X-ray generation by high intensity laser pulses

Inaugural Dissertation
zur
Erlangung des Doktorgrades der
Mathematisch-Naturwissenschaftlichen Fakultät
der Heinrich-Heine-Universität Düsseldorf

Dezember 2017

vorgelegt von
Stephanie Kathrin Brauckmann
aus Arnsberg

aus dem Institut für Laser- und Plasmaphysik
der Heinrich-Heine-Universität Düsseldorf

Gedruckt mit der Genehmigung der
Mathematisch-Naturwissenschaftlichen Fakultät
der Heinrich-Heine-Universität Düsseldorf

Referent: Prof. Dr. Oswald Willi
Koreferent: Prof. Dr. Alexander Pukhov

Tag der mündlichen Prüfung: 26.01.2018

Abstract

The interaction of ultra intense laser pulses with matter comprises the instant creation of hot dense plasma. Moreover it is accompanied by a large variety of mechanisms and processes leading to the emission of electromagnetic radiation in the XUV and X-ray regime, and the acceleration of particles. The work presented in this thesis aims to investigate different kinds of X-ray sources based on this interaction, applying two independent high intense laser pulses. One option for the production of X-rays is the usage of a secondary process, namely scattering of photons on fast moving electrons. The experimental investigations of Thomson scattering on laser accelerated electrons in two different setups was studied. In a first setup, a high energetic electron beam was accelerated from a gas jet. The remainder of the laser pulse was reflected back by a glass plate in order to be scattered on these electrons. The properties of the X-ray beam, generated during this process depend on the electron characteristics and the laser wavelength. A low divergent ($20-50\,\mathrm{mrad}$) X-ray beam with a number of photons in the range of $1.6\times10^4\,\mathrm{ph/keV}$ per 0.1% BW at $100\,\mathrm{keV}$ was detected along the electron beam axis. A counter-propagating beam geometry was implemented in order to investigate the frequency upshift of a laser pulse on electrons accelerated from thin solid foils. PIC simulations showed the generation of dense electron sheath using a target thickness in the range of tens of nm. Despite the challenge of spatial and temporal overlap, indication for a frequency upshift of the scattering 2ω laser pulse in the range of $500-1000\,\mathrm{eV}$ were found.

To investigate the X-ray emission coming from the hot dense plasma directly, spectroscopic measurements were carried out. Particularly, the radiation emitted during the transition of an excited state of an ion into its ground state was studied. The results showed, that the line emission intensity can be enhanced by a factor of 5, using a double beam geometry. Due to the controlled manipulation of the target condition with a heater beam, the radiation dynamics resulting from the interaction with the second beam were optimised. Hydrodynamic simulations and calculations with an atomic code for the expected line intensity supported this enhancement. Studying the line intensity ratio of two different thick targets, the plasma electron temperature was determined to be in the range of $1500-1900\,\mathrm{eV}$. Showing, that spectroscopic investigations can be a powerful tool for the diagnosis of hot dense plasmas.

Zusammenfassung

Die Interaktion von ultra-intensiven Laserpulsen mit Materie umfasst die Erzeugung heißer Plasmen. Darüber hinaus wird es von einer Vielzahl von Prozessen begleitet, die zur Emission von Strahlung im Röntgenbereich und zur Teilchenbeschleunigung führen. Das Ziel dieser Arbeit ist es, verschiedene Arten von Röntgenstrahlquellen zu untersuchen, die auf der Interaktion eines Targets mit zwei Laserpulsen basieren. Eine Option ist die Streuung von Photonen an sich schnell bewegenden Elektronen (Thomson Streuung), die in zwei verschiedenen Konfigurationen untersucht wurde. Im ersten Setup wurden Elektronen mit Energien im Bereich $50 - 100\,\mathrm{MeV}$ aus einem Gasjet beschleunigt. Der Rest des Laserpulses wurde zurückreflektiert, um an den beschleunigten Elektronen gestreut zu werden. Röntgenstrahlen mit einer geringen Divergenz ($20 - 50\,\mathrm{mrad}$) und einer Photonenanzahl von $1.6 \times 10^4\,\mathrm{ph/keV}$ pro 0.1% BW bei einer Energie von $100\,\mathrm{keV}$ wurden entlang der Elektronenstrahlachse detektiert.

Um die Frequenzverschiebung eines Laserpulses zu beobachten, der auf Elektronen trifft, die zuvor aus einer dünnen Folie beschleunigt wurden, wurde eine Aufbau mit zwei gegenläufigen Strahlen implementiert. Trotz der großen Herausforderung der räumlichen und zeitlichen Überlappung von Elektronen und Laserpuls, konnten Indizien für die Frequenzverschiebung des 2ω Laserpulses in einem Bereich von knapp $1\,\mathrm{keV}$ gefunden werden. Um die Röntgenstrahlung, die direkt aus heißen und dichten Plasmen emittiert wird zu untersuchen, wurden spektroskopische Messungen durchgeführt. Dabei wurde vor allem die Strahlung untersucht, die bei dem Übergang eines angeregten Ions in seinen Grundzustand freigesetzt wird. Die Ergebnisse zeigten, dass die Linienintensität um den Faktor fünf ansteigt, wenn eine Doppelstrahlgeometrie verwendet wird. Die Strahlungsdynamik während der Interaktion mit einem intensiven Laserpuls wurde optimiert, durch kontrollierte Manipulation der Folieneigenschaften mit einem Heiz-Laserpuls. Hydrodynamische Simulationen und Berechnungen mit einem atomaren Code für die erwartete Linienintensität unterstützen diese Ergebnisse. Durch Untersuchung des Verhältnissen der Linienintensität von zwei verschieden dicken Folien, wurde die Plasmaelektronentemperatur bestimmt, die im Bereich von $1500 - 1900\,\mathrm{eV}$ liegt. Es wurde gezeigt, dass spektroskopische Untersuchungen ein wichtiges Werkzeug für die Diagnose von heißem dichtem Plasma sein können.

Contents

Introduction

The development of few-cycles, ultrahigh intense laser pulses initiated investigations on new regimes of laser-matter interaction. An ultra-intense laser pulse, incident on matter, is an abundant source for many kinds of radiation and high energetic particles. Nowadays it is one of the most important research topics in modern physics, with applications in the field of particle acceleration [1] [2], inertial fusion [3] [4], nuclear physics [5] and laboratory astrophysics [6].
While most experiments in the field of laser-matter interaction are based on a single intense laser pulse, the Arcturus Laser facility in Düsseldorf has the great advantage of having two independent high intensity laser beams. This unique feature opens up the opportunity for new concepts and regimes in all topics of relativistic laser plasma physics. Applying both beams, either sychronised or with a certain delay onto a solid target will modify the whole interaction process and the accompanied X-ray radiation [7] and particle acceleration [8]. Another approach is the utilisation of one beam as the base for a laser generated particle source. A technique called proton probing, uses accelerated protons as a radiography diagnostic for a second laser plasma interaction [9]. The proton beam properties, particularly the divergence, can be modified by shooting a high intense laser pulse onto a metal cylinder or wire structure in order to create strong electric fields, which help to focus the particles [10] [11]. The injection and acceleration of electrons in plasma wakefields can be controlled and enhanced by the application of a second laser pulse [12]. Furthermore, a double beam configuration can be operated in order to generate ultrashort X-ray pulses via Thomson backscattering of photons on laser accelerated electrons [13].
The huge demand of high-quality X-ray beams in fundamental research and in even more practical applications, including cancer radiotherapy, radiography of dense objects or the analysis of large, fast moving biomolecules, leads to a great scientific inter-

est in this topic. Routinely implemented in medical treatments are Bremsstrahlung sources, which rely on linear accelerators. Conventional synchrotron sources are recently competing with free electron lasers, which are able to reach an extremely high brightness [14].
A promising approach to generate high brilliance X-ray radiation on a smaller and less cost intensive scale is the scattering of laser light on fast moving electrons. The scattered photons experience a frequency upshift, based on the relativistic Doppler effect. Freely tunable parameter, in order to manipulate the radiation properties, are the energy of the electron beam γ, the initial photon frequency ω_0 and the scattering pulse intensity a_0.
One main goal of this work is to investigate different setups for the implementation of an all laser generated X-ray source based on Thomson scattering. Both, the electron acceleration mechanism and the scattering beam properties are studied. The first concept uses laser wake field acceleration (LWFA) for the generation of a high energetic, low divergent electron beam from a helium gas jet. The remainder of the laser pulse is reflected back by a glass plate, in order to become the scattering pulse. The outcome is a likewise low divergent X-ray beam, which is characterised by a number of photons of 1.6×10^4 ph/keV per 0.1% BW at 100 keV.
Another scheme involves two high intense laser beams. During the interaction of the first laser pulse with a thin solid foil, dense electron sheath are created. The second laser pulse is used for the scattering process on those electron layers. The challenging part of this configuration is to guarantee a sufficient spatial and temporal overlap of the electrons with the scattering laser pulse. The result is a frequency upshifted signal, detected along the electron propagation axis.

As stated before, hot dense plasmas are a radiation source on its own. Beside self emission at the laser frequency ω_L or multiple of it, radiation in the X-ray and XUV range is emitted. When the energy of the laser pulse is absorbed by the target within a short amount of time, dense plasmas with typical temperatures of hundreds of eV are formed. A comparable condition for matter is found in the interior of stars. At such high temperatures, the electrons are usually completely stripped off the ions. Recombination processes and bound-bound transitions in ions of various charge states are two examples of radiation mechanisms contributing to the final emission spectrum. The type of radiation, broad continuum or narrow line emission,

and its strength depend on temporally evolving parameters, such as the temperature, density and ionisation degree of the plasma. Thus, plasma spectroscopy is a powerful tool for the diagnosis of different plasma conditions, which makes is suitable for experimental investigations in laboratory astrophysics. The experimental studies reported in the second part of this thesis are focused on investigating the physical properties and dynamics of hot dense plasmas by spectroscopic measurements and hydrodynamic simulations. Firstly, the line emission yield of various plasma conditions of low-Z target material is examined. In order to create those conditions, one laser pulse is used to pre-heat the target before the second main pulse arrives. The delay (ps time scale) between both beams is a measure for the target density and plasma scale length, which in return influences the radiation emitted from the plasma. In comparison to the ps to ns time scale of the plasma expansion and X-ray emission period, the ultrashort (fs) laser pulse deposits its energy within a negligible amount of time. Thus, the dynamics of the hot dense plasma can evolve without further influence by the strong electromagnetic fields of the laser pulse. The second spectroscopic measurement involves a scan of two different target thicknesses. Due to the complex interplay of the plasma density, ionisation degree and the plasma temperature, the emissivity and the opacity depends on the available target dimension. The line emission ratio for both target types is measured and compared to theoretical calculations in order to determine the plasma temperature.

The structure of this thesis is as follows:

- Chapter 2 gives an overview of the physical processes relevant to this thesis starting with the ionisation of a target by an electromagnetic wave. Furthermore the interaction of this wave with a single free electron and its energy coupling to the plasma are described. After the introduction of different electron acceleration schemes, atomic processes in hot plasma are discussed. Finally a secondary process, the scattering of electromagnetic radiation on accelerated electrons is depicted.

- In Chapter 3 the main methods and devices used to obtain the experimental results of this thesis are introduced. Initially, the functionality of the high power laser system ARCTURUS is presented followed by optical plasma diagnostics such as interferometry and shadowgraphy. A description of the electron

spectrometer and the x-ray detection, diagnostics which detect the radiation generated during the interaction conclude the chapter.

- Experimental results on the topic of Thomson scattering of a laser pulse on laser generated electrons in two different setups are presented in Chapter 4. 100 MeV electron bunches are created during the interaction of the laser pulse with a gas jet. The pulse is reflected back towards these electrons by a glass plate and during the following scattering process, an X-ray beam in the energy range of 150 keV is generated. In the second part of the chapter a setup, using two independent beams is introduced. The acceleration of dense electron sheaths from thin targets is investigated experimentally and with the help of PIC simulations. Finally, results on a frequency upshift of the second laser pulse on these electron slabs are presented.

- Chapter 5 summarises the study on line emission from hot plasma at various target conditions. Typical emission spectra are introduced and the visible lines are identified. The emission yield depends on the electron density, temperature and ionisation degree of the plasma. The results reveal that the line intensity can be enhanced by pre-expanding the target with a second laser pulse. Furthermore the plasma temperature, present during the interaction of a high intense laser pulse with a tens of nm thick low-Z material is determined by measuring the line intensity ratio of heliumlike carbon ions. The expected line intensity at different temperatures is simulated using a hydrodynamic code for the plasma expansion in combination with an atomic physic code for the calculation of the emission yield.

- The final chapter is a summary of the experimental and simulation results presented in this thesis. An outlook for future investigations and possible experimental campaigns is given.

Role of the author

As a main investigator the author was leading the experiments presented in this thesis and carried out at ARCTURUS laser facility in Düsseldorf under the supervision of Mirela Cerchez.
Parts of the theoretical background described in chapter 2 was complied by the author

in the framework of her master thesis [15].
For the analysis of interferometry images, in order to obtain the gas jet density in section 4.1.1, the author used a Matlab code developed by Ilhan Engin.
The theoretical calculations and simulations presented in section 4.1 originate from a Matlab code evolved by the author. Energy dependent transmission curves for various Cu filter are implemented in the code, which were produced by Maximilian Kosel during his Bachelor thesis [16], using GEANT4.
The experimental investigations on the plasma expansion of solid targets in section 4.2.2, was carried out by the author in collaboration with a Master student. In this context, the data presented in figure 4.14 were prepared by Esin Aktan in the framework of her Master thesis [17]. The author processed, analysed and interpreted the output of the 2D PIC simulations presented in section 4.2, based on the relativistic PIC code EPOCH. The simulation was run by Xiaoming Zhu on the cluster of the Centre for Information and Media Technology (ZIM) at the University of Düsseldorf.
The hydrodynamic code Multi-fs and the atomic code FLYCHK were employed by the author for the simulations in section 5.5. Additionally the author further processed and organised the results with Matlab. Helpful input regarding the simulations with FLYCHK were provided by Steve Rose and Dave Riley.

Physical processes in laser- plasma interactions

In this chapter an overview of the fundamentals of laser- plasma interactions is given. The basic processes in conjunction with high intensity laser light on matter are described with focus on electron acceleration and X-ray sources. At the beginning of the chapter a description of ionisation processes with different intensity conditions is introduced. The motion of the freed electrons is dominated by the applied laser field via the Ponderomotive force, which originates from the electric field's gradients. Fundamental plasma parameters, such as the Debye-length, plasma frequency, critical density and the refraction index, as well as the propagation of light in a plasma are presented. An overview regarding the main processes involved in the laser energy transfer to the plasma is given. Processes including collisional absorption (dominant in low intensity regime), as well as collisionless absorption (relevant in the relativistic regime) are discussed. A laser produced plasma can be the origin of a wide variety of radiation sources consisting of electrons, protons and characteristic X-rays. Different types of electron acceleration mechanisms and the atomic radiation effects are presented. Finally the scattering of laser light on the accelerated electrons and the associated frequency upshift of these photons is introduced.

2.1 Ionisation

To describe the plasma properties it is necessary to analyse the dynamics of its components, so the basic interaction processes between light and matter have to be

clarified and here the example of the hydrogen atom is used. The production of a plasma by the interaction of a laser with matter is caused by ionisation processes. Considering the Bohr model, the theoretical laser intensity threshold for ionisation can be derived. The Bohr radius is

$$a_B = \frac{4\pi\epsilon_0\hbar^2}{me^2} = 5.3 \times 10^{-9}\, cm \tag{2.1}$$

with the vacuum permittivity $\epsilon_0 \approx 8.854 \times 10^{-12}$ As/Vm, the reduced Planck constant $\hbar = \frac{h}{2\pi} \approx 1.055 * 10^{-34}$ Js, the electrons mass m and the elementary charge e [18]. To overcome the Coulomb force between the electron and the atomic nucleus of hydrogen, an electrical field stronger than

$$E_a = \frac{e}{4\pi\epsilon_0 a_B^2} \approx 5.1 \times 10^9\, V/cm \tag{2.2}$$

has to be applied. This field corresponds to a laser intensity $I_L > I_a = \frac{\epsilon_0 c E_a^2}{2} \approx 3.51 \times 10^{16}\,\mathrm{W/cm^2}$ in which c is the speed of light. However, ionisation processes can also be observed using intensities lower than this threshold. In the following section different processes, depending on the laser intensity used, are explained based on the work of Burnett [19] and Gibbon [18]. The dominant process depends not only on the laser intensity, but also on the temporal profile of the laser pulse. Saturation is possible before the laser pulse reaches its maximum intensity [20]. The most common ionisation process is **Photo ionisation**, which describes the absorption of a single photon with suitable frequency by an atomic bounded electron. In this process, the electron receives enough energy to overcome the Coulomb potential of the atom and leaves it. With visible and near infrared lasers this is not possible, because the photon energies (e.g. $\lambda = 800\,\mathrm{nm}$, $h\nu \approx 1.54\,\mathrm{eV}$) are much lower than typical first ionisation potentials of common targets.

Increasing the photon flux provides the opportunity of concurrent absorption of multiple (n) lower frequency photons (ω_L) by one electron, so that $\hbar n\omega_L = E_{ion}$. The quantum mechanical description of **Multi-photon ionisation (MPI)** exhibits consecutive energy input based on a certain durability of the electrons virtual states caused by single photons. The electron is excited by a single photon into a intermediate or virtual state and stays there for a certain amount of time before it relapse into its ground state by emitting a photon. However, if the photon flux is high

enough, the probability for absorption of another photon before relapsing into the ground state rises and the atom can be ionised. The ionisation rate for n photons can be described as

$$\Gamma_n = \sigma_n I^n, \tag{2.3}$$

where σ_n is the generalised cross section and I the laser intensity. The process dominates at low intensities below a certain saturation intensity. For higher intensities (in the order of $10^{13}\,\mathrm{W/cm^2}$) the electron absorbs more photons than required for ionisation, this leads to **Above-threshold ionisation (ATI)**. The kinetic energy of the photo-electron is given by an extension of the photoeffect formula derived by Einstein:

$$E_f = (n+s)\hbar\omega_L - W_f, \tag{2.4}$$

where n describes the number of photons necessary for MPI, s the number of additional photons and W_f the ionisation potential.
With increasing the laser intensity, the laser driven field is sufficiently strong to distort and reduce the Coulomb potential, and with it the potential barrier for ionisation. Taking the laser electric field E into account the effective potential experienced by the bound electron in a distance x from the nucleus is then given by

$$V(x) = -\frac{Ze^2}{x} - eEx. \tag{2.5}$$

For positive x the potential is reduced and outer shell electrons may escape via **Tunneling ionisation** (TI) or **Over-the-barrier ionisation** (OTBI), which appears when the Coulomb potential is completely suppressed ($\mathrm{I}>10^{15}\,\mathrm{W/cm^2}$). The transition between MPI and TI is characterised by the *KELDISH-Parameter*

$$\gamma_K = \omega_L \sqrt{\frac{2W_f}{I_L}} \tag{2.6}$$

for the laser frequency ω_L, intensity I_L and ionisation potential W_f. MPI and ATI are expected for $\gamma_K > 1$, whereas the TI and OTBI become dominant with increasing field strength and laser wavelength ($\gamma_K < 1$).

2.2 Single electron motion in the laser field

After considering ionisation of the material by exposure to a laser field, the dynamics of the free electrons can be described [21]. Their behaviour under the influence of an electromagnetic field is an important factor for most of the physical processes in laser plasma interactions. The fast reaction of the electrons plays a role in the laser propagation through the plasma and in the energy absorption and transfer mechanisms. However, before going into detail about these topics in section 2.3 and 2.5 the single electron motion in the laser field is summarised.

In conformity with the Lorentz-equation

$$\frac{d\vec{p_e}}{dt} = m_e \frac{d\vec{v_e}}{dt} = -e\left(\vec{E} + \vec{v_e} \times \vec{B}\right), \tag{2.7}$$

particles with a charge e and velocity $\vec{v_e}$ in the time depending electromagnetic field, with the speed of light c and the momentum p_e, perceive a certain force. The electric and magnetic field components for a linear polarised, monochromatic laser field, which affects the electrons are

$$\begin{aligned} E(\vec{r},t) &= \vec{E_0} cos(\omega t - \vec{k}\vec{z}) \\ B(\vec{r},t) &= \vec{B_0} sin(\omega t - \vec{k}\vec{z}), \end{aligned} \tag{2.8}$$

with ω the laser frequency in the plasma and light propagation in the $\vec{k}$ vector direction. Assuming a non relativistic velocity of the electron ($v_e \ll c$) corresponding to laser intensities $I < 10^{18}\,\mathrm{W/cm^2}$ at $\lambda = 1\,\mu\mathrm{m}$, the effect of the magnetic field is not strong enough and the second part of equation 2.7 can be neglected. The result of the first part of equation 2.7, assuming a laser wave propagation in z direction and linear polarisation, for an electron with the charge e, starting from $x_{(t=0)} = 0$ at rest, is a transverse harmonic oscillation in the electric field E with the amplitude $x_0 = \frac{eE_0}{m_e\omega^2}$ and with a maximum velocity $v_0 = \frac{eE_0}{m_e\omega}$.
For the high intensity regime, in which the motion of the electron can become relativistic, it is convenient to establish the dimensionless light amplitude

$$a_0 = \frac{|v_0|}{c} = \frac{eE_0}{m_e \omega c} = \left(\frac{1}{2\pi^2 \epsilon_0} \frac{e^2}{m_e^2 c^5} \lambda_L^2 I \right)^{\frac{1}{2}} = 0.85 \cdot \lambda_L[\mu\text{m}] \sqrt{I[10^{18}\,\text{W/cm}^2]}. \quad (2.9)$$

By inserting the value for the laser wavelength in μm and laser intensity in $10^{18}\,\text{W/cm}^2$, the transition of non-relativistic ($a_0 \ll 1$) to relativistic ($a_0 \geq 1$) particle motion can be easily evaluated. The relativistic factor $\gamma = \frac{1}{\sqrt{1-v^2/c^2}}$ becomes crucial and the momentum of the electron changes to $p = \gamma m_e c\beta$. It also affects a relativistic increase of the electron's mass and the motion becomes anharmonic. Using equation 2.9, it can be calculated that the relativistic effects become relevant for a laser intensity $I \geq 2.1 \times 10^{18}\,\text{W/cm}^2$ at $\lambda = 0.8\,\mu$m wavelength (equation 2.9). The magnetic field now exerts sufficient magnetic force to the electron, which causes a nonlinear dynamic and an average forward drift velocity

$$v_D = \frac{a_0^2}{4 + a_0^2} c e_z \quad (2.10)$$

in the direction of propagation, resulting from the cross product of oscillation velocity and magnetic field.

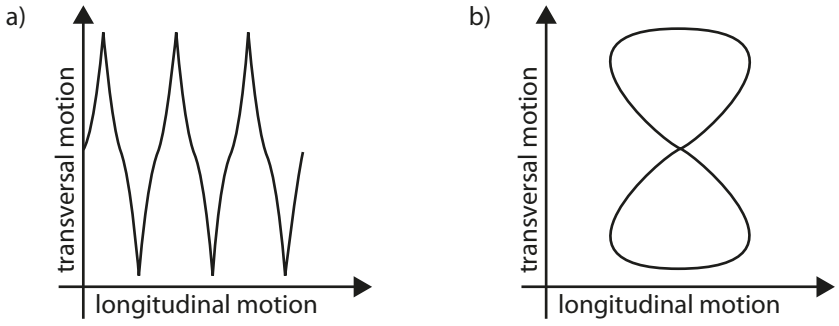

Figure 2.1: Electron motion in a linear polarised electromagnetic wave a) in the laboratory reference and b) in the reference frame moving with the average drift velocity.

Figure 2.1 a) shows the motion of an electron in a linear polarised electromagnetic wave in the laboratory reference frame. Beside the oscillation in the polarisation direction of the electric field, there is a drift in the propagation direction. Changing the reference frame to one which is moving with the average drift velocity, the shape

of motion becomes a figure of eight (figure 2.1 b)). Starting from rest, the free electron drifts in the propagation direction during the laser pulse and rests again afterwards, so that the electrons' net-energy does not increase.

2.2.1 Ponderomotive potential

The **Ponderomotive force** is exerted on the plasma electrons by the electromagnetic wave due to spatial variation of the wave intensity. In the non relativistic regime the energy gain of an electron is expressed by the average kinetic energy over one oscillation using $U_p = \left\langle \frac{1}{2} m_e v_e^2 \right\rangle$. This potential

$$U_p = \frac{e^2 E_0^2}{4 m_e \omega^2} \tag{2.11}$$

is the so called **Ponderomotive potential**. However, to reach high intensities, which are desired e.g. for ion acceleration via laser-plasma interaction, the laser pulse is focused on an appropriate target and the intensity is no longer homogeneous. In the case of a Gaussian transverse intensity profile, the electron is affected by an additional acceleration, which is related to the transverse laser field gradient. The electron moves away from the beam axis during the first half of the laser cycle. The reverse driving force in the second half is weaker, as the field strength decreases with the distance from the laser axis. The electron is not able to reach the starting point again. The ponderomotive force can be described quantitatively by averaging the dynamics over one laser cycle. Following the derivation in [18], where the laser pulse propagates in z-direction and the E-field varies with y perpendicular to the propagation, the force can be identified as

$$f_p = -\frac{e^2}{4 m_e \omega^2} \frac{\partial E_0^2}{\partial y} = -\nabla U_p, \tag{2.12}$$

which is the negative gradient of the ponderomotive potential. In the non- relativistic case the force acts in the y-direction only and is perpendicular to the $\vec{k}$-vector of the wave.

In the relativistic regime, where the laser intensity is in the order of $10^{18}\,\mathrm{W/cm^2}$ or higher the magnetic field component is no longer negligible and the electron dynamics become nonlinear. The ponderomotive force leads (similar to the non-relativistic regime) to a displacement of electrons towards lower intensity regions. However,

the electron now experiences additionally a relativistic mass increase during the first half of the laser cycle and a forward drift due to the magnetic field component. In the second half of the laser cycle the exerted force is weaker, due to the decreasing intensity with increasing radial distance. The net effect is that the electron is pushed both sidewise and forward. Gibbon [18] derives the relativistic ponderomotive force by separating the electron motion into slow and fast components. The relativistic ponderomotice force is finally expressed as

$$\mathbf{f}_p = \frac{dp^s}{dt} = -mc^2 \nabla \overline{\gamma}, \tag{2.13}$$

where $\gamma = (1 + p_s^2/m^2c^2 + a_0^2/2)^{1/2}$ is the relativistic factor of the oscillation and p_s is the impulse which describes the slow component of the electron motion.

2.3 Plasma parameters and light propagation

The previous sections shows how high intensity lasers can both, ionise matter and also influence the dynamics of the resultant free electrons. This description of laser-electron interaction is not sufficient to understand all effects of laser- plasma interactions. The plasma is a multi- particle ensemble, in which collective effects play a major role caused by self generated coupling of all particles [21]. An important parameter to describe the kinetic energy of plasma particles, which usually occurs in form of a disordered motion, is their temperature. The electron temperature T_e is typically much higher than the ion temperature T_I because of their considerably lower mass. In addition, the positive and negative charge of the ions and electrons compensate each other to fulfill the demand of quasi-neutrality. However, local charge separation does exist over a scale length known as the Debye length

$$\lambda_D = \sqrt{\frac{\epsilon_0 k_B T_e}{n_e e^2}} = 2.21\,\mu\text{m} \times T_e^{1/2}[\text{MeV}] \times n_e^{-1/2}[10^{19}\,\text{cm}^{-3}], \tag{2.14}$$

where $k_B \approx 1.38 \times 10^{-23}$ J/K is the Boltzmann constant and T_e the electron temperature. From the macroscopic point of view ($\gg \lambda_D$, a plasma behaves neutrally. The Debye length is also a scale length for the oscillation of electrons around the much heavier and consequently more inert ions, which are assumed to be quasi-static. The frequency of this oscillation can be derived from the equation of motion and the

Gauss theorem and results in

$$\omega_p = \left(\frac{e^2 n_e}{\epsilon_0 m_e}\right)^{1/2} \cong 5.6 \times 10^4 n_e^{1/2} [\mathrm{cm}^{-3}][\mathrm{s}^{-1}]. \tag{2.15}$$

The resonance frequency of the electrons depends on their basic properties like the density n_e, the elementary charge and their mass m_e.
In contrast to a neutral gas, the accumulation of the positively-charged ions and negatively-charged electrons generates a plasma. This leads, in the local scale, to the formation of an electric field E, current flow and consequently the development of a magnetic field B; so that a modification of light propagation through plasma occurs. For an electromagnetic wave $E = E_0 exp(kx - \omega t)$ with the frequency ω and the wave vector $|\vec{k}| = k = 2\pi/\lambda$ the dispersion relation in a plasma is given by

$$\omega^2 = \omega_p^2 + c^2 k^2. \tag{2.16}$$

When a laser beam hits a plasma, the propagation through the plasma is just possible for frequencies $\omega_L > \omega_p$. For $\omega_L < \omega_p$ the $\vec{k}-$vector becomes imaginary, which means the laser is not able to propagate in the plasma. Inserting eq. 2.15 into the limiting case $\omega_L^2 - \omega_P^2 = c^2 k^2 = 0$ the critical density is found to be

$$n_c = \frac{\epsilon_0 m_e}{e^2} \omega_L^2 \cong \frac{1.1 \times 10^{21}}{(\lambda[\mu\mathrm{m}])^2} [\mathrm{cm}^{-3}], \tag{2.17}$$

which divides the plasma into two distinctly different regions: the underdense ($n_e < n_c$) and the overdense plasma ($n_e > n_c$).

Figure 2.2 depicts a schematic of a non-uniform plasma, where the plasma density n_e is a function of x. Electromagnetic waves can penetrate into the underdense area, but are reflected at a point where the plasma density reaches the critical density n_c, above which the plasma becomes overdense.
In laser-solid target interaction the density profile strongly depends on the temporal profile of the laser pulse, which usually contains pre- and postpulses. The prepulse preheats the target and a significant plasma expansion can appear. The main pulse deposits its energy in the created low density matter instead of interacting directly with the dense target.

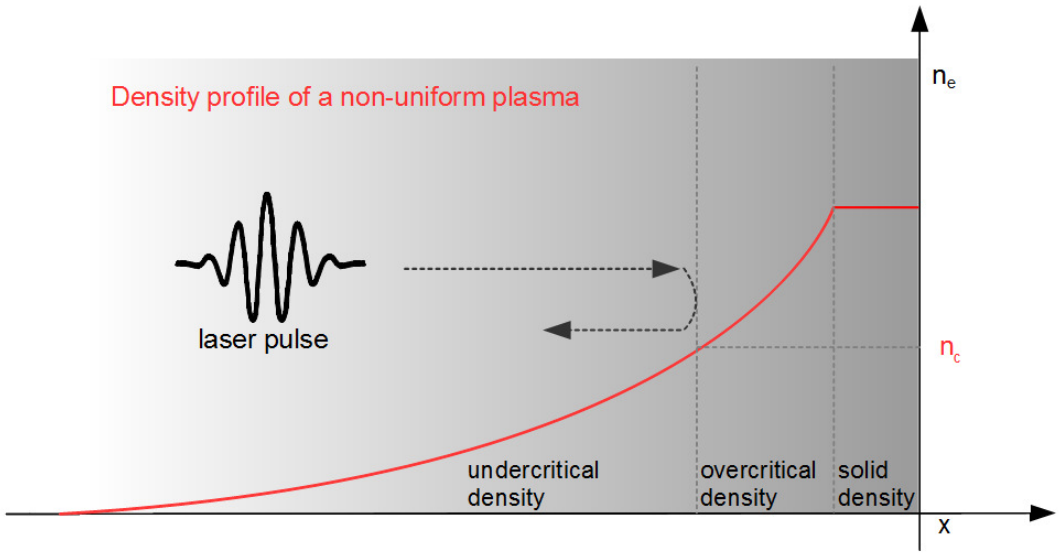

Figure 2.2: Light propagation in a non-uniform plasma. A laser pulse can propagate into the underdense part of the plasma and is reflected as the electron density exceeds a certain threshold, the critical density n_c.

The propagation in a underdense plasma leads to significant interactions between the electromagnetic field and the plasma, resulting in deviations of the electron density and a relativistic mass increase of the electrons. This affects the refractive index η of the underdense target, which can vary in time and space. The refractive index can be written as

$$\eta_p = \frac{ck}{\omega} = \sqrt{1 - \frac{\omega_p^2}{\omega^2}} = \sqrt{1 - \frac{n_e}{n_c}} \tag{2.18}$$

and depends on the plasma frequency ω_p and consequently on the electron density n_e and the critical density n_c.

When the laser-matter interaction becomes relativistic, the propagation of light in classically overdense plasma ($n > n_c$) is possible. The phenomenon, known as self−induced transparency, describes the modification of the plasma frequency and therefore the critical density in the relativistic regime. The critical density is corrected due to the relativistic mass increase of the electrons to

$$n_{c,rel} = n_c \sqrt{1 + \frac{a_0}{2}}, \tag{2.19}$$

where a_0 is the dimensionless light amplitude (eq. 2.9).

2.3.1 Self-focusing

An important effect at relativistic laser intensities in underdense targets is self-focusing of the laser pulse in the plasma beyond the geometrical limits [18]. As discussed before, the propagation of laser light in plasma strongly depends on its refractive index. A transverse gradient in the refractive index of the plasma, peaking on the laser axis, reduces the phase velocity of the central part of the pulse. Consequently the phase front of the whole beam profile bends and self-focusing occurs. Two mechanisms contribute to this effect: Firstly, the ponderomotive force pushes electrons out of the region with higher laser intensity. As the refractive index increases when the electron density decreases, a transverse gradient develops. The second mechanism is related to the dependency of the refractive index to the γ-factor of the oscillating electrons. At relativistic intensities the γ-factor is at its maximum near the propagation axis, thus the refractive index rises and the laser pulse becomes self-focused. The power threshold at which these phenomena occur is

$$P_{cr} \approx 17(\frac{\omega}{\omega_P})^2 \,\mathrm{GW} \tag{2.20}$$

where plasma frequency ω_p directly depends on the electron density (eq.2.15).

2.4 Excitation of plasma waves in underdense plasma: Variants of Laser wakefield acceleration

The acceleration of electrons by waves in an underdense plasma which are triggered by intense laser pulses was first suggested by Tajima and Dawson [22]. The concept of **laser wake field acceleration (LWFA)** comprises the excitation of a plasma wave in the wake of a laser pulse comparable to the waves created in the wake of a ship. The following description is based on [23]. The intense laser pulse triggers plasma oscillations due to its nonlinear ponderomotive force (eq. 2.13), which pushes electrons away from regions of high laser intensity gradient. Thus, a positive charged cavity is generated behind the laser pulse surrounded by the expelled electrons. On the other hand, the plasma applies a contrary potential pushing the electrons back onto the laser axis (or further). Electrons, which are trapped in the wake, experience a strong energy gain. The amplitude of this oscillation and the properties of the cav-

ity depend strongly on the strength of the driving pulse, quantified by its relativistic amplitude a_0. The phase velocity of the plasma wake equals the group velocity of the laser pulse $v_p = \omega_p/k_p = v_{L,g} = \eta c$, where η is the refractive index of the plasma. A huge advantage of plasma as a medium for the acceleration of particles is the accessibility of high electric fields, orders of magnitude above the limit for conventional accelerators [23]. In a cold plasma, the limit of the electric field in the linear regime is given by

$$E_{wb} = \frac{cm_e\omega_p}{e} = 96\,\mathrm{V/m} * \sqrt{n_e[\mathrm{cm}^{-3}]}, \tag{2.21}$$

where ω_p is the electron plasma frequency (eq. 2.15) and n_e is the electron density. Typical values for electron densities in gas targets are in the range of $10^{19}\,\mathrm{cm}^{-3}$, leading to an electric field of up to 300 GV/m. If this limit is exceeded, neighbouring electron sheets in the longitudinal plasma oscillation may cross each other, associated with a singularity in density [18]. The result is a loss of coherence, the wave breaks. In the relativistic case ($a_0 > 1$), the electric field can reach even higher values before the wave-breaking limit is exceeded. In order to use those fields, there are several approaches how to excite and preserve plasma waves with the final goal of a stable and reproducible electron acceleration.

In the linear case ($a_0 < 1$), the response of the plasma on the perturbation by the laser pulse can be derived by the Poisson equation, the equation of continuity and the fluid momentum equation. The linear wave is excited inside the uniform plasma, which can be described by

$$\begin{aligned}(\partial^2/\partial t^2 + \omega_p^2)\delta n/n_0 &= c^2\nabla^2 a_0^2/2\\ (\partial^2/\partial t^2 + \omega_p^2)\Phi &= \omega_p^2 a_0^2/2,\end{aligned} \tag{2.22}$$

where Φ is the electrostatic potential, n_0 the plasma density and accordingly $\delta n/n_0 = (n - n_0/n_0)$ is the normalised density perturbation. For small perturbations, $\delta n/n_0 \ll 1$ and electric fields far underneath the limit for wave breaking ($E \ll E_{wb}$) (eq. 2.21), the solutions

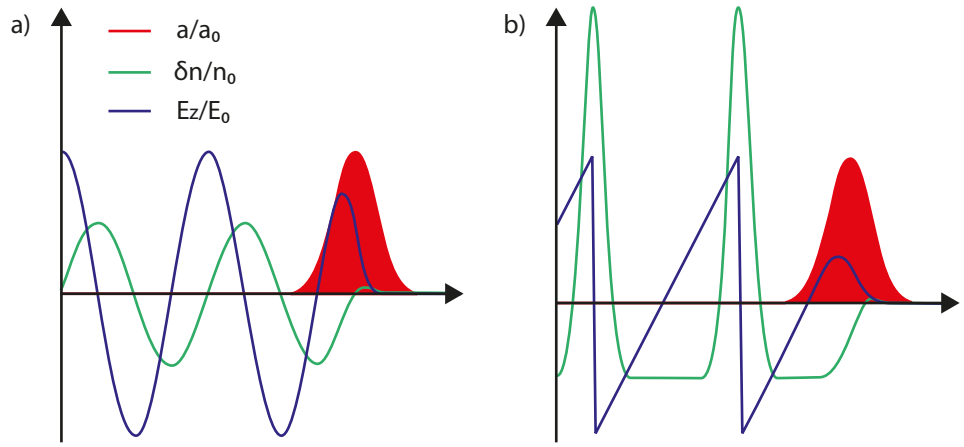

Figure 2.3: Density variation $\delta n/n_0$ and axial electric field E_z/E_0 in LWFA driven by an intense laser pulse based on [23]. In the linear case a) $a_0 < 1$ the fields follow a sinusodial function and the nonlinear regime b) $a_0 > 1$ the electric field forms a sawtooth profile, while the density develops strong peaks.

$$\begin{aligned} \delta n/n_0 &= (c^2/\omega_p) \int_0^t dt' sin[\omega_p(t-t')]\nabla^2 a_0^2(\mathbf{r},t')/2 \\ \mathbf{E}/E_{wb} &= -c \int_0^t dt' sin[\omega_p(t-t')]\nabla a_0^2(\mathbf{r},t')/2 \end{aligned} \tag{2.23}$$

describe plasma waves with a frequency ω_p. The solutions of equation 2.23 are convolutions of the gradient of the squared laser amplitude a_0 and a simple sinus function with the periodicity of $2\pi/\omega_p$. A schematic of the density and electric field oscillation in a plasma wave triggered by a weak laser pulse is shown in figure 2.3 a). In the linear regime the plasma wave follows a sinusodial oscillation with the plasma wavelength $\lambda_p = 2\pi c/\omega_p$.

At high power laser facilities, pulses with an amplitude $a_0 > 1$ are provided. The electrons, expelled by the ponderomotive force, become relativistic and trigger the generation of a nonlinear wave. Details about the derivations in the nonlinear regime can be found in [23], here the modification of the relevant parameters is given qualitatively.

In case the maximum amplitude of the electric field E_{max} exceeds E_0, its oscillation deviates from the linear case and develops into a sawtooth profile, while the den-

sity variation $\delta n/n_0$ changed into strong peaks, as illustrated in figure 2.3 b). The modification of the plasma wavelength is given by

$$\lambda_{Np} = \lambda_p \begin{cases} 1 + 3(E_{max}/E_0)^2/16, & E_{max}/E_0 \ll 1 \\ (2/\pi)(E_{max}/E_0 + E_0/E_{max}), & E_{max}/E_0 \gg 1, \end{cases} \tag{2.24}$$

which shows a lengthening of the plasma period as the laser amplitude enters the nonlinear regime.

A major development in the context of LWFA is theoretical work based on $3D$ PIC simulations by Pukhov and Meyer-ter-Vehn [24], which predict a non-linear broken-wave regime and is also called **bubble regime**. For relativistic few-cycle laser pulses, which are shorter than the plasma wavelength ($L \ll \lambda_P$), and with intensities high enough to overcome the threshold of wave breaking, the excitation of the plasma wave stops after the first oscillation. The wake field takes the shape of a single cavity or bubble in which electrons can be trapped and accelerated. A great advantage compared to classical LWFA is the generation of quasi-monoenergetic electrons.

In many experimental setups the laser pulse length is longer than the plasma wavelength ($L > \lambda_P$). However, it is possible that the laser pulse breaks up into a train of pulses if the laser power exceeds the critical power for self-guiding. Each pulse of this train is shorter than the plasma wavelength and therefore fulfilling the condition for LWFA. This regime is called **self-modulated LWFA** and has the advantage, that the parameter conditions to initiate the process are more flexible.

Figure 2.4 shows a typical energy distribution recorded during the experiment discussed in chapter 4.1. A 30 fs high intensity laser pulse ($a_0 = 2$) is focused into a $n_e = 5 \cdot 10^{19}\,\mathrm{m}^{-3}$ helium gas, implying $L \approx 1.5\lambda_P$ and $P \approx 10P_{cr}$. Here, the self-modulated LWFA regime is triggered leading to a 20 MeV broad energy peak at 100 MeV.

The electron energy gain is limited by the depletion of the laser pulse. An additional limit is, that the electrons and the plasma wave can dephase, which results in a electron deceleration. The depletion length is given by [23]

$$L_{depl} \approx \frac{\lambda_p^3}{\lambda^2} \begin{cases} 2/a_0^2, & a_0^2 \ll 1 \\ (\sqrt{2}/\pi)a_0, & a_0^2 \gg 1, \end{cases} \tag{2.25}$$

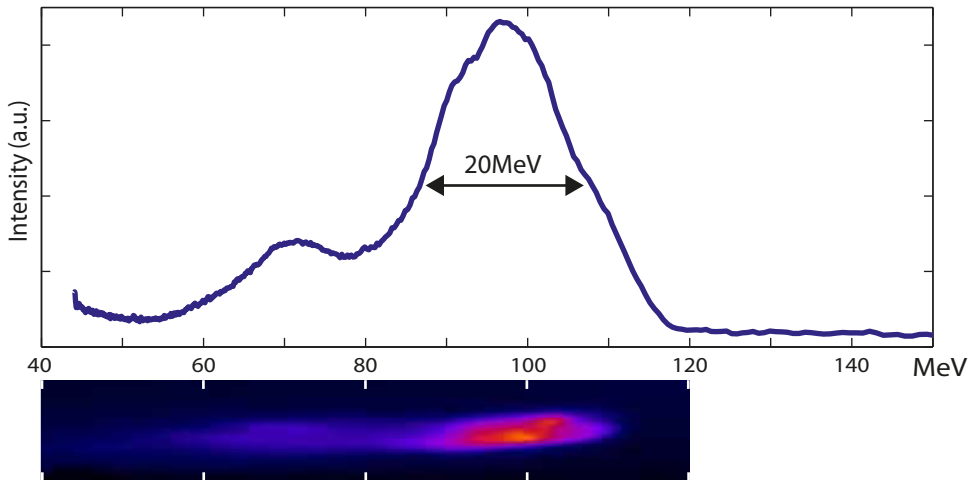

Figure 2.4: Electron spectrum from electron acceleration in the self-modulated LWFA regime. A high intensity laser ($a_0 = 2$) is focused onto a helium gas jet ($n = 0.03 n_c$). The electrons are accelerated and detected on the lanex screen of an electron spectrometer.

while the dephasing length for the two cases of low and high intensity is

$$L_{deph} \approx \frac{\lambda_p^3}{2\lambda^2} \begin{cases} 1, & a_0^2 \ll 1 \\ (\sqrt{2}/\pi) a_0 / N_P, & a_0^2 \gg 1, \end{cases} \tag{2.26}$$

where N_P is the number of plasma periods behind the laser pulse.

2.5 Coupling of laser energy into overdense plasma: Absorption and Acceleration schemes

One of the most important and discussed processes in the field of laser plasma interactions is the coupling of laser energy via electrons into the plasma. The energy absorption efficiency is a major factor in a variety of applications and effects. The absorption of laser energy by a plasma strongly depends on every type of laser and target parameters and is thus a non-trivial topic. Over the last few decades, many descriptions of absorption mechanisms were developed [18], [25]. For a quite moderate intensity regime collisional absorption (e.g. inverse Bremsstrahlung) and collisionless classical resonance absorption occur. In the ultrashort, high intensity laser pulse

regime collisionless processes are identified to be responsible for the energy transfer to the target. These mechanisms are the Brunel effect or vacuum heating, $\mathbf{j}\times\mathbf{B}$ heating and the anomalous skin effect. They are described in the following section. A short qualitative overview of some mechanisms out of the large zoo of descriptions for laser energy absorption in plasmas is presented. In addition, a combination of several energy transfer mechanisms is usually required to describe the behaviour of contemporary laser experiments.

2.5.1 Collisionless absorption

For high laser intensities, approaching or reaching the relativistic regime, the collision probability decreases rapidly, and collisionless absorption mechanisms dominate. For laser intensities less than $10^{24}\,\mathrm{W/cm^2}$, the interaction between the laser light and the electrons is relevant and the direct interaction of the ions can be neglected [25]. One of the main issues of developing theoretical models to fit experimental results is the complex behaviour and mutually interaction of the laser light with the plasma. The electron density for example, an important parameter for most of the absorption processes, is strongly influenced and modified by the laser, which results in a density variation in space and time. The following explanations are simplified models of different mechanisms which contribute to the total absorption.

When a p-polarised electromagnetic wave penetrates a plasma at a specific incident angle θ, the electric field has a component parallel to the plasma density gradient. This part of the electric field initiates a spatial oscillation of the electrons at the point of the critical density, which results in the development of a plasma wave. Here we choose the coordinates so that the electromagnetic wave propagates in the y-z-plane and the plasma density varies along the z-axes. The dispersion relation in this case is $\omega^2 = \omega_P^2 + (k_y^2 + k_z^2)c^2$; only k_z is a function of z but $k_y = \frac{\omega}{c}\sin\theta$ is constant. Using this relation to find the point where θ becomes 90°, the reflection point moves to a density $n_e = n_c \cos^2\theta$. Although the incident laser wave is reflected at this density, its field can tunnel into the region of the critical density and the condition for **resonance absorption** is satisfied. The electrons oscillate resonantly with the laser field and a plasma wave develops. This wave runs into the plasma longitudinally and transmits the laser energy by collision (Landau damping).

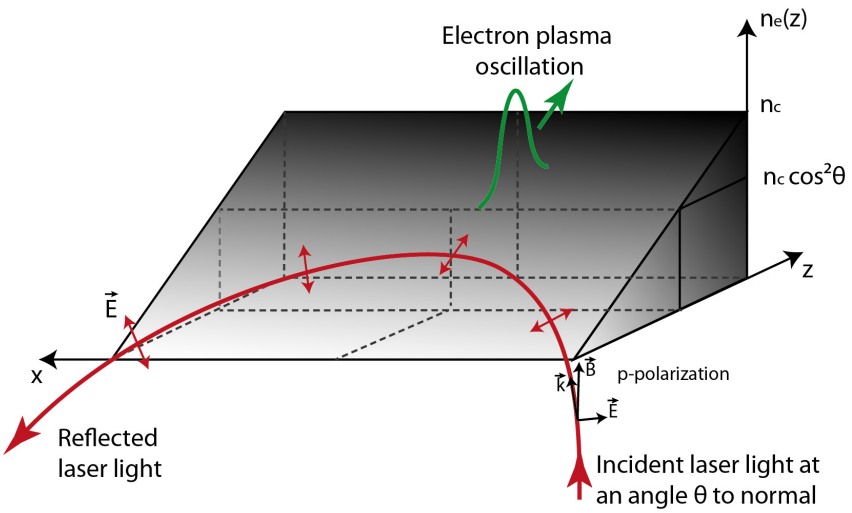

Figure 2.5: Light propagation in a plasma with increasing density gradient. Under certain conditions resonance absorption takes place.

The **Brunel effect** or **vacuum heating** describes the interaction of a steep plasma with a laser pulse of intensities ($I > 10^{19}\,\mathrm{W/cm^2}$) higher than necessary for collisional absorption. Because of the high laser intensity, the electrons are accelerated extremely abruptly into the vacuum at the steep plasma-vacuum boundary. The electric field direction changes after a half cycle, and the electrons are forced back towards the overdense region of the plasma. Due to the decreasing collision rate with increasing intensity, the free path λ becomes longer than the skin depth l_s (which is also the lasers maximal penetration length). The electrons become irreversibly independent of the laser field and thus deliver their energy to other particles. The plasma heats up quite efficiently in this case without the development of a plasma wave. Vacuum heating depends, analog to resonance absorption, for p-polarised waves on the incident angle, because the driving force is the electric field normal to the target surface.

Besides vacuum heating, the laser energy can be transmitted to electrons via another heating process. The driving force of $\mathbf{j} \times \mathbf{B}$ **heating** is the $\vec{v} \times \vec{B}$ component of the Lorentz force, which cannot be neglected in case of high laser intensities. It is relevant

for p- and s- polarisation and plays a significant role in short-pulse, high-intensity laser solid interaction, because it is most efficient when the incident pulse is normal to the target surface. At relativistic intensities, the $\vec{v} \times \vec{B}$ term induces a gyratory movement of the electrons with a final velocity component along the $\vec{k}$-vector of the radiation (as discussed in section 2.2). The ponderomotive force

$$f_x = -\frac{m}{4}\frac{\partial v^2(x)}{\partial x}(1 - \cos 2\omega t) \tag{2.27}$$

created by the laser field with frequency ω, includes the usual non-relativistic part and an oscillating component caused by the interaction between the transverse movement of electrons in the laser field and the magnetic field. The damping of this longitudinal oscillation provides the plasma heating.

The Normal skin effect comprises an oscillation of electrons within the skin depth and subsequent energy transfer due to collisions. With increasing electron velocity, the free path gets longer and the oscillation amplitude rises above the laser penetration length. This so called **anomalous skin effect** describes another laser energy absorption mechanism.

In the previous section, a qualitative description of the absorption mechanisms is given. Quantitative calculations or scaling laws require numerical modeling, which is beyond the scope of this thesis. However, Davies [25] gives a detailed comparison of different experimental measurements with numerical modeling of laser absorption in overdense plasmas in the relativistic regime and reveals the complexity and difficulties which accompany this topic.
Figure 2.6 shows several published values of absorption and numerical modeling as a function of $I\lambda^2$. To determine the general trends and the main conclusions, it is sufficient to compare the experimental and numerical results of Ping et al. [26] (black solid dots, squares and line). The other results belong to experiments and theoretical investigations dealing with fast electron absorption; further interpretation can be found in [25]. Ping et al. examined the relativistic regime and measured the total absorption by detecting the reflected and scattered radiation. Using a $\lambda = 0.8\,\mu$m p-polarised laser pulse focused on different plain target foils at an incident angle of 6° (solid black dots) and 45° (solid black squares), they investigated the absorption

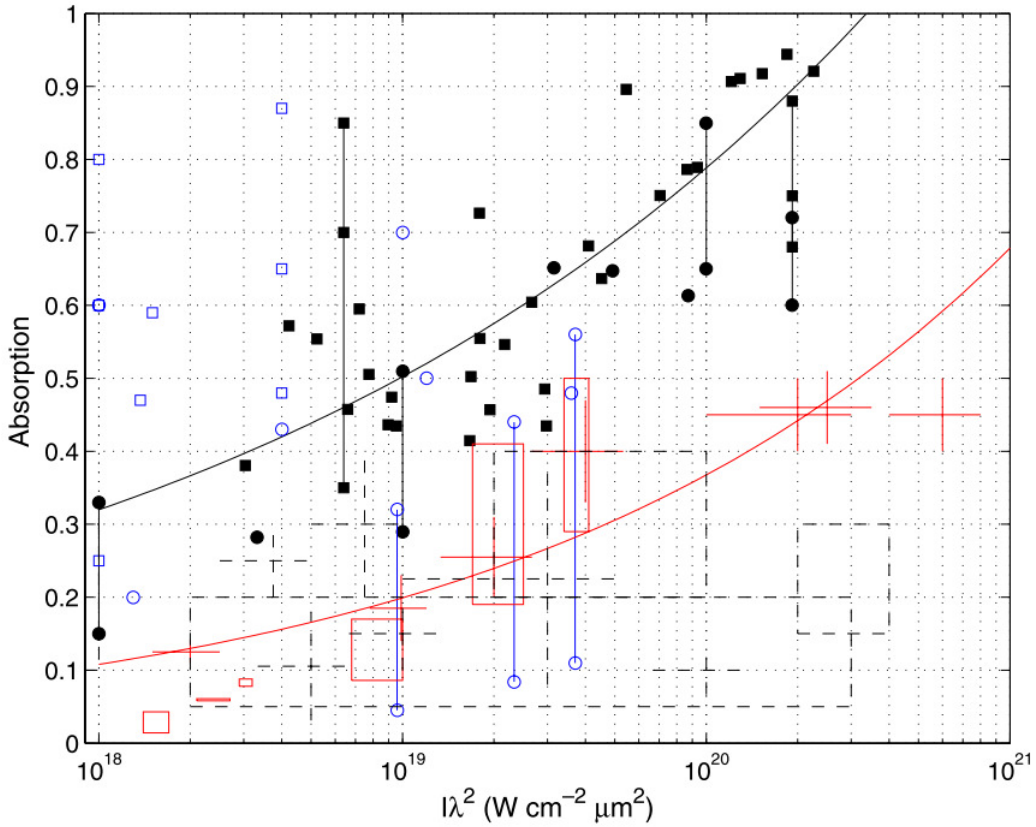

Figure 2.6: Absorption values as a function of $I\lambda^2$, published by Davies et al. [25]. The solid black symbols are results from [26], representing experimental data (dots 6° incident angle and squares 45° incident angle) and numerical (vertical lines) data from total absorption. The solid red and dashed black crosses and boxes are results from fast electron absorption from other experiments.

energy fraction in a intensity range $I\lambda^2$ from 1.64×10^{17} to $2.30 \times 10^{20}\,\mathrm{W/cm^2}$. The black solid line is a simple fit to the specific data and shows the increase in absorption with $I\lambda^2$.

The dependency of absorption on the incident angle and the plasma density cannot be specified due to the few data points and insufficiently determined parameters. Nevertheless, in the numerical results (vertical black lines) the preplasma conditions are varied to simulate different plasma densities. A long preplasma length leads to lower densities (the upper dot of the vertical line) and the density increases with shorter preplasma length (the lower dot of the vertical line). The results indicate an increase of absorption with lower density, with a maximum near the critical plasma density.

Although general trends can be clearly identified in these published results, further work is required to complete the current data sets. The consistently lower values of fast electron absorption (red data), compared to the total absorption, provide a motivation for furthers studies. As the absorption depends not only on the laser intensity, but also on many other parameters (e.g. the incident angle, plasma density, pulse duration etc.) there are many opportunities for future investigations.

2.5.2 Hot electrons and bunch formation from thin foils

When considering absorption mechanisms for high intensity, short pulse laser foil interactions, the generation of hot electrons with energies much higher than the bulk plasma temperature has to be mentioned. In the high intensity regime, this fraction of electrons absorbs most of the laser energy by collisionless mechanisms as those described earlier in this chapter. For most applications, the conversion efficiency of laser energy into hot electrons is designed to be as high as possible. As the hot electron temperature T_h depends strongly on absorption mechanisms, these models can be used to construct scaling laws for T_h. This also means, that several competing processes contribute to the resultant energy scaling. Different absorption mechanisms become dominant depending on the pulse intensity, duration, contrast or angle of incidence.
In figure 2.7 a comparison of experimental measurements of hot electron temperatures for short pulse solid target interactions with several scaling laws, which follow different absorption models in different intensity regimes, is presented [18]. The general trend shows a dependence of T_h on the product $I\lambda^2$, which is predicted in all theories. In the relativistic regime I$> 10^{18}\,\mathrm{W/cm^2}$, for a laser pulse normally incident onto a target, the absorption is dominated by $\mathbf{j}\times\mathbf{B}$ and the hot electron temperature is estimated by

$$\begin{aligned} T_h^W &\cong mc^2(\gamma-1) \\ &= mc^2\left[\left(1+\frac{p_{os}^2}{m^2c^2}\right)^{1/2}-1\right] \\ &\cong 511\left[\left(1+(0.73\times I[10^{18}\,\mathrm{W/cm^2}]\times\lambda^2[\mu\mathrm{m}])\right)^{1/2}-1\right]\ \mathrm{keV}, \end{aligned} \tag{2.28}$$

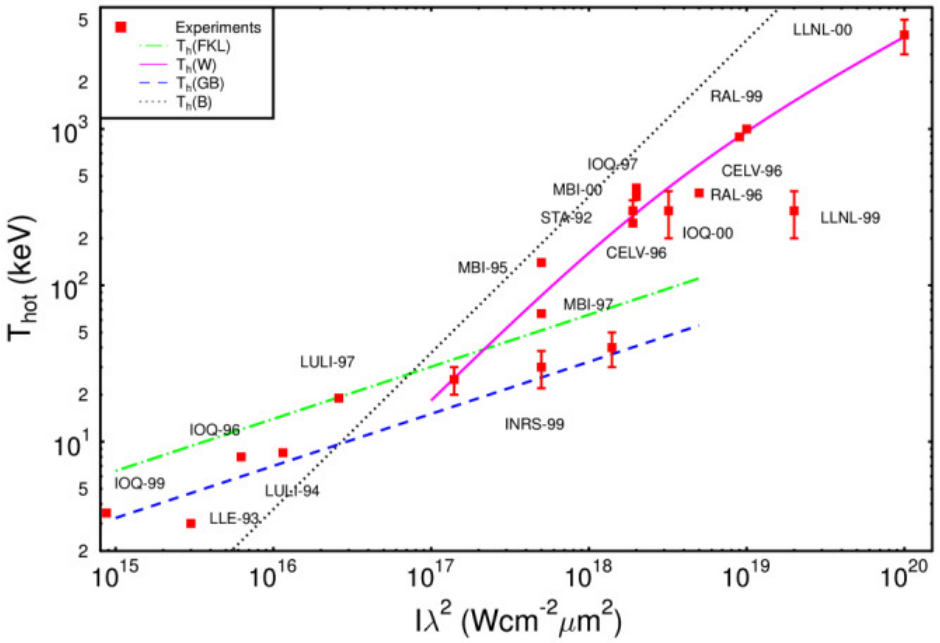

Figure 2.7: Hot electron temperature as a function of irradiance from sub-ps laser solid interaction experiments compared with various models, published by Gibbon [18]. Details on experimental data and scalings laws derived from different models are given in [18].

where I is the laser intensity (in $10^{18}\,\mathrm{W/cm^2}$) and λ the laser wavelength (in μm), both typical dimensions. The temperature is proportional to the ponderomotive energy [27] and equation 2.28 predicts a value for the hot electron temperature of $\approx 4\,\mathrm{MeV}$ for an intensity of $10^{20}\,\mathrm{W/cm^2}$ and a laser wavelength of $1\,\mu$m. This scaling is in good agreement with both, the experimental data for this regime (see figure 2.7) and 2D PIC simulations of laser interactions with step-like density profiles investigated by Wilks et al. [27]. These simulations show that the plasma surface is strongly influenced by hole boring processes and almost all energy is absorbed due to $\mathbf{j} \times \mathbf{B}$ and vacuum heating.

For different kind of applications, for example secondary scattering processes, the spatial and temporal physical parameters of the electrons become important and thus, a widely investigated topic in laser-plasma physics. The driving force of the dominant absorption process indicates a longitudinal oscillation at twice the frequency of the incident laser pulse. This oscillation leads to a periodic formation of dense electron bunches, gaining high energy before escaping the laser field [28]. Baton et. al [29] first observed this effect by the indirect measurement of the second harmonic laser light emitted from those electron bunches. More recently, theoretical investigations

were carried out describing the interaction of an high intense laser pulse with ultrathin (nano) foils, where all electrons are separated from the ions completely [30].

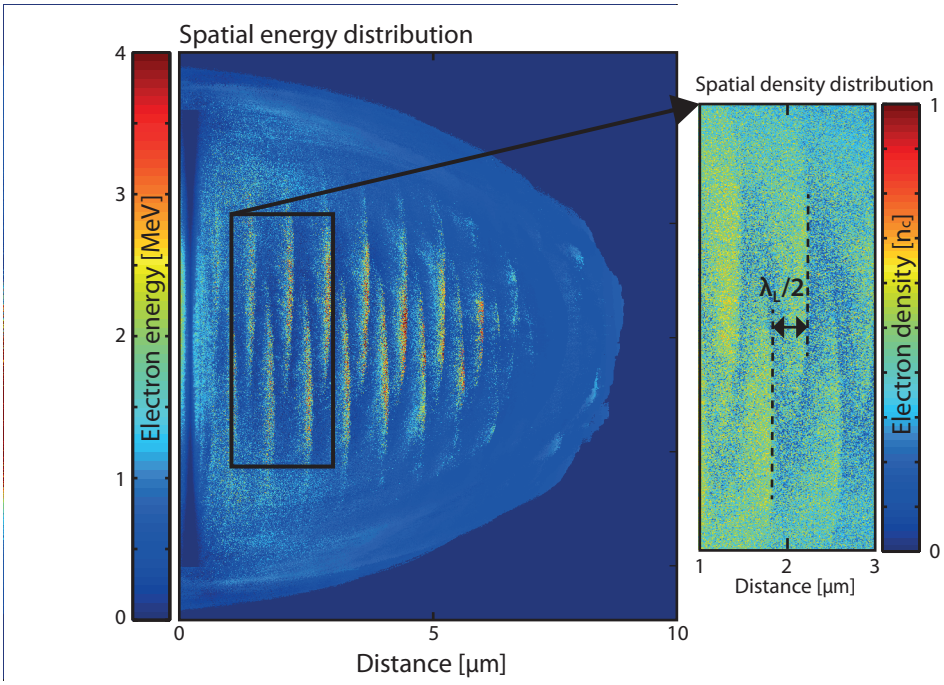

Figure 2.8: Simulation results from the interaction of a step-like laser pulse ($a_0 = 2$) with a 25 nm thin carbon foil. The image shows the spatial electron energy distribution 30 fs after the pulse hits the target. The spatial density distribution of the generated electron bunch formation is shown in the enlarged section on the right.

Figure 2.8 illustrates the simulation results from a step-like laser pulse with $a_0 = 2$ and $\lambda_L = 800\,\text{nm}$ incident on a 25 nm thin carbon foil at 30 fs after the main pulse arrived at the target surface. The spatial electron energy distribution indicates, that the high energetic electrons ($E_{kin} > 3\,\text{MeV}$) are accelerated in bunches. The section on the right shows the spatial electron density distribution of the energetic bunches in the red marked square. The bunches have a periodicity of $\lambda_L/2$ and reach densities near the critical density n_c. They are generated by the $\vec{v} \times \vec{B}$ force of the incident pulse and are driven through the remainder of the target. The electron sheets elude at the back side of the foil, while slowly dispersing due to their energy distribution.

2.6 Laser produced plasmas as a radiation source

The electromagnetic radiation emitted by hot plasmas has importance in two fields. Firstly, laser produced plasmas can be used as a direct source for X-ray beams with femtosecond pulse duration, to provide temporal resolution for microscopy of dynamic atomic-scale objects [31]. Secondly, the emission of hot plasmas can be of great interest for the characterisation of the properties of an ionised medium. The spectrum carries information about the plasma temperature and density conditions and thus is one of the most important diagnostics in the field of hot plasmas. Especially for fast processes, such as the interaction of an ultrashort laser pulse with matter, the emitted radiation is a signature for the evolution of the plasma [32].
The atomic physics, describing the processes which lead to the emission of the characteristic spectrum, is partly introduced in chapter 2.1 and 2.5. Here, the concepts are briefly summarised based on [32], emphasising the importance for the contribution to the emission spectrum recorded during the interaction of a laser pulse with a thin target.

2.6.1 Atomic processes in hot plasmas

Photoionisation occurs dominantly at the beginning of the interaction, when the target is still optically thick and the free path of the photons is shorter than the plasma dimensions. During the inverse process, called **radiative recombination**, radiation is emitted when an electron is captured in a bound state. For high Z material the efficiency increases as the coefficient rate is proportional to the ionisation potential of the bound electron.
In optically thin plasmas the **electron impact ionization** plays an important role. An electron with high kinetic energy encounters an ion and spalls one initially bounded electron. In high density plasmas on the other hand, the **three body recombination** is more likely, because the present of two electrons is required. One electron is caught by the ion while the other one gains its extra energy.
Autoionization and **dielectron recombination** involve two electrons in an excited level. While one electron decays to a lower level the second electron takes the released energy and is thereby freed into the continuum. During the inverse process a free electron is captured in an excited state, additional energy is transferred to a

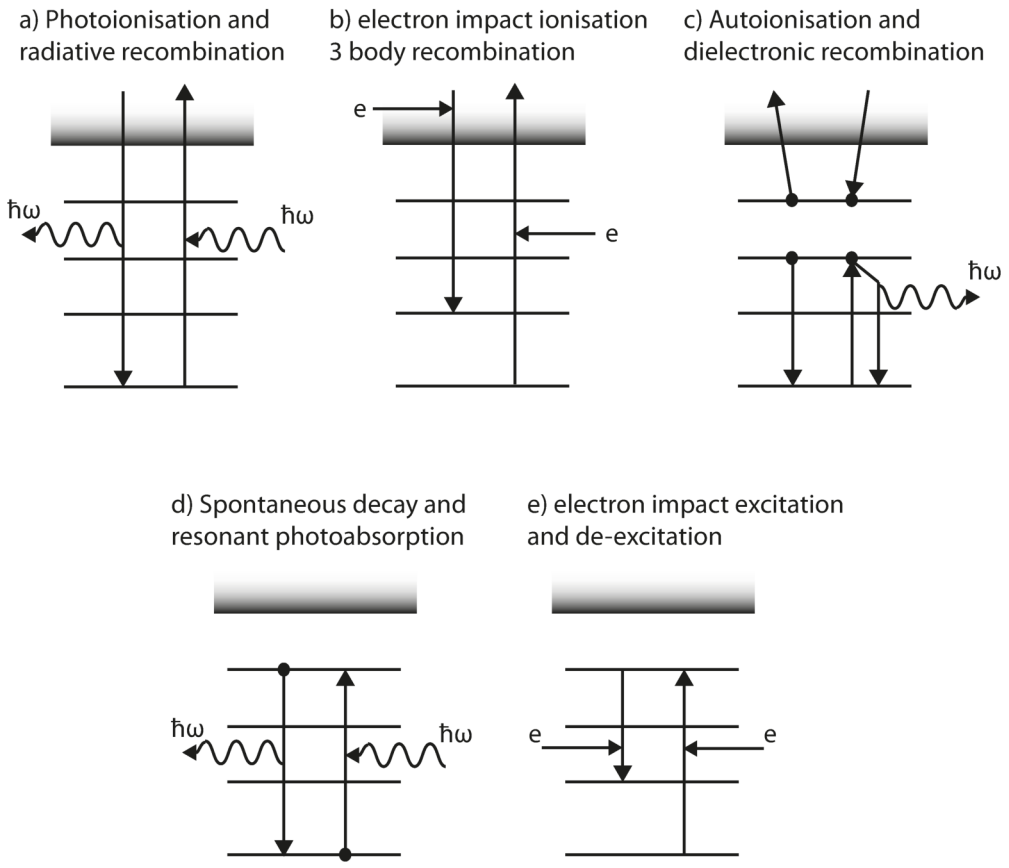

Figure 2.9: Schematic drawing of ionisation and excitation processes in hot plasmas based on [32]

bound electron which leads to the transition into a higher state. In case this electron decays back into the ground state, radiative stabilization is achieved and the emitted photon contributes to the features of the line spectra in form of satellites lines.

Spontaneous decay takes place when an ion of a higher state E_m decays into the ground or lower excited state E_n, emitting a photon with $E_p = E_m - E_n$. In the contrary, a photon with an energy equal to the energy difference between ground level and excited level or two excited levels is absorbed resonantly by the ion. As a single-particle process spontaneous decay does not depend on the density of the plasma. Moreover both processes follow the well-known Einstein coefficients describing the probability of spontaneous decay and **resonant absorption**.

Electron impact excitation is a process induced by the collision of an electron and an ion. Due to the collision the ion gets excited into an upper state while the electron experiences an energy loss. When the ion is already in an excited state the opposite process, **impact deexcitation**, can occur. The ion relaxes and transfers the energy to the electron. The efficiency of electron impact excitation is at a maximum when the plasma temperature is in the range of the transition energy. For higher temperatures the electron energy increases and becomes sufficient for ionization rather than excitation.

2.6.2 Emission Spectrum

The total emitted radiation intensity and spectral distribution of hot plasmas consist of two parts, the continuous spectrum and the line spectrum. Both parts are determined by the details of the emission process, the plasma temperature and its density.
Bremsstrahlung contributes with an exponentially decreasing function to the spectral structure of the continuous spectrum. It is produced when an electron is passing through the electric and magnetic field of an ion. Due to its acceleration in this field a photon is emitted. This mechanism is dominant for a low-Z plasma and for fully ionised higher Z plasmas at very high temperatures. However, for high-Z plasmas at low temperatures, the contribution of Bremstrahlung to the total emission spectrum is usually limited to a low continuous background signal.
Recombination radiation or free-bound radiation is emitted when a free electron recombines with an ion. This second type of emission, devoting to the continuous part of the spectrum, shows an edge structure corresponding to recombination into atomic states.

Particularly for intermediate and high-Z plasmas the spectral line emission, also called bound-bound emission, becomes prominent. Line emission occurs when a bound electron of an excited ion decays into a lower shell while emitting a photon with the transition energy $E_P = E_n - E_m$. While the radiation characteristics of high-Z plasmas can be rather complex, the spectra of ionized low-Z plasmas predominantly show spectral lines of hydrogenlike ions as well as heliumlike ions. Both species are well known and abundant in hot plasmas and therefore lines can be easily identified.

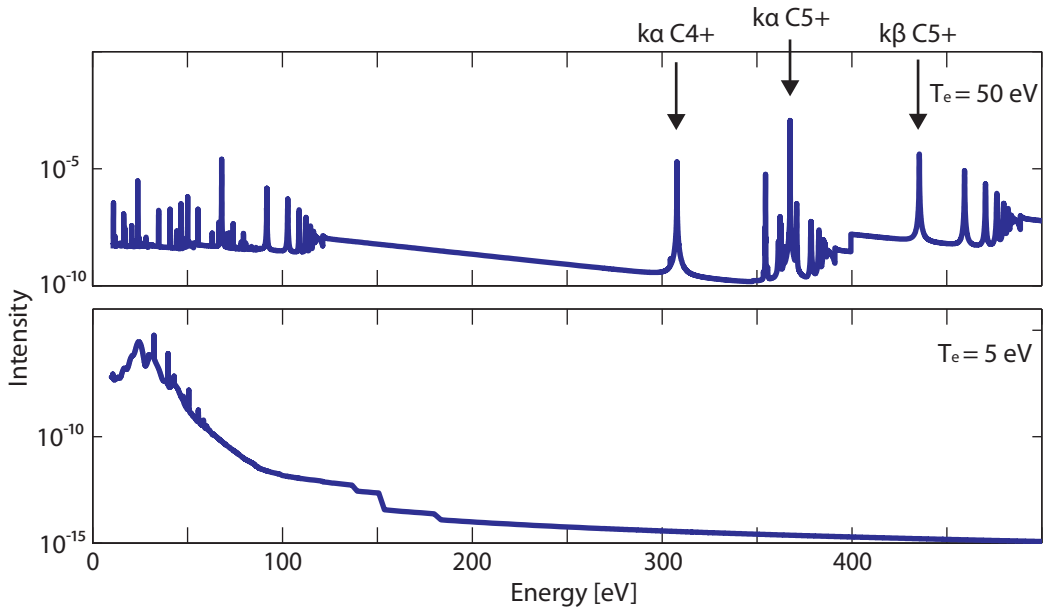

Figure 2.10: Comparison of simulated emission spectra of carbon at a density of $10^{19}\,\mathrm{cm}^{-3}$ and an electron temperature of $T_e = 50\,\mathrm{eV}$ (upper spectrum) and $T_e = 5\,\mathrm{eV}$ (lower spectrum). The line emission of hydrogenlike and heliumlike carbon becomes prominent as the high temperature is sufficient to ionise the carbon atoms.

The most probable transitions of an excited hydrogenlike ion are into the ground state $1s^1$. Simplifying the Bohr formula, energies of the Lyman series can be calculated with

$$\Delta E(Lyman) = Z^2 hcR_\infty(1 - \frac{1}{n}), \tag{2.29}$$

where R_∞ is the Rydberg constant. For hydrogenlike carbon with the atomic number $Z = 6$, the energy of the Lyman-α line, which originates from the transition of an electron from the second shell $n = 2$ to the ground state, becomes $6^2 * 13.6\,\mathrm{eV} * (3/4) = 368\,\mathrm{eV}$. This line can be found for example in the emission spectrum of the interaction of a high intensity laser pulse with a thin diamond-like-carbon foil (DLC). Figure 2.10 shows two emission spectra of carbon at different electron temperatures, generated by the computer code $FLYCHK$ [33]. The simulations are based on an electron density of $10^{19}\,\mathrm{cm}^{-3}$ and the spectra for a temperature of 5 eV (lower spectrum) and 50 eV (upper spectrum) are plotted. In the lower spectrum there is hardly any line emission visible, as the temperature is not sufficient to pro-

duce heliumlike or hydrogenlike carbon. Increasing the temperature by a factor of ten the spectrum changes significantly. The recombination edge structure is present and the emission lines of highly ionised carbon ($C4+$ and $C5+$) become prominent. Some dominant emission lines are marked by an arrow in figure 2.10, amongst these is the Lyman-α line of hydrogenlike carbon ($C5+$) at 368 eV.
The list of effects and mechanisms taking place in a hot plasma and contributing to the final emission spectrum is certainly not complete. Effects, like pressure ionisation, continuum lowering, satellites line emission, atomic level shifts or line pressure broadening are phenomena occurring in dense plasmas and are further describes in [32].

2.7 Thomson scattering

Classical Thomson scattering is a process, in which electromagnetic radiation scatters on a free charged particle with a total cross section of $\sigma = 6.65 \times 10^{-25}\,\mathrm{cm}^2$ [34]. While the magnetic field can be neglected in the non-relativistic case, the electric component of the incident laser field accelerates the particle in the direction of the oscillating field. The result is electromagnetic dipole radiation, which is emitted dominantly in direction perpendicular to its motion. In this linear process, the scattered frequency equals to the frequency of the incoming laser field. In a plasma, the scattering on electrons is most important as the ions are much heavier and their contribution is negligible. The condition for classical Thomson scattering is that the photon energy is much smaller than the electron rest energy ($h\omega \ll m_e c^2$), in order to preform inelastic recoils.
When the light intensity exceeds $10^{18}\,\mathrm{W/cm}^2$, the magnetic field component becomes relevant and the motion of the accelerated electron describes a figure of eight, as discussed previously in section 2.2. The quiver velocity of the electron in such a strong electromagnetic field approaches the speed of light. In this relativistic regime, the photons are scattered with a specific angular distribution and at harmonic frequencies of the incident laser field [35].

2.7.1 Thomson scattering and frequency upshift from laser accelerated electrons

An effective way to create an X-ray source is the scattering of a laser field on a bunch of relativistic electrons instead of a plasma. The result is a scattered spectrum, which is modified by the relativistic Doppler shift of the moving electrons. The relativistic electron beam can be generated by the interaction of a high intense laser beam with matter. Physical parameters, namely density, divergence and energy spectrum of the electron beam highly depend on the details of the acceleration mechanism and have a direct impact on the scattered X-ray beam. For instance, the interaction of a high intensity laser pulse with a thin foil is promising to deliver a near critical density electron sheath, resulting in a high number of back-scattered photons [36]. The electron acceleration from a gas jet on the other hand can provide a non-thermal energy distribution and therefore can lead to a narrower band X-ray source [37]. An adequate quantity to compare different X-ray sources is their brilliance, defined as

$$\text{Brilliance} = \frac{\text{photons}}{\text{second} \cdot \text{mrad}^2 \cdot \text{mm}^2 \cdot 0.1\%\text{BW}}. \tag{2.30}$$

It embraces important properties, in particular the photon flux, the beam divergence and the X-ray source size.

Frequency upshift

The relativistic Doppler shift describes an alteration in wavelength and amplitude of an electromagnetic wave, which is reflected of a relativistic, fast moving source and was first mentioned in the work of Einstein [38]. The following description is based on [39] and is pictured in figure 2.11 in two different frames of reference. The reflection takes place on the boundary of two media with the refractive index n_1 and n_2. The second medium can be for example a relativistically moving plasma slab with an electron density $n_{e,2}$ and a velocity $c\beta$, acting as the reflective source. Figure 2.11 a) illustrates the laboratory frame of reference $\boldsymbol{L}$, in which the electromagnetic wave with frequency ω_0 and wave vector $\mathbf{k}_0$ is propagating through medium 1 under an angle of θ_i towards the plasma slab. The rest frame of reference $\boldsymbol{R}$, where the plasma slab does not move is drawn in b). In this situation, the reflection of the wave follows the classical Snell's law, which describes the relation between angles of

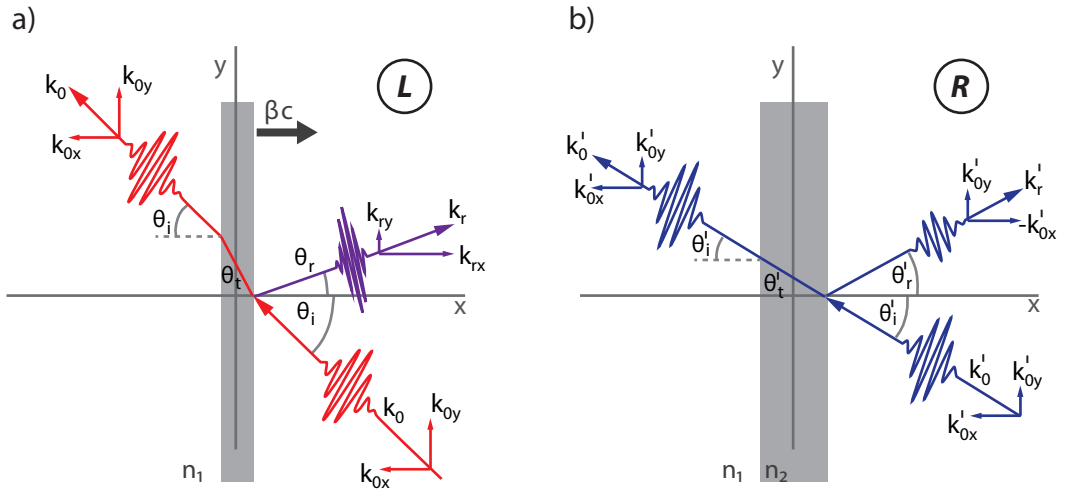

Figure 2.11: a) Reflection of an electromagnetic wave on a plasma layer with refractive index n_2. The plasma layer is moving with velocity βc along the x axis in the laboratory frame of reference $\boldsymbol{L}$. b) The reflection is illustrated in the rest frame of reference $\boldsymbol{R}$ of the plasma layer. The schematic is based on [39].

incidence and refraction at a boundary between two media with refractive index n_1 and n_2:

$$\theta_i' = \theta_r' \frac{sin(\theta_t')}{sin(\theta_i')} = \frac{n_1'}{n_2'}. \tag{2.31}$$

If the two media are plasmas, the refractive index can be replaced with equation 2.18 and the expression 2.31 changes to

$$sin(\theta_t') = sin(\theta_i') \sqrt{\frac{1-(\omega_{p,1}/\omega')^2}{1-(\omega_{p,2}/\omega')^2}}, \tag{2.32}$$

where $\omega_{p,1/2}$ is the plasma frequency of the two media and ω' is the wave frequency in $\boldsymbol{R}$. The wave parameters in $\boldsymbol{R}$ are related to the once in $\boldsymbol{L}$ by the Lorentz transformation [34]

$$\begin{aligned} \omega' &= \gamma(\omega_0 + k_{0,x}\beta c), \\ k_x' = \gamma(k_{0,x} + \omega_0 \beta/c), \;\; k_y' &= k_{0,y}, \end{aligned} \tag{2.33}$$

with the relativistic Lorentz factor of the plasma slab $\gamma = 1/\sqrt{1-\beta^2}$. The incidence and reflection angles in $\boldsymbol{L}$ can be expressed by $sin(\theta_i) = k_{0,y}/k_0$ and $sin(\theta_r) = k_{0,y}/k_r$. To find the frequency of the reflected wave in the laboratory frame of reference $\boldsymbol{L}$, another Lorentz transformation from $\boldsymbol{R}$ to $\boldsymbol{L}$ has to be performed, considering the change in sign of the x component of the wave vector. Including the expressions for θ_i, θ_r and the result of the first Lorentz transformation (eq. 2.33), the reflected frequency becomes

$$\omega_r = \frac{\omega_0(1+\beta^2) + 2\beta\sqrt{\omega_0^2 - \omega_{p,1}^2}cos(\theta_i)}{1-\beta^2}. \tag{2.34}$$

For a counter-propagating geometry ($\beta > 0$), the electromagnetic wave experiences a frequency upshift accompanied by a compression of the pulse and an increased wave amplitude in the laboratory frame of reference $\boldsymbol{L}$. If, in addition, medium 1 is a vacuum ($\omega_{p,1} = 0$) and the angle of incidence of the wave is normal to the plasma slab ($\theta_i = 0$), the reflected frequency simplifies to

$$\omega_r = \omega_0 \frac{1+\beta}{1-\beta} = \omega_0(1+\beta)^2\gamma^2 \approx 4\gamma^2\omega_0. \tag{2.35}$$

The latter part of the equation becomes valid in the ultra-relativistic limit $\gamma \gg 1$, where $\beta = v/c \approx 1$.

An extensive theory for the description of Thomson scattering was developed by Esarey et al. [40], starting with the Lienard-Wiechert potential in order to calculate the energy spectrum of the radiation emitted by a single electron. A detailed derivation is given, leading to a reflected frequency of

$$\omega_r = \frac{4\gamma^2\omega_0}{1 + a_0^2/2 + \gamma^2\phi^2}. \tag{2.36}$$

The results for the reflected frequency ω_r given in equation 2.35 are confirmed and supplemented by the dependency on the radiation cone angle ϕ.

Scattered number of photons

The total radiated power emitted by an accelerating charge is calculated with the *Larmor formula*. For the case of a relativistically moving source one can use its relativistic generalisation [34]. The description below follows closely the derivations

of Ride et al. [41], who applied this concept to determine the scattered photon flux per electron in an intense laser field. Firstly, the motion of an electron in a laser field is described by the Lorentz equation 2.7. Here the normalised electron momentum $\boldsymbol{u} = \boldsymbol{p}/m_e c = \gamma\boldsymbol{\beta}$ and the normalised electron velocity $\boldsymbol{\beta} = \boldsymbol{v}/c$ are used.
The motion of interest, when the electron and the electromagnetic wave are counter-propagating, is the laser direction. Assuming the laser field, with the wave number $k_0 = 2\pi/\lambda_0$ is propagating along the z-axis the average axial electron velocity is stated as

$$\bar{\beta_z} = \frac{\beta_{z0} - a_0^2/(4\gamma^2(1+\beta_{z0})}{1 + a_0^2/(4\gamma^2(1+\beta_{z0})}, \tag{2.37}$$

where a_0 (eq.2.9) is the normalised amplitude of the incident laser field.
For the derivation of the total radiated power, the relativistic Larmor formula

$$P = \frac{2e^2}{3c}\gamma^2 \left[\left(\frac{d\mathbf{u}}{dt}\right)^2 - \left(\frac{d\gamma}{dt}\right)^2 \right], \tag{2.38}$$

is introduced, where e is the electron charge and c the speed of light. The quantities $\boldsymbol{u}$, $\boldsymbol{\beta}$ and γ are functions of the variable $\eta = z + ct$ and the Lorentz equation implies the constant of motion $d(\gamma - u_z)/d\eta = 0$. This assumption and time averaging over a whole laser period leads to the approximation for the radiated power

$$P \approx \frac{1}{3} e^2 c k_0^2 a_0^2 \gamma_0^2 (1+\beta_{z0})^2. \tag{2.39}$$

The radiated photon frequency is given in equation 2.36, thus the average energy can be written as

$$\hbar \langle\omega\rangle = \frac{2(1+\beta_{z0})\gamma_0^2}{(1+a_0^2/2)} \langle n\rangle \hbar\omega_0, \tag{2.40}$$

with the average harmonic number $\langle n\rangle$ and $\gamma_0 \gg 1$. In order to gain information about the total number of photons, the flux can be determined by dividing the photon power (eq. 2.39) by the average photon energy (eq. 2.40). Finally the flux is multiplied by the interaction time

$$T = \lambda_0 N_0/(1+\bar{\beta_z})/c, \tag{2.41}$$

where N_0 is the number of laser periods during the interaction. The result is the

number of radiated photons per electron:

$$N = \frac{\pi}{3}\alpha N_0 a_0^2 \frac{(1 + a_0^2/2)(1 + \beta_{z0})}{\langle n \rangle (1 + \bar{\beta}_z)}, \tag{2.42}$$

where α is the fine structure constant. In the case of a laser based electron source, there are N_e electron involved, and consequently the total number of photons is the product of N and N_e.

Laser setup, diagnostics and experimental techniques

This chapter is dedicated to present a description of the laser system, its specific parameters and the experimental techniques utilised during the experimental campaigns. Furthermore the diagnostics for both, the interaction itself and the detection of the radiation generated through the process are explained. Relevant aspects are the characterisation of the electrons accelerated by the high intensity laser pulse and the detection of the X-rays, which are either generated by scattering processes of laser light on these electrons or originate from the hot dense plasma itself. Therefore the underlying physical concepts of the corresponding diagnostic are introduced and finally the utilized spectrometers and detectors are described.

3.1 Arcturus laser system

The versatile high power laser system ARCTURUS, situated at the Heinrich Heine University in Düsseldorf is a double *chirped pulse amplification* (CPA) system equipped with a *cross-polarised wave* (XPW) module for additional contrast enhancement. It is capable of delivering three independently compressed beams into the target chamber, enabling optimum flexibility in the setting of experimental parameters. The two main beams have up to 6 J laser energy during a 30 fs long pulse. This leads to a laser power of 200 TW at a central wavelength of 800 nm with a repetition time of theoretically 10 Hz. The third low power beam (10 TW) can be additionally applied as a probe beam.
The system uses the CPA technique developed by Donna Strickland and Gerard

Mourou [42] which was a milestone in the history of high power laser systems. This technique implies a stretching in time of an ultra short laser pulse with low energy (nJ). This is to keep the intensity low, in order to avoid nonlinear effects on the optical systems, for example damages or breakdowns of the laser pulse in air. Finally, the amplified laser pulse is compressed again to provide the high power output.

At the ARCTURUS laser system all beams originate from a Kerr-lens mode-locked

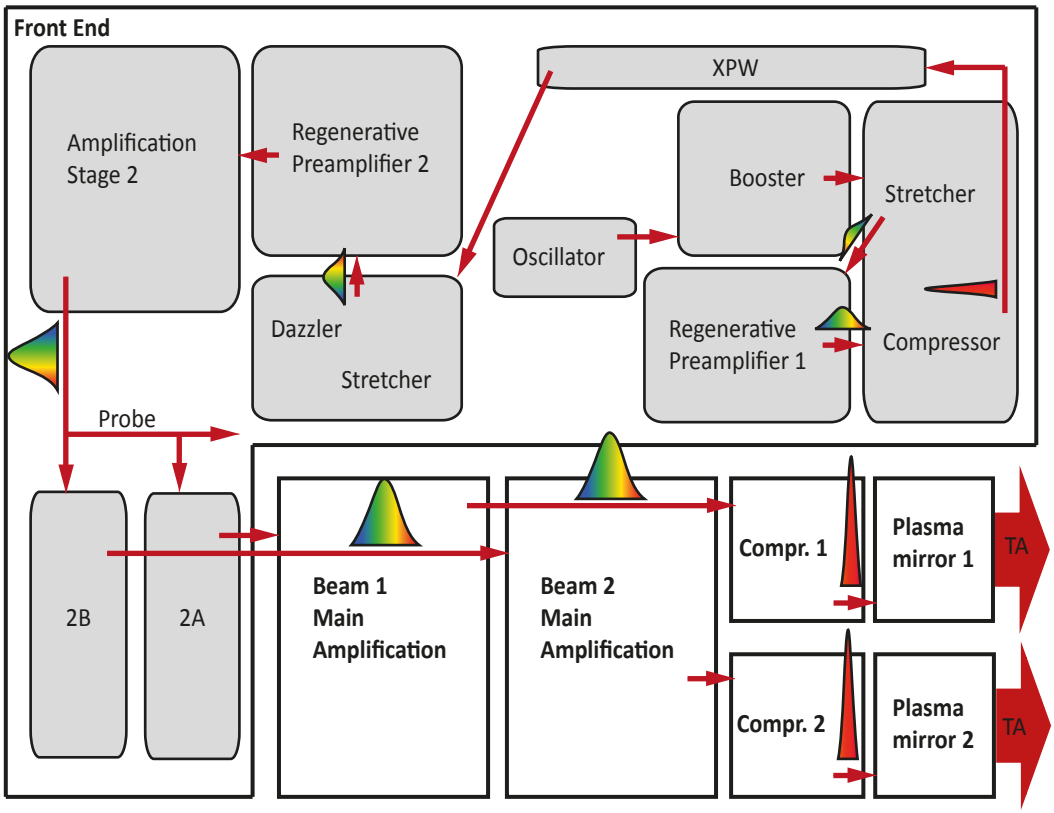

Figure 3.1: A simplified overview of the Arcturus laser system. The laser pulse is generated in the oscillator, preamplified and its contrast is enhanced in the XPW module. There are two more amplification stages before the pulse is split into three parts, two main beams and a probe. The main beams are further amplified and finally compressed before they are sent to the target area.

Synergy Ti:Sa Oscillator, which generates ultra short pulses (25 fs) with low energy (5 nJ) at a repetition rate of 75 MHz. The central wavelength of these pulses is 790 nm, with a spectral bandwidth of 96 nm. Mode locking of the oscillator provides this particular frequency spread, which acts as a limit to the minimum duration of the pulse. Focusing these pulses leads to intensities too low for most recent research

fields, consequently an amplification of the laser pulse is required. The pulse is guided through a booster amplifier and experiences a gain of 10^4, being picked at 10 Hz by a pockels cell. A saturable absorber is responsible for cleaning the pulse of unwanted amplified spontaneous emission (ASE). The next step is a first CPA in combination with a cross-polarised wave (XPW) module in order to pre-amplify and enhance the contrast of the laser pulse. The pulse is optically stretched and injected in a regenerative cavity amplifier. The result is a 1 mJ energy pulse, which is compressed to 40 fs and guided through the XPW module. This method improves the contrast ratio of the Arcturus laser system from originally 10^{-9} without XPW module to now 10^{-12} on ns time scale. The pulse leaving the XPW becomes the seed pulse for the second, conventional CPA stage. Lengthened to a pulse duration of $\sim$ 750 ps by a stretcher module, the pulse is shaped in phase and amplitude by an acousto-optical dispersive filter called Dazzler. During the amplification process, a reduction in the bandwidth usually occurs; this is known as gain narrowing. To avoid this effect, the Dazzler introduces spectral losses on the central part of the spectrum and broadens the spectrum for efficient amplification. The amplification chain starts with a regenerative pre-amplifier, in which the pulse runs multiple passes through a Ti:Sa crystal. In a second amplification stage the pulse reaches an energy of 300 mJ and is then divided into three parts, a probe beam and two main beams (beam 1 and beam 2). The probe beam is guided directly into a delay setup, before entering the compressor. This is required for the compensation of missing beam path in comparison to the two main beams which undergo several multi-pass, butterfly amplifiers. Each amplifier contains a cooled Ti:Sa crystal pumped by frequency doubled Nd:YAG lasers. In the first amplification stage ($2A$ and $2B$) after splitting the beam the energy is increased to 300 mJ. The following main amplifiers boost the energy up to a maximum of 6 J. This can be attenuated by reducing the pump power, thus enabling each beam to be individually tuned for different experimental requirements.
During the amplification process the beam diameter is expanded in order to keep the fluence on the optics below their damage threshold. The 80 mm diameter beams are temporally compressed in two separate vacuum compressors to a minimum pulse duration of 25 fs and are finally guided through vacuum beam lines into the target area (TA) and the experimental chambers.

3.1.1 Laser pulse contrast

The laser pulse contrast is the ratio of the laser peak intensity to the intensity of the ASE pedestal background. The ASE pedestal originates mainly from the preamplifier in the laser system and is generated by spontaneous emission, which is further amplified by the main amplifiers. The parameter laser pulse duration describes the temporal length of the main high intensity peak. The entire temporal profile of the laser pulse however, discloses a complex time structure. It contains the ASE pedestal before the main pulse arrives and some additional pre and post pulses. It can be experimentally measured, typically in a pico- to nano second time scale. Current laser systems, without additional contrast improvement modules, deliver pulses reaching $6-9$ orders of magnitude contrast in ns time scale [43].
The leading edge of such a laser pulse has intensities well above the ionisation threshold and interacts with the target before the main pulse arrives. The result is a pre ionised material or, in case of ultra thin solid foils, the target can be completely destroyed. Effects of the so called pre-pulse on interaction and the following acceleration processes are an interesting part of the research in Laser-plasma physics on its own [44] [45]. The experiments carried out in the context of this thesis require additional pulse cleaning to avoid these effects.
Two methods, which are implemented in the ARCTURUS laser system are introduced in more detail. The first one, the XPW module is implemented at the front end of the laser system, whilst the second method, the plasma mirror setup improves the contrast for each main beam individually after the final compression.

XPW generator

Cross-polarised wave generation is a nonlinear filtering technique, producing a wave with the same wavelength as the input pulse. The temporal profile of the output wave has a cubic dependence on the input pulse profile, which makes this technique successful in the enhancement of the temporal contrast of femtosecond laser pulses [43]. A XPW generator consists of two crossed polarisers and in between a nonlinear crystal (BaF_2 crystal). A linear polarised laser pulse is focused onto the crystal; a new wave is generated, which is orthogonally polarised to the input pulse. As the conversion is more efficient for high intensities, the ASE background is drastically suppressed.

Plasma mirror setup

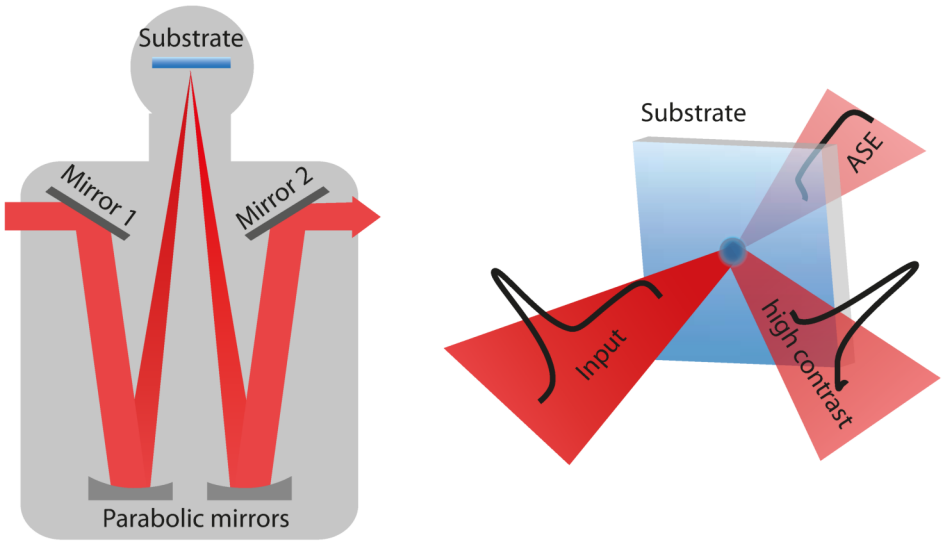

Figure 3.2: Schematic of a plasma mirror setup (left) and the working principle (right). The laser pulse is focused by a parabolic mirror onto a subtrate, which becomes instantly reflective when the rising edge of the main pulse starts to ionise it. The reflected high contrast laser pulse is re-collimated by a second parabolic mirror.

In the plasma mirror setup (figure 3.2) the compressed laser pulse is reflected by mirror 1 onto an off-axis parabola. The pulse is focused onto a dielectric optically flat glass substrate, which has an anti reflective coating. The low intensity ASE pedestal and prepulses go through the substrate, which is transparent for the laser wavelength. The rising edge of the main pulse reaches intensities sufficient to ionise the substrate. A reflective plasma sheet is triggered by the laser pulse itself and acts as a mirror, which reflects most of the subsequently arriving main pulse. A second off-axis parabola re-collimates the beam and it is finally redirected by mirror 2 into the beam line. As a positive side effect, possible reflections from the interaction area, which are guided back through the beam line towards the front end are stopped at the damaged substrate surface.

Figure 3.3 depicts the temporal laser pulse profile of the ARCTURUS laser system, including the XPW module. 60 ps before the intensity peak, the laser pulse contrast is 10^{-10}, which is one magnitude higher than the contrast without XPW module (before

the ARCTURUS upgrade in 2013). A contrast measurement of the pulse after the plasma mirror is challenging, as for each shot the damaged substrate surface has to be moved and the limit of the dynamic range of the measuring device is exceeded. Nevertheless, the contrast improvement by using a plasma mirror can be estimated to be two orders of magnitude, which adds up to a final contrast of 10^{-12} on a hundreds of ps time scale.

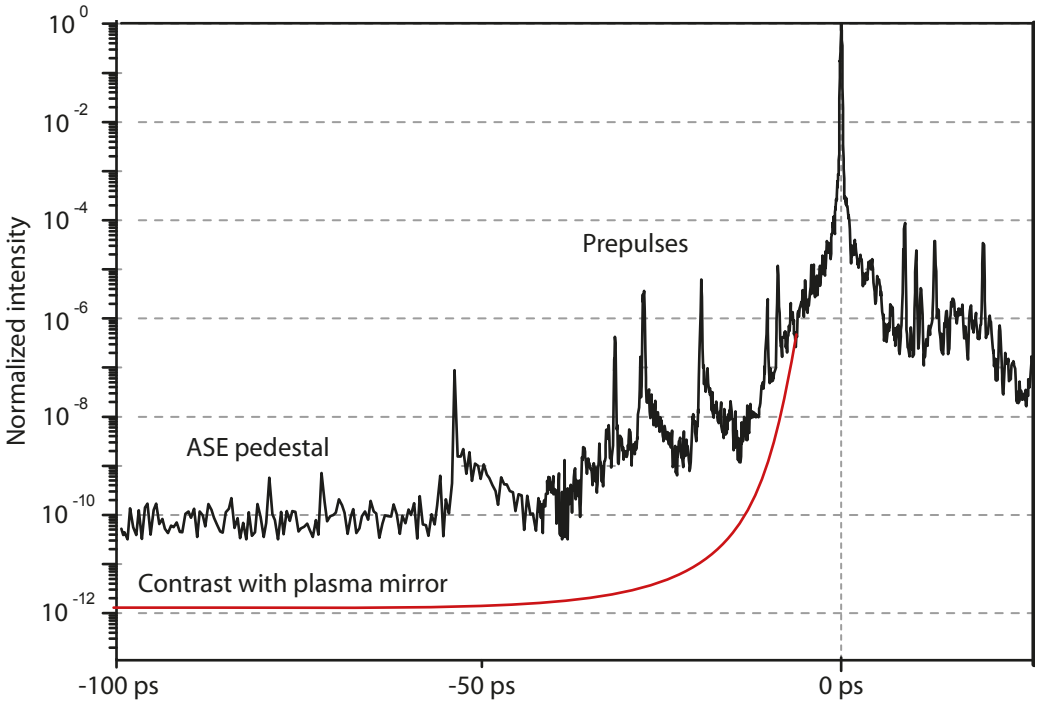

Figure 3.3: Temporal profile of the laser pulse of the ARCTURUS laser system. The contrast is 10^{-10} on a hundreds of ps time scale. Implementing the plasma mirror enhances the contrast up to 10^{-12}.

3.2 Diagnostics and techniques

For both experiments, discussed in this thesis, a high intense laser pulse is used to accelerate electrons from a target (gas or solid). On these electrons a counter-propagating laser pulse is scattered, generating X-rays via Thomson scattering. Figure 3.4 shows a schematic valid for both setups, emphasising the diagnostics in use which can be divided into two groups: diagnosis of the interaction area and detection

of generated radiation.

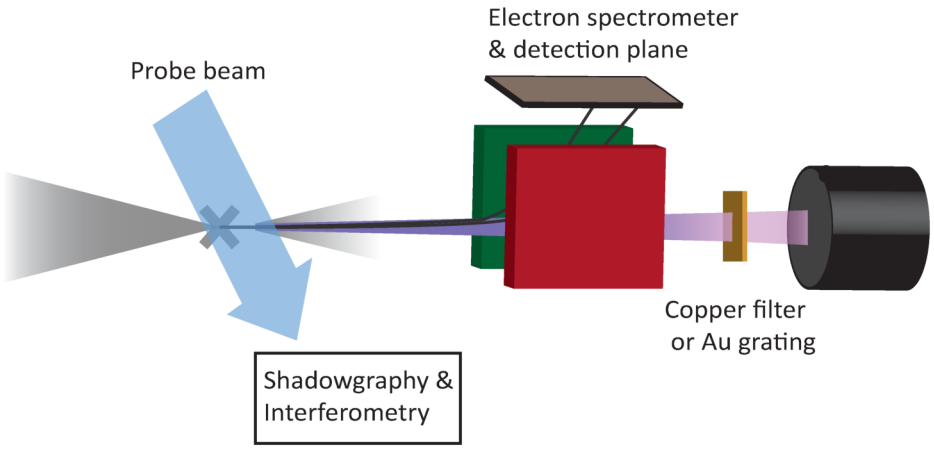

Figure 3.4: Schematic of the experimental arrangement of the diagnostics used during the campaigns in connection with this thesis.

The interaction itself, particularly the target conditions, including density (gas target) or expansion velocity (solid target) are diagnosed by *optical probing*. A collimated probe beam is sent orthogonally to the interaction beam through the interaction area. The modifications are captured on a CCD camera by an *interferometric* or *shadowgraphy* setup.
The accelerated electrons are measured by an *electron spectrometer*. They are deflected by a magnet and detected, energetically resolved, on a *lanex screen* (online) or an *image plate* (single-shot). The X-ray detection method depends on the expected spectral range of the generated radiation. For soft X-rays ($100\,\mathrm{eV} - 5\,\mathrm{keV}$) a *transmission grating*, which diffracts X-rays onto an Andor camera is used. Hard X-rays ($10\,\mathrm{keV} - 200\,\mathrm{keV}$) are attenuated in dependence on their energy by a set of copper filter and captured by a *Photonic camera*, which is sensitive in this range.

3.2.1 Optical probing

The interaction of ultra short, high intensity laser pulses with matter leads instantly to the creation of a plasma. The evolution of the characteristic parameters, for example the plasma density and temperature, happens on a *ns* time scale. At the early stage of this interaction, the characteristics are mainly determined by the con-

tribution of the electron density. For this reason, diagnostic techniques capable of measuring the electron density variation become important.
The optical probe technique is a diagnostic based on the propagation of a probe beam through the plasma [46]. The beam profile is modified due to the variation of the refractive index within the plasma. The refractive index

$$\eta(x,y,z,t) = \sqrt{1 - \frac{n_e(x,y,z,t)}{n_c}} \cong 1 - \frac{n_e(x,y,z,t)}{2n_c} \tag{3.1}$$

is a function of the electron density and of the critical density and therefore dependent on the probe wavelength. The variation of the refractive index and therefore plasma parameters, such as the electron density, can be obtained by the measurement of the modifications (e.g. phase variations) induced on the probe beam. The probe pulse duration determines the temporal resolution of the diagnostics.

Interferometry

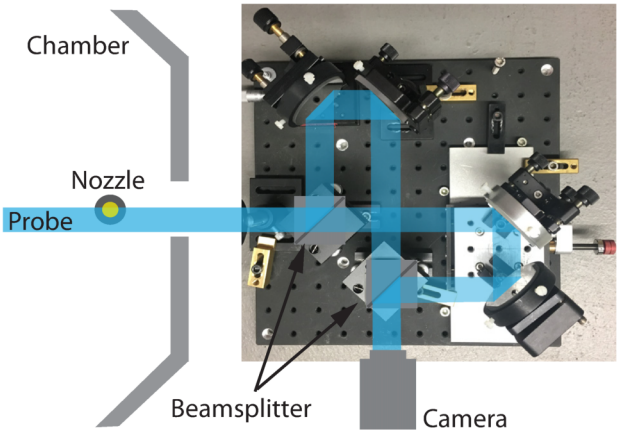

Figure 3.5: Mach Zehnder interferometer as used in order to measure the density distribution of a gas jet.

A practical approach to capture these modifications is the interferometry [47]. The probe beam, crossing the plasma and a non-influenced reference beam, traveling the same distance, are brought to interfere on a detection plane. The resulting fringe pattern contains information about the electron density present at the time the probe

beam passed through the plasma or gas. The technique is of great interest when experimenting with gas jets, using different background pressures, as the density of these jets is an important parameter in the electron acceleration process.
There are several possible configurations to implement interferometry as a diagnostic [47]. Figure 3.5 shows the Mach Zehnder interferometer, that is used to measure the density distribution in the jet and the temporal response of the valve during the experimental campaign described in chapter 4.1. A continuous wave laser (400 nm) is expanded and directed slightly off center through the interaction area. The probe exits the vacuum chamber through a glass window and is divided by a beam splitter into two parts. Both beams are reflected at two mirrors, before the beams recombine. Finally, the beams are individually aligned in such way, that the reference part of one beam interferes with the distorted part of the other beam on a CCD camera.
The spatial and temporal variation of the refractive index η is a function of the electron density. The propagation of the probe beam through the expanding gas leads thus to an additional phase shift $\Delta\Phi(x,z)$ of the probe beam with respect to its propagation in vacuum, for the same distance. Phase extraction from the interferometric data is therefore an important step in the analysis. This is achieved by measuring the fringe displacement from their unperturbed position [48].
The mathematical treatment involves a Fourier transformation of the intensity profile of the raw data (figure 3.6 a)) along the z-axis. The inverse Fourier transformation is applied to the component of the spectrum, where the phase information is stored. Finally, the phase (figure 3.6 b)) can be deduced from the ratio of the inverse Fourier transform of the signal and the reference case. The phase shift

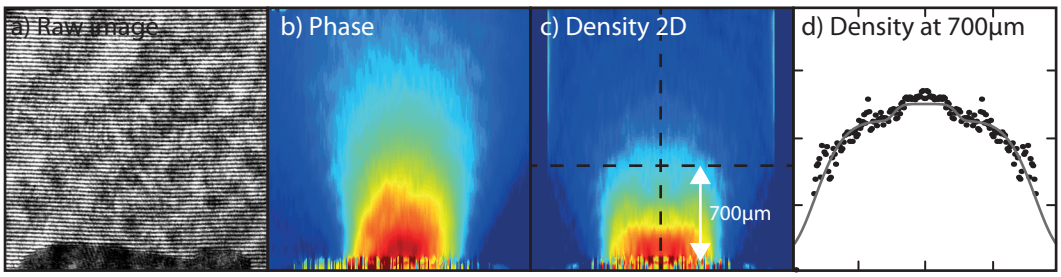

Figure 3.6: Process of the interferogram analysis. From the raw data (a), the phase information (b) is extracted via Fourier transformation. The 2D density plot (c) can be obtained after an Abel inversion of the phase shift. A line out of the density map provides information about the density at a specific height (d) above the nozzle.

$\Delta\Phi(x,z) = \int_L(\eta(x,y,z) - 1)\frac{\omega_P}{c}dy$ is proportional to the integral of the refractive index along the optical path length (y-axis). Considering the cylindrical symmetry of the gas jet, the integral becomes analytically solvable by an Abel inversion [48]. The final density is plotted in 2D (figure 3.6 c)). To obtain the specific density profile, at the position where the focused laser beam interacts with the gas jet, a line out is taken (figure 3.6 d)).

3.2.2 Shadowgraphy

Transverse optical shadowgraphy is one of the simplest optical probing techniques, in which the shadow of the plasma is imaged along the probe line. The probe light is not able to propagate through the region, where the refractive index is higher than the critical density, this causes a shadow in the recorded image. An optical lens is installed to collect the probe rays and to focus them onto a CCD camera with a magnification of 10. The probe pulse is converted to 2ω by a BBO crystal, in order to be able to block ω light of other sources from reaching the detector. The visible signal is proportional to the second derivation of the refractive index. The diagnostic is often used to analyse the plasma expansion rather then gaining quantitative information about the electron density. However, the expansion velocity can be derived from shadowgrams by measuring the spatial evolution of the shadow edge at different times.

3.2.3 Electron spectrometer

An electron spectrometer is a magnetic yoke with two detection planes, one on the top and the other one on the back of the magnets. It is used to record energetically resolved electron spectra in high power laser plasma experiments.
The deflection of a charged particle in a homogenous magnetic field depends on its kinetic energy E. More specific, the trajectory of a particle with the charge q and mass m describes a circle with the energy dependent radius

$$R = \frac{m\gamma\beta}{qB} = \frac{m}{qB}\sqrt{(1+\frac{E}{E_0})^2 - 1}, \tag{3.2}$$

called the Larmor radius [49], where E_0 is the electron rest energy. The magnetic field B is therefore causing a dispersion of a bunch of energetically broad distributed

electrons in space.

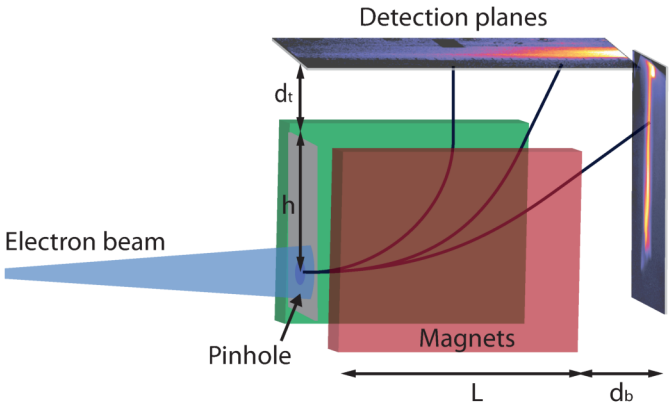

Figure 3.7: Schematic drawing of an electron spectrometer. Electrons enter the magnet through a pinhole and are deflected due to the magnetic field in dependency of their energy. They are detected above and behind the magnet by an electron sensitive screen.

Figure 3.7 shows a schematic drawing of the working principle of an electron spectrometer. The entrance of the spectrometer is covered by a layer of plastic and lead with a pinhole in the middle of the magnetic yoke. A small pinhole diameter improves the energy resolution of the system. However, the minimum size is defined by the flux, which is necessary to obtain a decent signal on the detector plain. Electrons, which enter the spectrometer through the pinhole, are deflected by the magnetic field. When they exit the yoke, they follow a linear motion with a constant velocity. The detection plane can be either at a certain distance d_t on top and d_b behind the magnet or directly attached to the magnet. Commonly used for the detection are phosphor screens, which instantly emit light, that is imaged by a CCD camera (online) or image plates, which store the information. The latter are read out by a scanner after each radiation process and can be analysed quantitatively.
The electron spectrometer, used for the measurements presented in chapter 4.1, is designed for high energetic electrons up to 150 MeV. Two 20 cm long and 10 cm high neodymium magnets are mounted, with a 1 cm gap between them, in an iron yoke configuration. The resultant homogenous magnetic field within the yoke is measured with a hall probe and is 400 mT. The 5 mm pinhole is surrounded by 2 cm thick plastic and 1 cm thick lead, in order to block high energetic electrons, which are not on the laser axis. The electrons are detected at a distance $d_t = 18$ cm on the top and

$d_b = 17\,\text{cm}$ behind the exit of the spectrometer on a phosphor screen.
To measure a lower energetic energy range up to 10 MeV, the gap between the magnets can be increased. For the experiment described in chapter 4.2 two neodymium magnets ($10 \times 7.5\,\text{cm}$) are arranged with 4 cm space between them and the magnetic field in the center reaches 150 mT. During shooting sessions a phosphor screen is mounted directly on top of the magnet and the spectrometer is used as an online diagnostic. However, for each target type, the electron distribution of some shots are recorded on image plates in order to gain quantitative information on the electron flux. During these shots, a 3 mm pinhole limits the entrance of the spectrometer, consequently a resolution of less than 10 % is achieved.

Phosphor Screen

The working principle of a lanex screen is based on the scintillating layer. When an energetic photon or a charged particle penetrates, it excites the phosphor molecules by collisions. The absorbed energy is re-emitted in form of green light, which can be captured by a CCD camera looking onto the screen.
When focusing an intense laser pulse onto a gas jet, the shot to shot fluctuation of the accelerated electrons, in particular their flux and energy distribution, can be rather strong. This kind of experimental campaigns require an online diagnostic for the recording of the electron spectrum and a lanex screen is most suitable as the detecting element.
The active layer of the lanex screen (KODAK Biomax MS) is protected by 15 μm thick aluminium in order to block unwanted laser light. The energy deposited in the phosphor layer by the electrons is proportional to the amount of energy of the light re-emitted by the screen in the visible range. A calibration of the same lanex screen, which is used during the experiments described in this thesis, shows that above 3 MeV the deposited energy becomes nearly independent of the incident electron energy and therefore depends only on the number of electrons [50]. The emitted light of the screen follows a cosine distribution, and to determine the total number of electrons it is crucial to measure all of the scintillation signal [50]. The camera, looking at the detection screen, is usually installed outside of the chamber. Thus is it not straight forwards to gain quantitative information from the images recorded. However, a qualitative energy distribution can be easily found by taking the line out

of the traces the electrons generate on the screen.

Image plates and flux determination

An image plate is a flexible sensor, which contains a photostimulable storage phosphor layer. When the molecules in this layer are struck by ionising radiation (e.g X-rays or charged particles), electrons are elevated into higher energetic levels, where they become trapped. This metastable state remains until lower-frequency light returns the trapped electrons to the conductive band, where they relax to their original state while releasing photons in the visible range [51]. In practice, the reading out process is operated by a laser scanner, which performs photostimulated luminescence (PSL) and captures it in discrete pixel values. The PSL signal is proportional to the number of incoming charged particle and therefore an essential detection method for quantitative measurements of laser plasma generated electrons.
In comparison to a lanex screen, which emits a signal instantaneously and only for a few milliseconds, an image plate (IP) is a one-shot-only diagnostic. Irradiated by charged particles, the information is saved long enough to be read out typically after 80 min, when the fading process of the IP stops and the signal stays constant over several hours [52]. During the read out process the total signal stored on the IP can be obtained. With the lanex screen however, the fluorescence is captured with a CCD camera, often far away from the screen and thus does not contain all photons emitted by the screen. For the experiment discussed in Chapter 4.2, BAS-TR2040 IPs containing a 50 μm thick sensitive layer are used and scanned by a Dürr medical CR 35 BIO scanner. In the scanner, a HeNe scanning beam is releasing the trapped electrons and the PSL signal accompany this process is detected by a photo multiplier, transforming it into a 16 bit grey value image with a pixel size of 25 μm. The dynamic range of the image plates is in the order of 10^5, while the range of the read out system is lower. However, the IPs can be read out several times to gain all the information stored and the total signal can be reconstructed considering the signal decay after each scan [53]. The exponential decay function after n scans, using the CR 35 BIO scanner, is measured to be [54]

$$L_n = 0.999 + 1.8279 \exp \frac{-n}{1.4027}, \tag{3.3}$$

where L_n is the ratio of the signal intensity of scan n to the intensity of scan $n = 1$.

The energy dependent spatial distribution of an electron beam is captured on a stratified stack, alternating different layers of aluminium filter and IPs. Hidding et al. [53] describe in detail the analysis method of the IP stacks technique, as it is used in the experiments presented in this thesis. Based on the total number of electrons and their divergence, the fraction of electrons going through the pinhole of the electron spectrometer and reaching the detector plane are estimated.
The response of IPs to electrons and the $1/cos(\theta)$ relation between the PSL value of electrons reaching the IP under normal incidence and under an incidence angle of θ is investigated by Chen et al. [52]. The effect of oblique arrival is acknowledged by considering the divergence of the electron beam and the deflection in the magnetic field of the electron spectrometer. The energy deposition in different types of IPs,

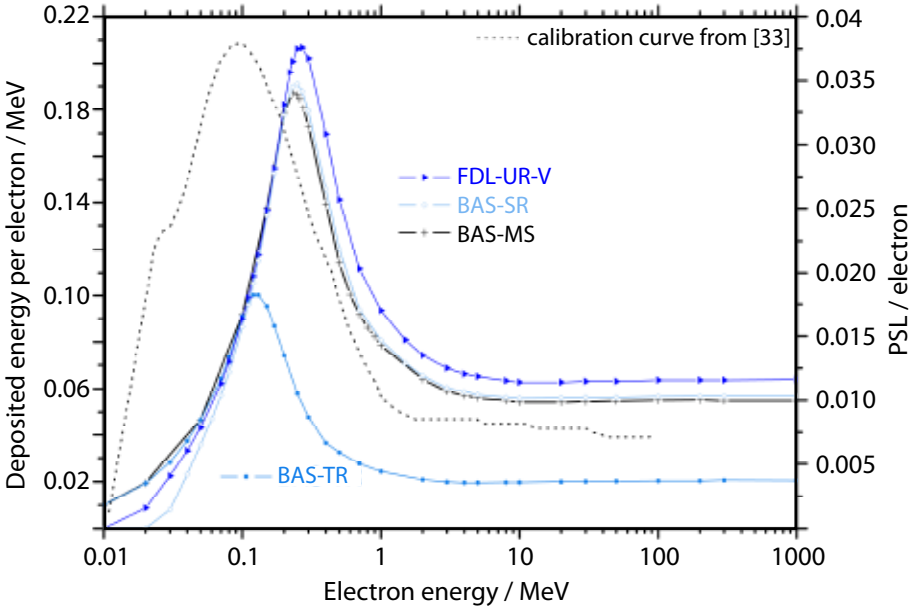

Figure 3.8: GEANT4 calculation results carried out by Hidding et al. [53] showing the deposited energy per electron for different types of IPs (solid lines and left y axis). In comparison, the PSL response per electron for the BAS-SR type IP (dotted line and right y axis) is plotted [55]

.

depending on the incident electron energy, is plotted in figure 3.8. The dotted curve is based on an experimental calibration [55], whereas the solid curves are the outcome of simulations with GEANT4 [53]. The solid, light blue curve corresponds to the IP type BAS-TR, used in this experiments and shows a nearly constant behaviour of

the deposited energy per electron, when the electron energies are higher than 1 MeV. The electrons produce a PSL signal at about 0.008 PSL/electron, looking on the experimentally measured calibration curve using BAS-SR type IPs. In comparison to BAS-SR IPs, the simulations show that BAS-TR IPs store three times less energy, consequently the PSL response is reduced to 0.003, corresponding to a deposited energy per electron of 18 keV. The calibration data in figure 3.8 is measured by reading out the IPs with a pixel size of 200 μm. The resolution of the CR 35 BIO scanner is eight times higher, therefore a factor of 64 has to be considered.

3.2.4 X-ray detection and evaluation with a Photonic Camera

Experimenting on optical laser generated ultrashort X-ray sources, based on electron acceleration from gas jets, it is mandatory to design a suitable diagnostic for hard X-rays. The theoretically expected properties of the X-ray beams imply a diagnostic for photon energies in the range of hundreds of keV with a sufficient energy resolution and a detection area large enough to capture a divergent beam.

Filter combination

In the experiment described in chapter 4.1, a Photonic Science Image Star 1001E X-ray camera is used, with an active area of 45×45 mm and an optical pixel size at the scintillator input of 44 μm. The absorption efficiency at 100 keV is 35 %, the complete quantum efficiency curve, provided by Photonic Science, is taken into account when estimating the total flux on the chip. The detector is protected by a 12 μm Al window, which is nearly invisible for high energetic X-ray radiation, but shields the array effectively from laser light. The X-ray radiation passes through a 500 μm thick glass plate and exits the vacuum chamber through a 20 μm thick polyimide (Kapton) window. The corresponding transmission curve for both, glass and kapton, can be generated with the *XCOM Calculator* of the National Institute of Standards and Technology (NIST) [56]. The product of these transmission curves and the efficiency curve of the X-ray camera can be summarised as the total response curve $R(E)$ of the detection system. The energy distribution of the scattered X-rays is experimentally measured by a set of copper filters ($f1 - f8$). Image 3.9 shows the beam profile through radially symmetrical arranged copper of different thickness (0 mm,

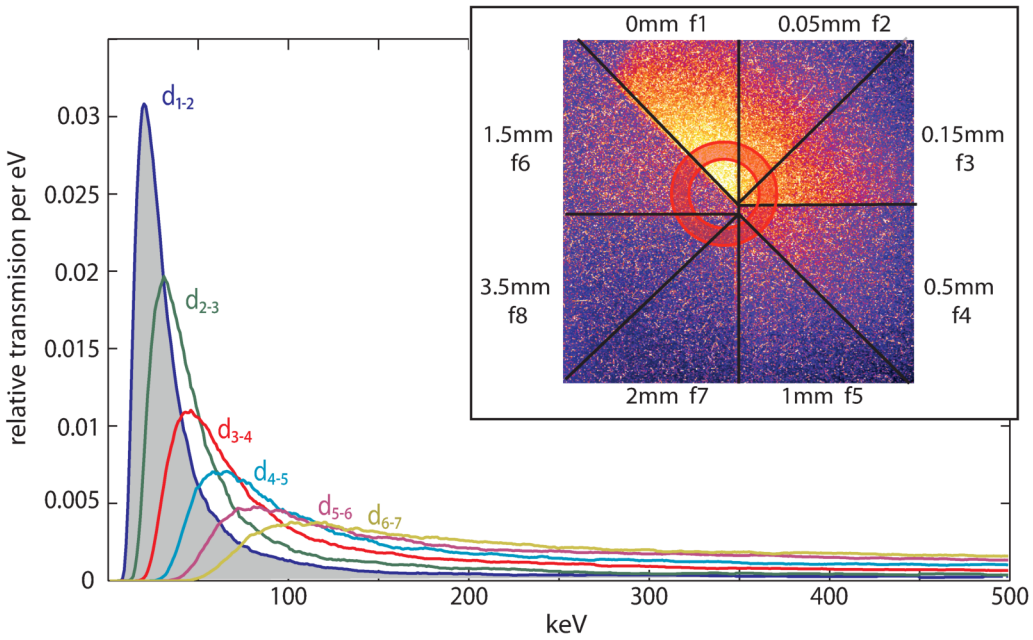

Figure 3.9: Raw image of a recorded X-ray beam going through a set of copper filters f1-f8, with the red highlighted area being analysed. The corresponding curves $d_{k/k+1}(E) = T_k(E-)T_{k+1}(E)$ are the difference of the transmission curves of two consecutive filters.

0.05 mm, 0.15 mm, 0.5 mm, 1 mm, 1.5 mm, 2 mm, 3.5 mm). The energy dependent transmission curve $T_k(E)$ for each filter is simulated by a GEANT code, which was run by Maximilian Kosel in the framework of his bachelor thesis [16]. The difference $d_{k/k+1}(E) = T_k(E-)T_{k+1}(E)$ of two transmission curves for consecutive filters is plotted in figure 3.9. The integral of $d_{k/k+1}(E)$ (e.g. $d_{1/2}$, grey area) equals to the difference in signal going through the filters. To meet the properties of a Gaussian beam profile, which can be off center to the copper arrangement, the average counts per pixel going through a filter is measured in a ring segment (highlighted in image 3.9). Knowing the response curve $R(E)$ of the detection system, which translates counts per pixel into photons, the total number of photons per 1 % bandwidth (eV) can be calculated.

3.2.5 Transmission spectrometer

For the detection of extreme ultraviolet radiation up to soft X-rays (10 eV – 10 keV), which is the typical range when scattering laser light on electron bunches accelerated

from thin solid foils, a high energy detection range Andor CCD camera is sufficient. The camera is vacuum compatible, with the advantage that no further material to hold the vacuum is in the field of view. The detectable photon energy ranges from 10 to 10.000 eV and is captured on a 27.7×27.7 mm chip with a pixel size of 13.5 μm. A transmission grating is aligned with a distance of $b = 390$ mm with respect to the CCD detector, at 0 degree to the target normal and in the direction of the driving beam (figure 3.10), to resolve the photon signal spectrally. Both, detector and grating, are covered by a lead housing with a 2 mm diameter hole at the entrance. A 200 nm aluminium filter is used to reduce any incoming optical light (e.g. laser light), while a great part of the XUV light passes through the filter. For an adequate resolution, an additional pinhole or slit (150 μm diameter/width) is added in line with the entrance of the lead housing. A side effect of the electron spectrometer, which is positioned in front of the grating setup, is the deflection of charged particles, which could cause strong background signal on the CCD. Supplementary, another strong magnet (500 mT) is located between grating and Andor camera to deflects these particles completely from the detector chip.
The grating is built of 5000 free standing gold lines per milimeter ($G = 5000[1/\text{mm}]$) on a 1 μm polyimide carrier foil and is optimised for 1st order diffraction. The dispersion at the detector plane can be measured and the wavelength λ of the radiation at a distance x from the zero point can be deduced from the interference condition

$$\lambda = \frac{1}{G} * sin(arctan(\frac{x}{b})) \approx \frac{x}{Gb}, \tag{3.4}$$

with the grating parameter G (lines per milimeter) and the distance between grating and detection plane b.

Total efficiency and analysis method

Figure 3.11 a) shows a raw X-ray spectrum of a shot on an aluminium target, which is analysed by taking the average signal of each column along the whole slit length. Hotspots are eliminated and the background signal is subtracted. The remaining counts are not directly proportional to the X-ray spectrum created during the interaction, as an energy dependent fraction of the radiation is absorbed by the Al filter and the polyimide layer of the grating. The transmission curves for these filters is provided by the *XCOM Calculator* of NIST [56]. The diffraction efficiency of the

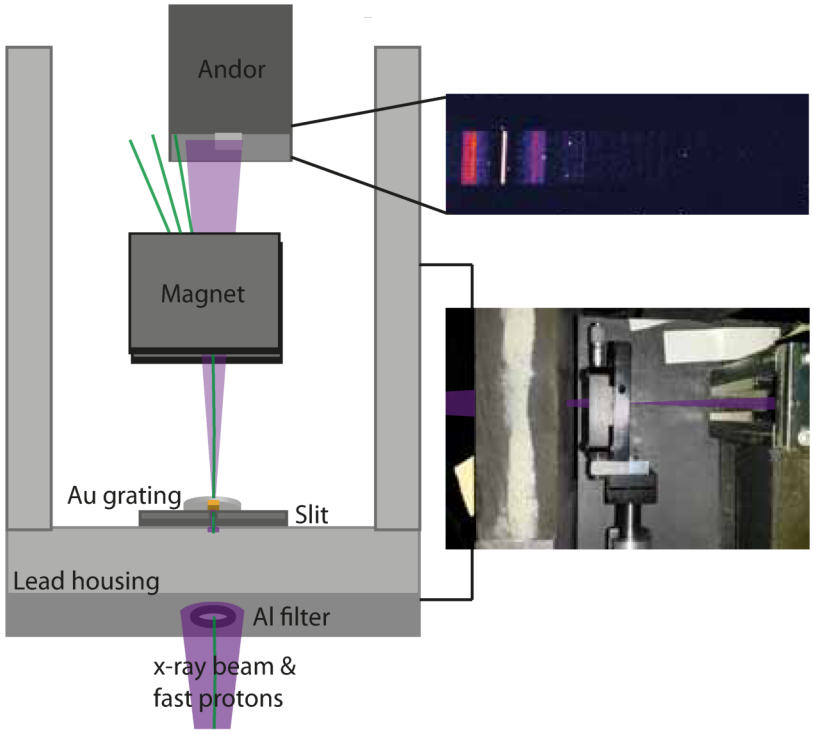

Figure 3.10: Setup of the transmission grating spectrometer. X-rays enter through a 200 nm aluminium filter and a slit. They are diffracted by a gold grating and the spectrum is detected by an Andor camera. Unwanted protons are deflected by a magnet.

grating itself can be plotted with the *Transmission Grating Efficiency Calculator*, provided by the Lawrence Berkeley National Laboratory [57]. Finally, the quantum efficiency of the CCD, provided by Andor has to be taken into account. Considering these effects, a total transmission curve of this setup can be derived and applied to the counts above background level measured on the CCD. In figure 3.11 b) the final spectrum is present. The x-axis is calculated with equation 3.4 and the X-ray counts per pixel on the y-axis include the total transmission function of the setup.
The spatial and spectral resolution of the transmission grating setup strongly depends on its geometry, more accurately the size of the elements and the relative distances between them. The source projection through the pinhole or slit with a diameter/width D is given by $\delta L = [(\Gamma + 1)/\Gamma]D$, where Γ is the magnification determined by the distance between pinhole and detector ($b = 390\,\text{mm}$), divided by the distance between source and pinhole ($a = 760\,\text{mm}$) [58]. In the setup, the pinhole size is large compared to the X-ray wavelength, that diffraction effects can be neglected

and a spatial resolution of less than 0.45 mm is achieved.
The signal on the detector has a certain spot size or line width, which is responsible for the spectral resolution of the setup. Based on the linear dispersion $D_x = d\lambda/dx = 5\,\text{Å/mm}$ calculated with equation 3.4 and assuming a point source, the minimal resolvable wavelength difference can be written as

$$\Delta\lambda = D_x * D * (1 + \Gamma). \tag{3.5}$$

For the range of interest from $10 - 100\,\text{Å}$, the spectral resolution of the setup is less than 10 %.
For a proper calibration of the spectrometer, the spectra emitted from targets of different material with well known k_α emission, for example aluminium (figure 3.11 b)) and titanium (figure 3.11 c)) are recorded.

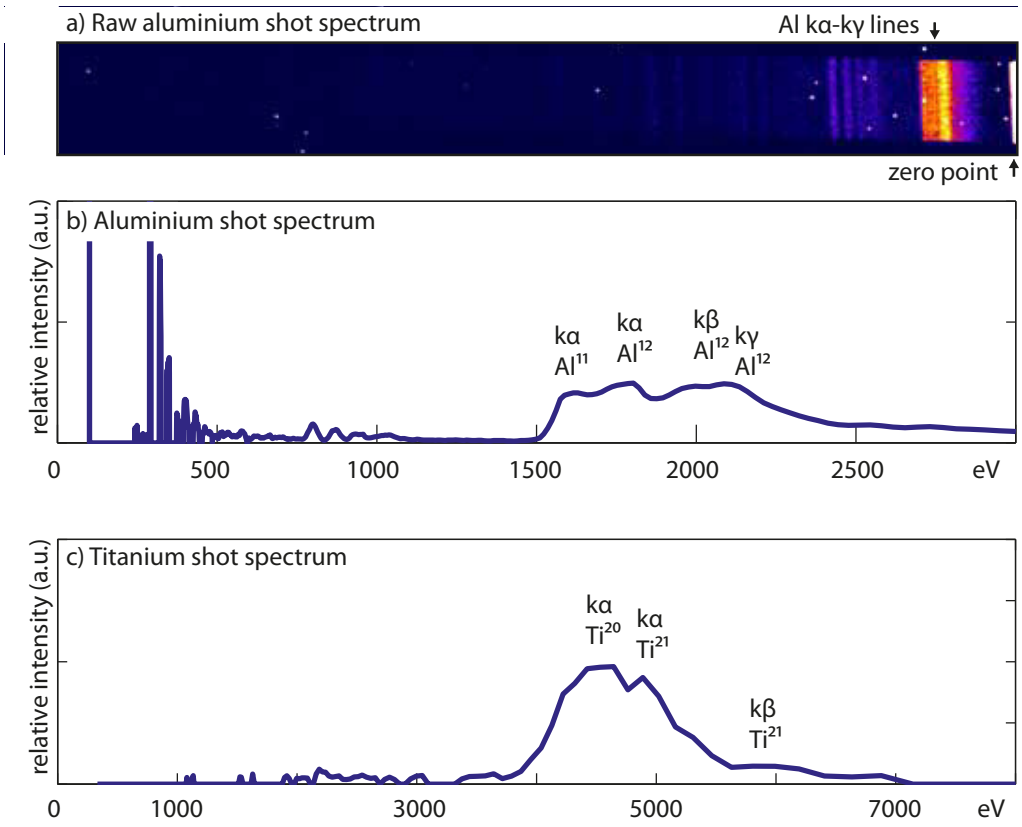

Figure 3.11: The raw image of a shot on an aluminium target is shown in a). The image is processed and the spectrum plotted in b) is obtained. In order to calibrate the spectrometer the spectrum of a shot on another target material (Titanium) is recorded c).

Laser generated, all-optical X-ray source

Ultrashort and brilliant X-ray beams are of great interest in many areas of science as they allow to resolve fast moving processes on the atomic level. A promising approach to create such radiation is based on Thomson scattering of intense laser light on relativistically moving electrons. The concept was proposed in the second half of the 20th century [59], [60] and since then intensive theoretical studies have been carried out [30], [40] and [41]. The process is build on the relativistic Doppler effect, which leads to a frequency shift of the scattered photons to $\omega_r = 4\gamma^2\omega_0/(1+a_0^2/2+\gamma^2\phi^2)$, with $\gamma = (1-\beta^2)^{-1/2}$ the Lorentz factor of the electron beam. The radiation depends on parameters, which can be freely tuned by varying the laser wavelength and the electron energy. The latter strongly depends on the applied electron acceleration method. Possible schemes are conventional high energy accelerators or the laser based acceleration from solid targets, gas jets or gas cells. Each scheme has their own advantages and has been experimentally investigated in [36], [37], [61] and [62]. In this chapter two setups are introduced, both with the aim to produce an X-ray pulse by Thomson scattering in an entirely optical manner. Firstly, the results from the scattering process of a recycled laser pulse on a 100 MeV electron bunch are presented. In this context, the electron acceleration from a gas jet is investigated. The configuration leads to the production of X-ray beams with energies around 150 keV, a divergence of less than 30 mrad. The second setup includes two independent beams, an intense ω pulse, which accelerates dense electron sheaths from a thin foil, and a counter-propagating 2ω scatter pulse. The latter is timed relative to the driver beam in such way, that it is able to scatter on the accelerated electrons. The investigations include an experimental characterisation and simulations on the electron acceleration from thin foils. Finally indications for a frequency upshift of the scatter pulse on these dense electron bunches are presented.

4.1 Thomson scattering of a recycled laser pulse on laser accelerated electrons

The two ingredients for a X-ray source based on Thomson scattering are relativistically moving electrons and a scatter laser pulse. There is a variety of experimental realisations for both of them. Quasi monoenergetic electron bunches in the range of hundreds of MeV and a high repetition rate are the results of SM-LWFA from a gas jet. The recycling of the driver laser pulse by the reflection on a plasma mirror has the great advantage of an inherent temporal and spacial overlap of the laser pulse and the relativistic electrons.

4.1.1 Setup I

The results, presented in this chapter, were obtained at the ARTURUS laser system in Düsseldorf using one of the 200 TW main laser beams for the interaction with a gas jet, and the 2ω probe beam for its diagnosis. A schematic of the experimental arrangement is shown in figure 4.1. The laser pulse is focused 600 μm above the center of the gas nozzle by an $f/12.5$ off-axis parabolic mirror to a spot size of 15 μm (FWHM).

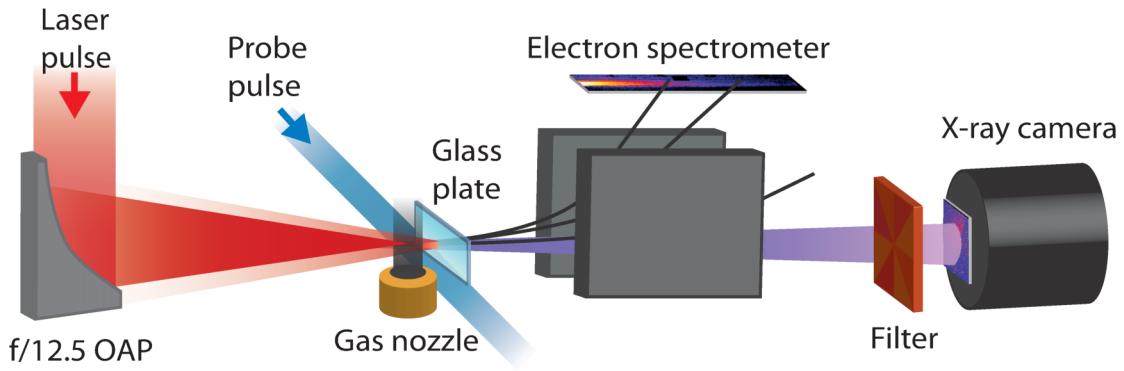

Figure 4.1: Schematic of Setup I. The laser pulse is focused by an off-axis parabolic mirror into a gas jet, reaching intensities of $10^{19}\,\mathrm{W/cm^2}$. The laser pulse is reflected back towards the accelerated electrons by a glass plate in order to generate X-rays. The electrons are detected by an electron spectrometer, and the X-rays are recorded by a Photonic X-ray camera after passing through a set of filters.

Reaching intensities of $10^{19}\,\mathrm{W/cm^2}$, the main beam accelerates electrons from the gas. A 0.5 mm thin glass plate is positioned a few hundred μm behind the nozzle,

on the laser direction. After passing the gas nozzle, the laser pulse reaches the glass plate and reflects back towards the electrons. The glass plate acts like a plasma mirror as the laser pulse has enough intensity to generate a plasma on its surface. A 2ω probe is guided perpendicular to the main beam through the interaction area to a shadowgraphy setup. The interaction plane is imaged 10 times magnified by a lens onto a camera. The electrons are detected by an electron spectrometer, resolving energies up to 150 MeV. A Photonic camera, able to detect X-ray up to hundreds of keV, in combination with different filter arrangements is used for the characterisation of the X-ray beam. The diagnostics, applied in this experiment are described in more detail in chapter 3.2. For the remainder of the thesis, this experimental arrangement is referred to as Setup I.

Gas jet characterisation

A suitable gas target for the laser based electron acceleration is the Parker Hannifin series 9 valve in combination with a supersonic nozzle. The gas used during the experiments for an optimum electron acceleration, is a mixture of 99 % Helium and 1 % Argon. The valve has a fast response time (μs) and is triggered to open just a few ms before the laser pulse arrives in order minimize the total gas load released into the vacuum chamber. The supersonic nozzle, mounted on top of the valve, is responsible for shaping the density profile. The optimum profile is a broad and flat density distribution with steep density gradient at the edges [63]. The maximum gas density is adjusted by tuning the backing pressure of the valve.
A time-resolved Mach Zehnder interferometrical measurement (details chapter 3.2.1) was performed to investigate the temporal response of the valve and the density profile along the gas jet. When the gas jet is expanding, local variations in particle density (and consequently the refractive index) result in a fringe displacement on the interferogram. The backing pressure is set to $15, 20$ and 25 bar to generate measurable fringe shift. The probe gas is 100 % Argon, instead of the gas mixture used during the shooting sessions. Argon has a higher refractive index than helium, which leads to a stronger fringe displacement at the same density.
The results reveal, that the gas density is stabilized after 6 ms, consequently the density distribution in dependence of the backing pressure at 8 ms is further investigated. Figure 4.2 a) shows the density profiles for three different backing pressures 0.6 mm

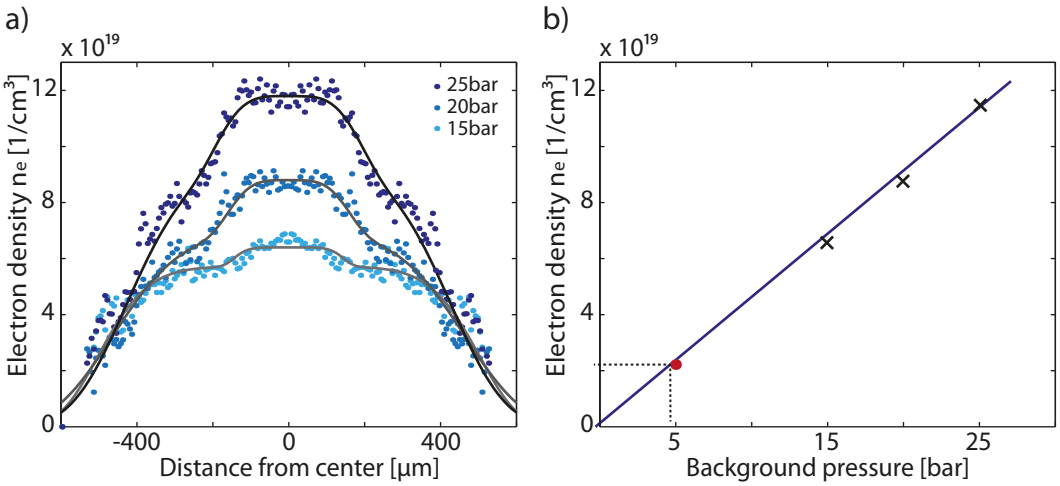

Figure 4.2: The left graph shows the interferometrically measured density profile, 0.6 mm above a supersonic gas nozzle, for three different background pressures. A linear interpolation along the data points of the maximum electron density at different background pressures is plotted in the right graph.

above the nozzle. For low backing pressure the profile becomes steeper at the edges and flatter in the center. In graph b), the maximum particle density against the backing pressure is plotted. A linear fit through the data points enables an estimation of the particle density at lower pressure values, e.g. at 5 bar the particle density equals to $1.15 \times 10^{19}\,\mathrm{cm}^{-3}$.

4.1.2 Parameter optimisation

The spectrum of Thomson backscattered photons depends on both, the electron energy distribution γ and the laser strength parameter a_0 of the recycled pulse. Therefore the study and detailed description of these parameter is essential for the interpretation of the measured X-rays.

Electron acceleration

The aim of the investigation of electron acceleration from gas jets is to create a spectrally characterised electron source for Thomson scattering. Depending on the demands of the final X-ray source, quasi-monoenergetic or broad band energy features can be of great interest. For the analysis it is important that both, the electron beam and X-rays are detected simultaneously.

Systematic modifications of different parameters, such as the nozzle diameter, the position of the focus and the plasma density were performed to find a set of parameters for a stable acceleration regime.

Figure 4.3 shows the raw data of 19 shots, recorded while continuously reducing

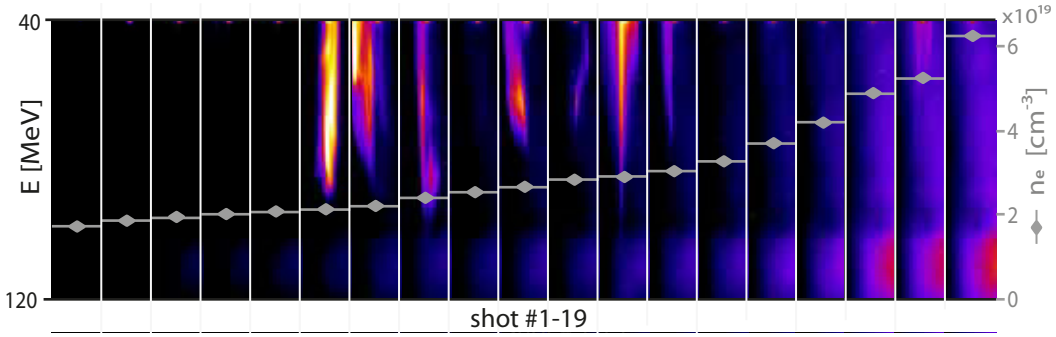

Figure 4.3: Images of the detection screen of the electron spectrometer for 19 different shots, onto a gas jet with increasing background pressure are shown. The black scale, on the left side, gives the electron energy. The gray scale, on the right side, gives the electron density of the gas jet present at each individual shot. The coloured traces are the electron signals, while the blurry purple and pink signal towards shots with high electron density are artefacts. The figure shows, that in a density band from $2-3\times10^{19}\,\mathrm{cm}^{-3}$ the electron acceleration is most efficient.

the density of the gas jet. The scale for the electron density, present at each individual shot, is on the right side of the diagram and is ranging from $1\times10^{19}\,\mathrm{cm}^{-3}$ to $6.4\times10^{19}\,\mathrm{cm}^{-3}$. The optimum density regime for the production of hot electron narrows down to a backing pressure of $5-6$ bar, which corresponds to an electron density of $2.3\times10^{19}\,\mathrm{cm}^{-3}$. At this density the condition $P/P_{crit}\gg1$ for self focusing of short laser pulses is fulfilled, which leads to an enhancement of the laser intensity. The plasma wavelength becomes longer than the laser pulse ($\lambda_P/2<c\tau<\lambda_P$), suggesting then both, SM-LWFA and LWFA acceleration can occur. The self-modulation of the laser pulse by the plasma wave can cause further shortening of the pulse. This can result in wave-breaking and the production of fast electrons in bubble like structures with non Maxwellian energy distribution. The acceleration is extremely sensitive to fluctuations of the laser and plasma parameters, for example the laser pulse duration, the plasma density profile and the spacial jitter of the laser pulse. Thus it is difficult to precisely predict the acceleration mechanism present at each individual shot causing a certain diversity of electron spectra.

Below a density of $2\times10^{19}\,\mathrm{cm}^{-3}$ there is no electron signal above 40 MeV visible,

suggesting conditions for an efficient acceleration are not met. The density profile and the exact density value at such low backing pressures originate from a linear fit and are not measured directly. A reason for the abrupt change of the electron signal can be a nonlinear behaviour of the gas density at low backing pressures. With decreasing electron density, the critical power increases. Without the effect of self focusing, the laser intensity is not sufficient to accelerate electrons to the range of hundred MeV.
For higher electron densities, the electron signal becomes less stable and the monoenergetic features disappear. The laser depletion length $L_{dep} \propto n_e^{-3/2}$ is inversely proportional to the electron density and thus becomes shorter than the plasma length leading to an inefficient acceleration.

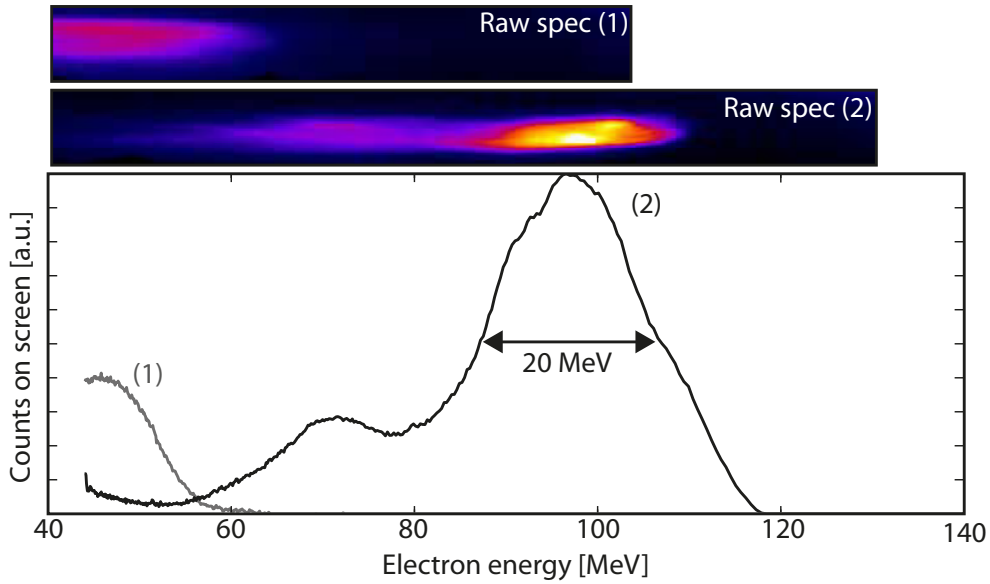

Figure 4.4: The raw electron data of two typical consecutive shots and the corresponding energy spectra are shown. The signal intensity is normalised to the peak number of counts of spectrum (2).

Various types of acceleration mechanisms, triggered at the optimum plasma density, produce different shapes of electron spectra. In Figure 4.4 two types of electron spectra are plotted, which are both normalised to the maximum signal counts of the raw data (2). Spectrum (2) shows a strong, quasi energetically narrow peak at 97 MeV with a spectral width of 20 MeV FWHM. In contrast to (2), the electron signal (1)

is decaying with increasing electron energy.
Maksimchuk et al. [64] investigated the electron acceleration in underdense plasmas using similar laser parameters and a similar gas density range. High-energy quasimonoenergetic electron beams were generated at a plasma density of $n_e = 1.5 \times 10^{19}\,\mathrm{cm}^{-3}$ to $n_e = 3 \times 10^{19}\,\mathrm{cm}^{-3}$, confirming the observations from this experiment.

Recycled Scattering Beam

For the interpretation of the generated X-ray beam in the recycling mirror setup, it is essential to estimate the intensity regime of the scattering laser pulse. The reflected beam properties were measured by tilting the glass plate 25°. Figure 4.5 a) shows the

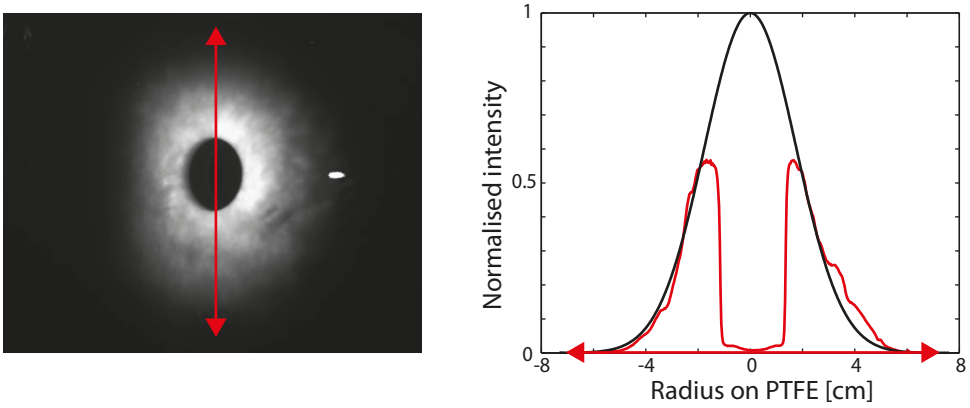

Figure 4.5: Degradiated profile of the reflected laser pulse on a PTFE screen, 32 cm behind TCC, and after the interaction with the gas jet. The red curve is a lineout taken along the arrow. The gaussian distribution (black curve) fits the data and is used to estimate the reflected total energy.

laser profile on the PTFE screen with a 2.5 cm hole in the center, in order to capture the remaining laser energy on the calorimeter behind the screen. The reconstructed Gaussian beam profile is plotted in figure 4.5 b), showing that 53 % of the total beam energy can be measured on the calorimeter. After the interaction with the gas jet and the reflection on the glass plate, about 500 mJ beam energy remains. The energy absorption during the interaction with the gas jet strongly depends on the gas jet density. For a backing pressure of 5 bar measurements account for $40 - 50\,\%$ absorption of the initial laser energy.
The electrons, accelerated during the interaction, are traveling with a velocity near to the speed of light. Considering this fact, the position where the recycled beam

scatters on the electrons is tens of nanometer away from the glass plate surface. Filamentation and refraction lead to an increased divergence of the beam and a degradation of the profile. In comparison to the undisturbed beam (shooting without gas), the divergence doubles. According to this, the beam diameter at the scattering position is about 45 μm (FWHM), resulting in a maximum amplitude of $a_0 = 0.9$.

4.1.3 X-ray beam characterisation

Along the axis of the relativistic electrons, an X-ray beam generated via Thomson scattering was detected. The X-ray radiation is produced when the recycled laser pulse scatters on the relativistically accelerated electrons. The radiation properties, such as the energy spectrum, the divergence, the pointing direction and the source size were measured and analysed by methods described in chapter 3.2.4. These properties strongly depend on the recycled laser amplitude a_0 and frequency as well as the electron beam characteristics.

Betatron radiation

Besides Thomson scattering, there is an additional X-ray source present in a laser-plasma electron accelerator. During the acceleration process the electrons undergo relativistic betatron oscillations in the strong electromagnetic field of the laser; as a result, a collimated beam of broadband radiation in the X-ray spectral range is emitted.

Figure 4.6 shows the X-ray spectrum, which was measured during an experimental campaign at the Arcturus laser facility in 2010 [65]. A $10^{19}\,\mathrm{W/cm^2}$ laser pulse was focused onto a $n_e \approx 10^{19}\,\mathrm{cm^{-3}}$ He gas nozzle and the resulting X-ray spectrum was recorded. The betatron spectrum peaks at 2 keV with a FWHM value of 3 keV.
The interaction parameters are comparable to the parameters applied during the experiment described in this chapter. Thus, it is reasonable to assume a similar emission of the X-ray beam originating from betatron oscillation. As regards detection, most of the radiation (up to 5 keV) is absorbed just by the 12 μm aluminium protection layer of the Photonic X-ray camera. Additionally the glass plate, which is inserted when creating X-rays via Thomson scattering, blocks the betatron radiation spectrum fully. This leads to the conclusion, that betatron radiation doesn't

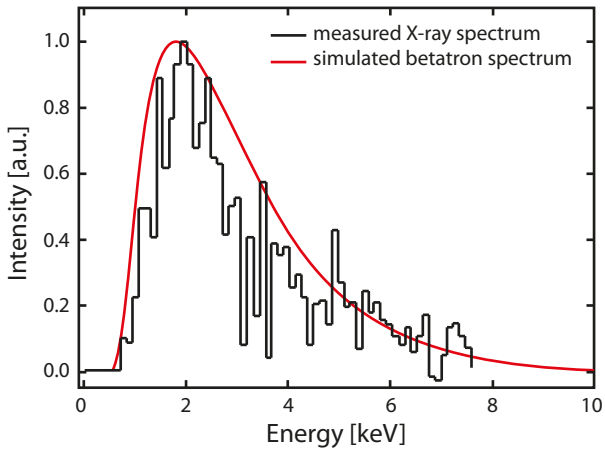

Figure 4.6: Betatron radiation spectrum (black curve) measured at the Arcturus laser facility in 2010 using similar interaction conditions as in the experiment presented in this chapter. The red curve is the simulated betatron spectrum [65].

contribute to the recorded experimental data.

Beam profile, divergence and lateral pointing

Figure 4.7 presents the detected electron raw data and the X-ray beam profile of three different single-shots. The electrons are vertically deflected by a magnet onto a screen. The lateral pointing and the energy distribution of the electron beam can therefore be detected simultaneously with the X-ray beam. The X-ray signal is partly attenuated by a T-shaped filter system before reaching the detector. This methods guarantees the accurate measurement of the beam profile, the divergence and the lateral pointing direction. At the same time, the energy distribution can be determined by analysing the transmitted signal through the filter system. This unique setup provides for the first time information about important X-ray beam characteristics in one single shot.

The electron spectrometer and the X-ray camera were aligned along the laser axis. The dashed lines in figure 4.7 a) mark the center of this axis laterally. Due to fluctuations in the density profile of the gas jet and the laser jitter, the acceleration axis of the electron beam can change on a shot to shot basis. In two different shots, shown in figure 4.7 a) and b), the direction of the accelerated electron beam diversifies from 1.9 mrad to −15 mrad. The X-ray beam follows by approximately the same amount (from 2 mrad to −18 mrad), proving that the scattering process is

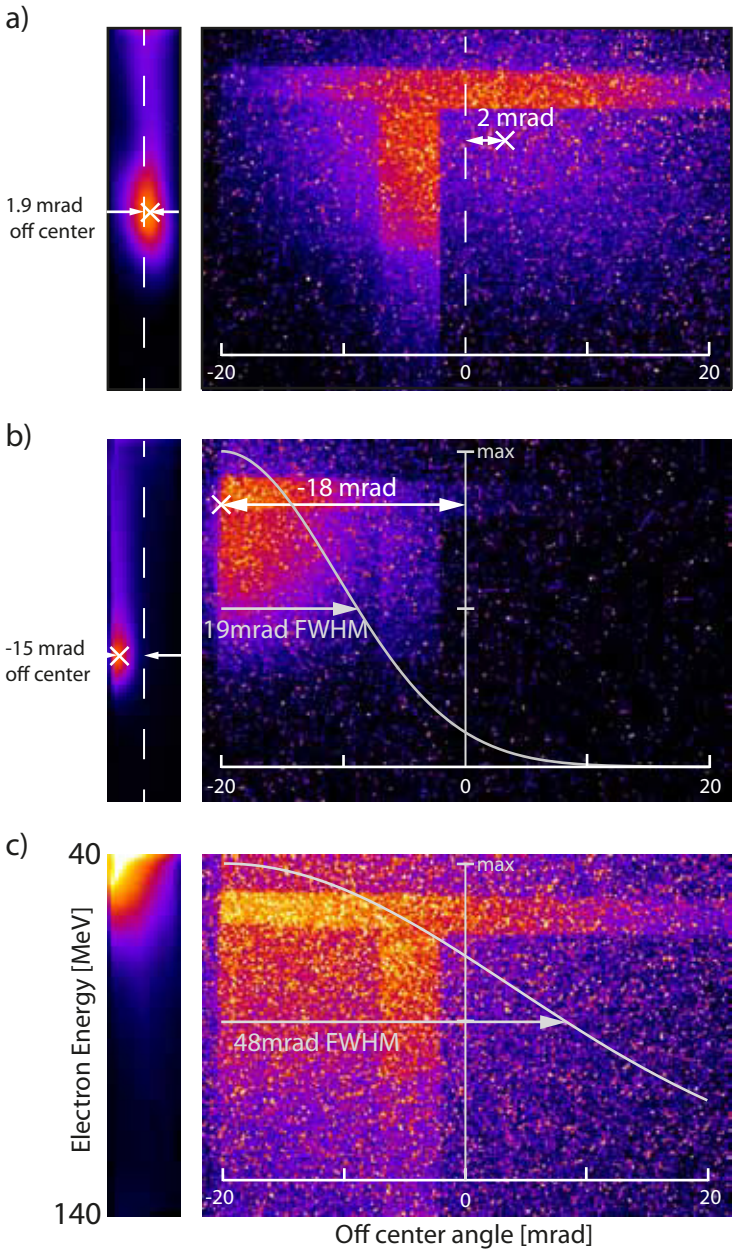

Figure 4.7: Raw electron and X-ray data of three single shots, showing the electron energy on the left side. The lateral shift of the X-ray beam is following the pointing drift of the electron beam, which is drawn in a) and b). The beam profile is plotted and its divergence is indicated for the shots b) and c) by the FWHM.

most efficient along the electron beam axis.
The X-ray beam profile has a symmetric Gaussian distribution and is plotted in light gray for the shots shown in figure 4.7 b) and c). In b) a quasi mono-energetic electron spectrum, peaking around 90 MeV, leads to an X-ray beam profile with a FWHM angle of 19 mrad. The divergence of the X-ray beam in c) on the other hand, more than doubles (48 mrad). The corresponding electron spectrum is exponentially decaying with a cut of energy of 70 MeV. This observation is supported by theory, as the divergence is a function of the energy and decreases with increasing energy. Moreover, the X-ray energy is proportional to γ^2 of the accelerated electrons.

Reconstructed X-ray spectrum based on filter edge

In this section the shape of the X-ray energy distribution is analysed. Based on the electron spectrum measured for each individual shot, the theoretical X-ray energy spectrum is calculated. Finally this spectrum is validated by experimental data, the energy dependent of the transmission through different filter configurations located in front of the detection camera.

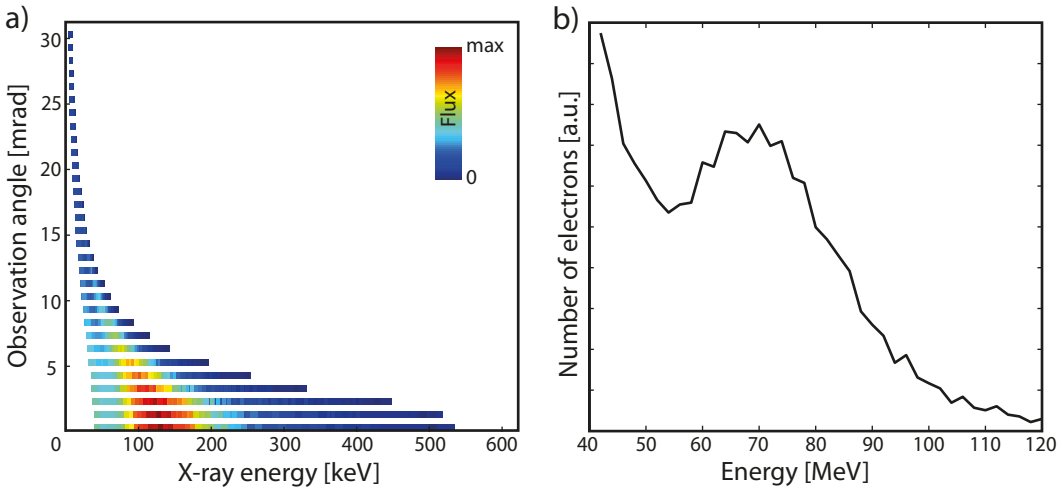

Figure 4.8: A simulated angulary resolved energy spectrum of the backscattered X-rays is plotted in a). The calculation is based on the experimentally measured electron spectrum, which is plotted in b).

Figure 4.8 a) presents a calculated angularly resolved spectrum of the backscattered photons. The x-axis of the graph shows the X-ray energy in keV, while the observation

angle in mrad is plotted along the y-axis. The colorbar represents the intensity and is normalised to the maximum intensity at 0 mrad. The simulation is based on the theoretical model for Thomson scattering for a head-on geometry described in chapter 2.7.1, using the equation 2.36 for the X-ray energy and equation 2.42 for the number of scattered photons. The input electron spectrum, plotted in figure 4.8 b), peaks at 70 MeV. The number of X-rays decreases with increasing observation angle. The slope of this decrease is mainly associated with the gaussian beam profile of the electron beam and its divergence, which is included in the code.
The general shape of the X-ray energy distribution follows the shape of the electron spectrum. The X-ray intensity resulting from the 70 MeV electron peak, at 0 mrad observation angle, is at 130 keV with a FHWM of 120 keV.

Based on the angularly resolved spectrum in figure 4.8 a), a theoretical beam profile

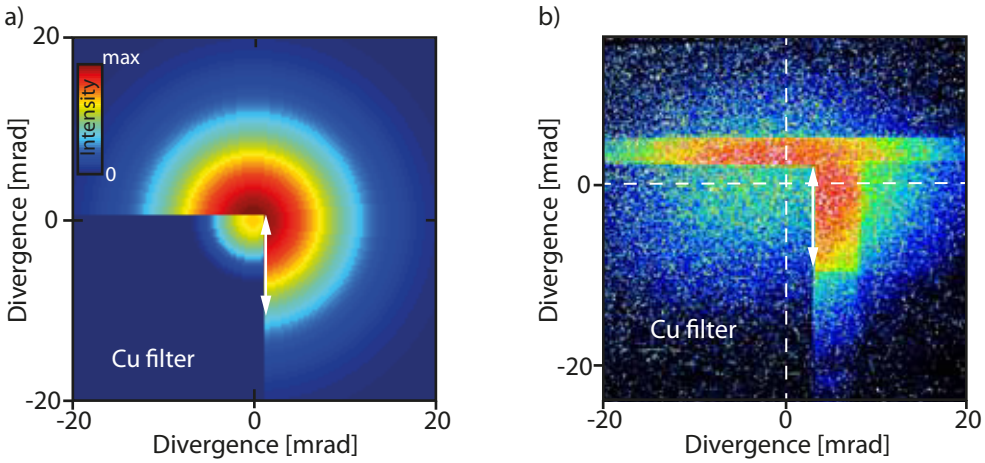

Figure 4.9: Calculated beam profile, with the attenuation of a 500 μm Cu filter in the bottom left quarter of the image a). The simulation results are compared to the experimental data plotted in b). The white arrow marks the position of a line out, which is taken and further analysed.

can be reconstructed, which is shown in figure 4.9 a). During the experiment, a 500 μm thick copper filter was used to attenuate the X-ray signal of approximately one quarter of the beam. In the theoretical beam profile, the energy spectrum of this part of the beam (bottom, left quarter) is multiplied with the transmission curve of the filter, in order to model the experimental configuration. Figure 4.9 b) presents the corresponding X-ray raw data, including the 500 μm thick copper filter. Along the white double arrow (in both plots) line-outs were taken, which are plotted in

figure 4.10 a), normalised to the peak intensity without any attenuation.

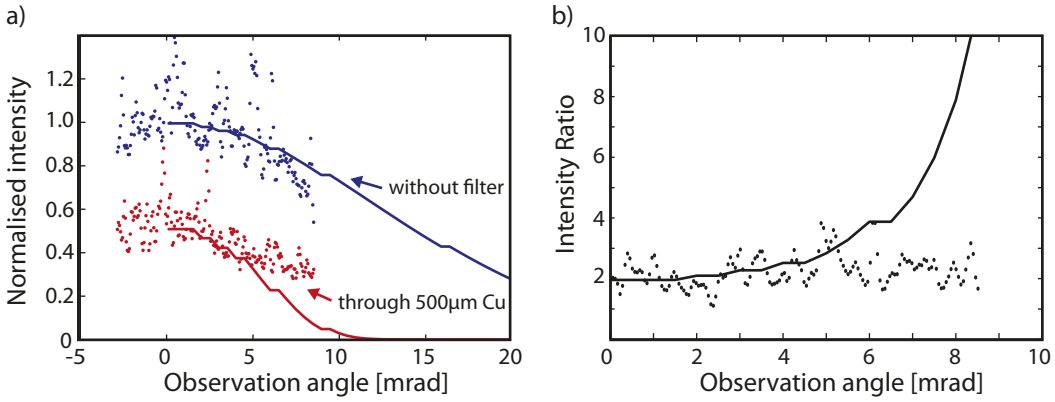

Figure 4.10: The graph in a) shows the experimental (dots) and calculated (lines) lineouts along the detected X-ray beam (white arrow in fig. 4.9). The black line/dots are showing the profile without attenuation and the gray line/dots profile is taken with a 500 μm Cu filter. The ratio of these two profiles (with and without filter) is plotted in b).

The calculated curves, with and without filter, fit the experimental data points well between $0 - 5$ mrad from the observation axis. Further away from the axis the experimentally measured X-ray beam, which is not attenuated by a filter, is less intense than expected from the calculations. However, the filtered signal is stronger than predicted. In figure 4.10 b), this trend becomes even more clear by plotting the ratio of the X-rays reaching the detector directly and through a filter. For the central, high energetic part of the X-ray beam, the curve overlaps with the experimental data and for angles > 5 mrad the calculated ratio increases rapidly.
The calculation relies on two approximations; The first one is caused by the low energy detection limit of the electron spectrometer. The minimum energy of the input electron spectrum is 40 MeV, while the undetected part of the spectrum from $0 - 40$ MeV can contribute strongly to the final X-ray spectrum and beam profile. The second approximation is, that the angle between the electrons and the scattering laser is considered as 0° (head-on geometry). This leads to a correct estimation of the X-ray spectrum near the propagation axis. However, further away from the axis the divergence of the electron beam and of the back-reflected laser pulse leads to a larger interaction angle. Consequently, the back scattered radiation for observation angles > 5 mrad is less intense in the experimental results.

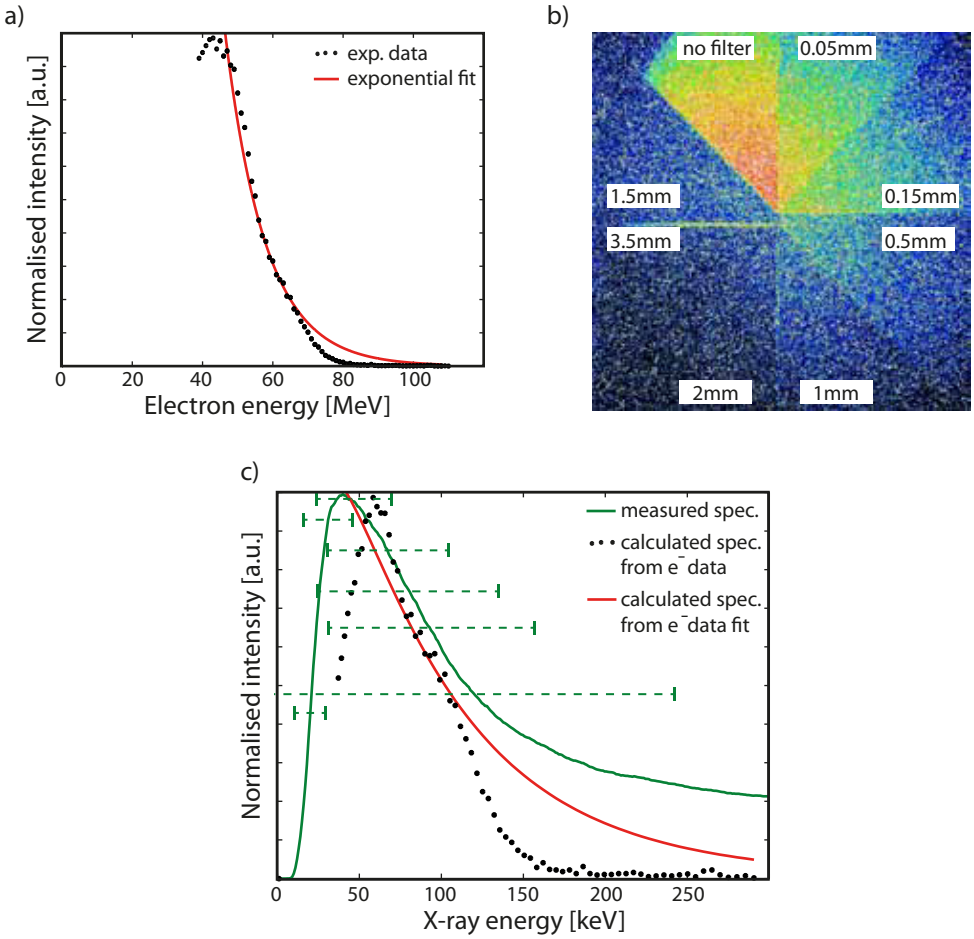

Figure 4.11: Graph a) shows an experimentally measured electron spectrum of a single shot and its exponential fit. In b) the associated X-ray raw data is plotted, showing the different filter areas. c) Comparison of the experimentally measured and the theoretically predicted X-ray spectrum. The latter is calculated from the electron spectrum in a).

Reconstructed X-ray spectra from multi Cu-filter setup

The second filter configuration applied in the experiment consists of seven, radial symmetrically arranged Cu filter ($0.05 - 3.5\,\mathrm{mm}$ thick). The details of the setup and the analysis method are described in section 3.2.4. Figure 4.11 a) shows the experimental electron spectrum and an exponentially decaying fit. The corresponding X-ray beam, plotted in b) is centered (with a certainty of 5 mrad) behind the filter system. As expected for an exponentially decaying electron beam in this energy range, the X-ray beam divergence is rather large, about 50 mrad. In figure 4.11 c), the X-ray energy spectrum from the X-ray signal on the camera is compared to

the calculated spectrum, which is based on the measured electron spectrum. The green curve, peaking at 48 keV is reconstructed from the difference in signal going through neighbouring filters. This signal equals to the integral over the subtracted filter transmission curves $d_{k/k+1}(E)$ (section 3.2.4) of the associated filter pair. The horizontal error bars are the FWHM of $d_{k/k+1}(E)$ for each filter pair and increase rapidly for higher energies. The measured single-shot result (green curve) is shifted 10 keV to the theoretically predicted spectrum built on the measured electron spectrum (black dots), but for energies > 40 keV it is still within the error bars. The method relies on the assumption that the energy distribution is not changing across the filters and that the observation angle is 0 degree.
Now two facts can be taken into account: The X-ray beam can be located up to 5 mrad off center and the measured signal is averaged over an area up to 5 mrad away from the center. Thus it is reasonable to compare the results to the predicted X-ray spectrum for an observation angle between $0 - 10$ mrad. It is shifted towards lower energies and therefore fits the measured results within the error bars over the whole spectral range.

Number of photons and source size

An important quantity in the characterisation of an X-ray source is the number of photons which can be produced in a certain amount of time, namely the X-ray flux.
Figure 4.12 shows the number of photons per keV, considering an averaged measured number of counts at the center of the X-ray beam. The spectrum originates from the angularly resolved energy spectrum in figure 4.8 at 0 mrad observation angle (beam center). Its integral equals the measured number of counts multiplied with the energy dependent response curve of the detection system

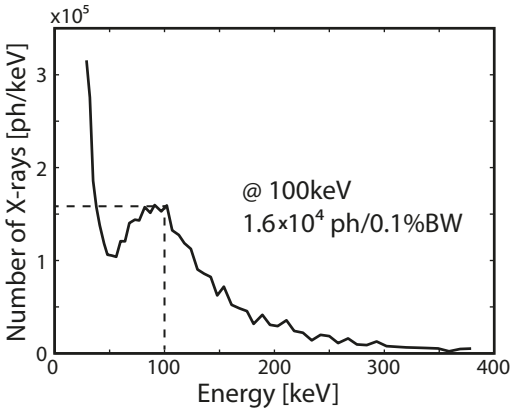

Figure 4.12: Number of X-ray photons per keV depending on the energy at the beam center.

(section 3.2.4). The multiplication of the integral of the curve with the solid angle of the X-ray beam results into a total photon number of 4.2×10^6. The peak of the energy spectrum is at about 100 keV. At this energy (dashed line) the number of photons per 0.1 % bandwidth is 1.6×10^4 ph/0.1% BW.
Another parameter of an X-ray source is the source size. The knife-edge technique is often used in order to determine the source dimensions. This method is a geometrical approach, where the intensity profile of the shadow of a knife-edge and the distances of the detector and of the source to the object are considered. The images recorded during the experiment in the context of this thesis show only objects (e.g. filters), which are rather close to the detector plane. Considering this geometric setup and the fact, that the X-ray camera resolution of 44 μm per pixel is rather low, the calculated source size, based on the intensity profile of a filter edge is in the range of several mm. A typical Thomson backscattering source size should be in the range of tens of μm [37] [66]. One factor contributing to this discrepancy is the method itself. A sharper object can be used, which should be positioned closer to the source than to the detector in order to improve the accuracy of the measurement. However, the large value obtained from the filter edge indicates, that other sources in the same wavelength range may be present. The accelerated electrons are stopped by various materials (magnet, chamber walls) and thus secondary radiation in the X-ray regime is produced e.g. by Bremsstrahlung. This radiation can contribute to a rather diffuse background signal and has an impact on the shadow profile of an object on the X-ray camera. In future, a pinhole geometry can be implemented to overcome this issue and improve the imaging quality.

4.2 X-ray generation in counterpropagating double beam configuration

An ultrashort X-ray source based on the interaction of a high intense laser pulse with a ultra thin target depends strongly on the ability to create a dense population of fast electrons, which forms a mirror like structure. This effect was investigated in theoretical work by applying laser intensities high enough to completely separate all electrons from the ions, using a few nm thick targets [30]. The counter-propagating laser pulse reaches the electron bunch within hundreds of fs afterward and experiences a frequency upshift, which depends on the laser pulse frequency and the electron γ-factor distribution.

4.2.1 Setup II

The experimental setup shown in figure 4.13 is designed to use the unique advantages of the Arcturus Laser System at HHU Düsseldorf. Providing two independent beams, each with a separate compressor and plasma mirror, this configuration is suitable for shooting both high power beams counter propagating. The driving pulse is focused by an $f/2$ parabola onto the front side of the target to a reproducible focal spot of 3μm FWHM. The pulse is compressed to a pulse duration of 27 fs and has an energy on target of 1J at the central wavelength of $\lambda = 800\,\text{nm}$, reaching peak intensities of 10^{20} W/cm^2. In the following, this beam is referred to as "driver". To obtain the contrast level required for targets in the nanometer thickness range, additional pulse cleaning is reached by using a plasma mirror. The collimated scattering pulse, is converted to 2ω by a 75mm diameter KDP crystal. Afterward, a 4 mm thick blue glass filter and two mirrors coated for 400 nm vanish the remaining infrared fraction in the pulse and an $f/6.6$ parabola focuses the beam onto the rear side of the thin foil. The energy, reaching the target, is measured to be 25 mJ in a focal spot of 50μm FWHM. By calculations the pulse duration can be estimated to 100 fs as the initial 27 fs infrared pulse travels through 4.5 mm glass and is widened due to dispersion. Both beams are operated with the plasma mirror included, offering the advantage of protecting the beams to couple one on the amplifier line of the other. The energy distribution of the electrons accelerated by the driving beam is measured with a 150 mT magnet deflecting the electrons onto a detector. The radiation emitted from

the foil and the radiation created in the scattering process is diagnosed at 0 degree to the target normal in the direction of the driving beam. For this reason the parabola focusing the scattering beam has a 1 cm hole in its center and the spectrometer to measure the radiation energy is set up behind this parabola. A 150μm slit defines the entrance of the spectrometer, which is based on a transmission grating with 5000 lines/mm supported by a 1μm polymer layer. In addition the entrance is light tide shielded by a 200 nm aluminum filter to protect the detector, an Andor camera which is positioned 40 cm behind the grating. More details of the spectrometer are given in Chapter 2.

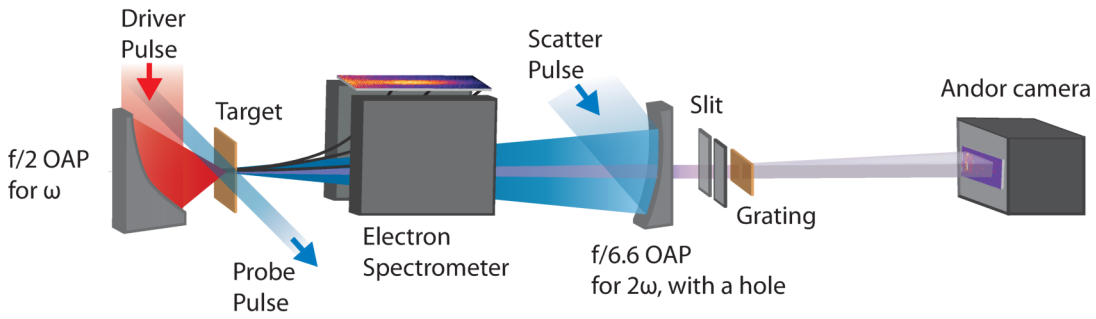

Figure 4.13: Illustration of Setup II. The ω driver pulse is focused by an $f/2$ off-axis parabola onto the front side of the target, while the 2ω scatter pulse is focused onto the rear side by an $f/6.6$ off-axis parabola with a hole in its center. The electrons are detected by an electron spectrometer. A transmission grating in combination with an Andor camera is installed as an X-ray diagnostic.

Spatial and temporal overlap of two beams

One of the most important requirements for a successful backscattering process is a precise temporal and spatial overlap of the driving and the scattering pulse. The spatial overlap is obtained by defining the TCC with the tip of a 10μm thick wire, which is imaged in both high magnification focal spot diagnostics. The pointing stability is measured to be less than 10μm for the driver and less than 20μm for the scattering beam. During shooting sessions over several hours, the spatial overlap is double checked every hour to ensure, that the beams have not moved or misaligned. To control the time between the two beams, so called delay stages are build into the beam line. The beam path is folded in a setup including two motorised mirrors to

either increase or decrease the path the light has to travel before reaching the TCC. A timing precision in the nanosecond range is ensured by reflecting both beams onto a photo diode by the edge of a prism set up at TCC.
The formation of a dense electron sheet and its widening in thickness and decreasing in density occurs within just a few hundreds of femtoseconds. Its life time depends of the target areal density and the laser pulse amplitude a_0 [67]. Thus, for an effective scattering process, the timing between the beams in the range of femtoseconds becomes crucial.
In the alignment process before each shooting session the photo diode is replaced by a camera, which monitors the overlap profile of the two beams and the beam path length of the scattering beam is adjusted. When both pulses are temporally synchronised, the condition for constructive interference is fulfilled and a fringe pattern becomes visible on the camera. Theoretically, this method should ensure a timing precision in the range of the laser pulse duration (tens of fs). However, in the experiment the fringe pattern appears on the camera for a longer time period. The reason for this is, that both beams are guided through a lens system, in which outer rays of the spatial beam profile travel a longer distance than central rays. Thus, for some part of the beam profile, the condition for interference is given for about 300 fs.

Flat foil solid targets; Preparation and Alignment

Experimental investigations of ultrathin foils is a widely studied topic; it has been demonstrated that in reduced target size, new acceleration mechanisms can be generated for an improved particle (e^- and ions) beam quality [68]. For the formation of dense electron bunches for instance, a combination of a high contrast laser pulse on target foils in the range of tens of nanometer is used [30].
Targets used for the investigations described in this chapter are $50 - 100$ nm thick diamond like carbon (DLC) foils and 27 nm parylene ($H_8C_6F_2$) foils floated onto a $6x5.5$cm brass frame with about 400 holes of 1mm diameter. DLC foils are an amorphous type of carbon and they are assigned to different kinds of characteristics usually related to diamond, for example chemical resistance and mechanical strength [69]. The second type of targets, used during the experiment is 27nm parylene ($H_8C_6F_2$). It has the advantage of mechanical stability as well as homogenous thickness over the whole layer and small surface roughness [70]. The target preparation process is

similar to the one for DLC foils where the target layer is attached to the brass frame via adhesion [69].
The delicate nature of ultra thin targets requires careful handling during the whole alignment process. The vacuum chamber needs to be pumped down slowly and the irradiation with focused laser pulses, even in a low energy alignment mode, should be avoided. Target alignment is operated before each shot by imaging the TCC position in the focal diagnostic system. The target material is transparent and small structures, such as dust particle can be imaged in order to drive the foil into the correct focal plane. Likewise, this method allows to review the target quality as double layers or damages of the target surface can be identified.

4.2.2 Characterisation of the acceleration of thin foils

An ultrashort X-ray source based on the interaction of a high intense laser pulse with an ultra thin target depends strongly on the ability to create a dense population of electrons which form a mirror like structure. The dynamics of the thin foils, in particular the plasma expansion on the rear side of the target can be observed in the shadowgraphy image of the interaction. Figure 4.14 a) depicts the raw shadowgraphy image of an expanding 100 nm parylene foil, 200 ps after the laser pulse left the target. The target is mounted on a grid, which is visible in the image in form of a shadow, restraining the view on the expansion at the early stage of the interaction. However, at later times (delay$>$ 50 ps) the plasma expansion at the front and the rear side of the target along the laser axis exceeds the shadow of the target mount and thus becomes visible again. The graph in b) shows a comparison of the expansion velocities of a thick (5 μm titanium) and a thin (100 nm DLC) foil. Up to 300 ps the expansion velocity at both sides is higher in the thin target case. This behaviour changes at later times, when the expansion material is depleted. Another observation is, that the plasma at the rear side of the thin target expands faster than the front side, which is contrary to the expansion dynamics of the thick target. The expansion of the thick target can be understood with the collisionless absorption mechanisms described in section 2.5.1. The laser pulse interacts mainly with the front side of the overdense target and the resulting electron population travels through the remainder of the target before escaping into vacuum. This process causes a strong plasma expansion at the front side of the target, which becomes visible in the shadowgraphy image. The

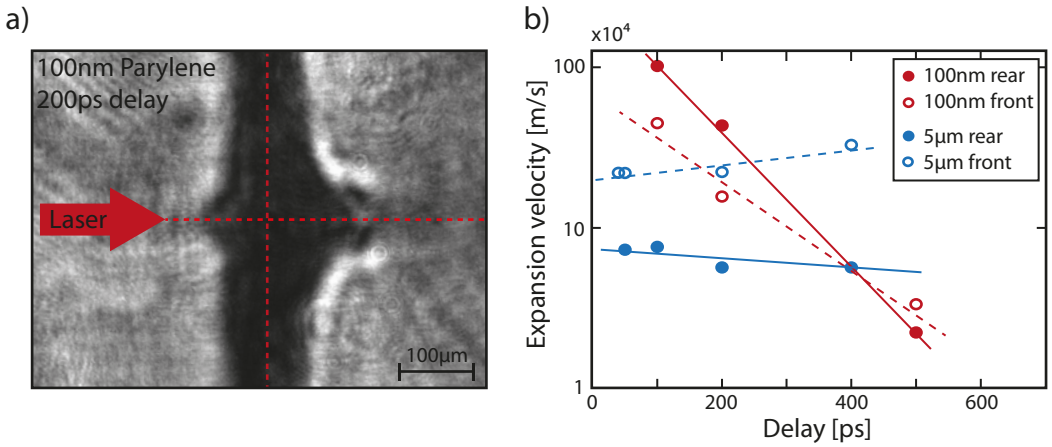

Figure 4.14: a) Shadowgraphy image of the plasma expansion of a 100 nm thin foil, 200 ps after the interaction. b) Time dependent expansion velocity of the front and rear side of a thin target (red) and a thick target (blue). The results are obtained by focusing a high contrast (plasma mirror) laser pulse with an $f/2$ parabola onto the target, reaching an intensity of 10^{20} W/cm^2.

interaction with a thin target is different. A laser pulse can propagate into a solid target up to the characteristic skin depth $l_s = c/\omega_p$, which depends on the plasma frequency and therefore the electron density n_e. Typical values for the skin depth are in the nm range. If the foil thickness is in the same range, the target becomes partially transparent for the laser pulse. Thus, the laser pulse has a direct impact onto the dynamics of the electron acceleration, which resembles a rather collective motion [71].

An additional effect is the recirculation of the electrons in thin targets, which applies when the target thickness is smaller than half a laser period $d < c\tau_L/2$ [72]. The accelerated electrons can be reflected several time at the back and front of the target by the Debye sheath. The electrons can transit the target twice, if the foil is thin enough. In this case, the total electron density is a superposition of the recirculated electrons and the electrons, which are accelerated by the laser pulse. The effective hot electron density increases compared to the thick target case and the plasma expansion becomes stronger [72].

The observations confirm that processes in connection with the interaction of a high intense laser pulse with a thick or thin target differ fundamentally. In the context of the development of a laser based X-ray source, a collectively forward moving, dense electron sheath is favoured. The temporal dynamics of the hot electron population

created from thin targets meet better these conditions.

Simulation on electron bunch formation from thin foils

The early stage of the acceleration process, when the laser peak energy enters the target, is crucial in the development of dense electron sheaths from thin foils. As mentioned before, the experimental observation of this stage is limited. However, particle in cell (PIC) simulations exhibit the electron density distribution up to several hundreds of femtoseconds. Moreover, additional quantities such as the electron energy and the directional impulse of each particle are obtained.

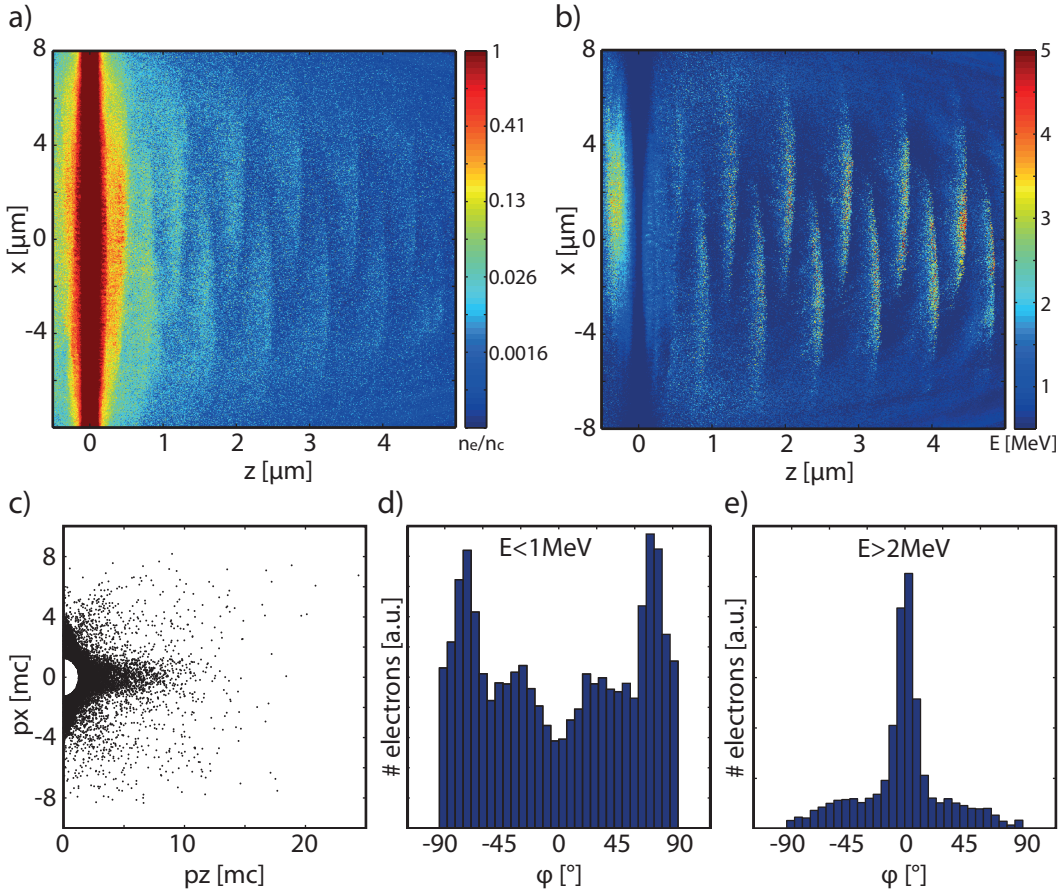

Figure 4.15: 2D-PIC simulation results from the interaction of a high intense laser pulse ($10^{20}\,\mathrm{W/cm^2}$, 30 fs)with a 30 nm thin carbon layer. a) shows the electron density distribution at $\omega t = 10$, in units of the critical density for 2ω. In b) the corresponding electron energy distribution and in c) the electron phase diagram is plotted. The graphs d) and e) display the angular distribution of all electrons with energies $E < 1\,\mathrm{MeV}$ and $E > 2\,\mathrm{MeV}$.

To demonstrate the acceleration from a thin foil, 2D PIC simulations have been preformed with the EPOCH 3D code for a linearly polarised, gaussian laser pulse, propagating along the z axis, with a peak intensity of $10^{20}\,\mathrm{W/cm^2}$ and a pulse duration of 30 fs. The target is a 30 nm thick carbon layer with a solid state density $n_0 = 150 n_{cr,\omega}$. The simulation box is $15\mu\mathrm{m} \times 20\mu\mathrm{m}$ in transverse and longitudinal direction and has a spatial resolution of 5 nm. Figure 4.15 a) presents the electron density distribution in units of the critical density for a 2ω laser pulse $n_{cr,2\omega} = 7 \cdot 10^{21}\mathrm{cm}^{-1}$ at $\omega t = 10$ relative to the pulse maximum. In b) the corresponding electron energy distribution is plotted. Both graphs show periodically generated, dense electron layers with energies of $2-3\,\mathrm{MeV}$ traveling into vacuum at the back side of the target. The dominant absorption mechanism in this interaction is $v \times B$ heating. During this process the laser energy is transferred to the electrons at every half cycle of the laser field. The result is, that thereby accelerated electrons escape into vacuum in form of multiple thin plasma layers at a frequency 2ω, with densities in the range of the critical density for ω laser light. Eventually the bunches are traveling with a velocity near to the speed of light, along the k-vector of the radiation free in space.
The qualitative observation that the high energetic dense electron sheath is moving mainly in the forward direction is confirmed quantitatively, when considering the impulse of the particles, which is plotted in c). A fraction of the total number of electrons propagates almost radial from the focal spot, while another fraction is directed strongly along the z axis. In order to analyse the dependency of the electron propagation direction on the energy, histograms of the angular distribution of all electrons with energies $E < 1\,\mathrm{MeV}$ and $E > 2\,\mathrm{MeV}$ are plotted respectively in d) and e). The laser front, reaching the target is strongly bend due to the focusing on the $f/2$ parabola; a part of the profile has components, which are not normal to the target surface. The components, which are parallel to the foil are responsible for the generation of rather low energetic surface electrons, which are accelerated predominantly into the x direction. Electrons with energies $E > 2\,\mathrm{MeV}$ move mainly in the forward direction, as the maximum intensity of the laser pulse is normal to the target, which leads to an efficient $\mathbf{J} \times \mathbf{B}$ heating. The curvature of the wave front introduces a small angular distribution, accompanied with the velocity dispersion for different energies, the dense bunch structure survives on a micrometer scale distance.

4.2.3 Indications for frequency upshift from relativistic electron bunch

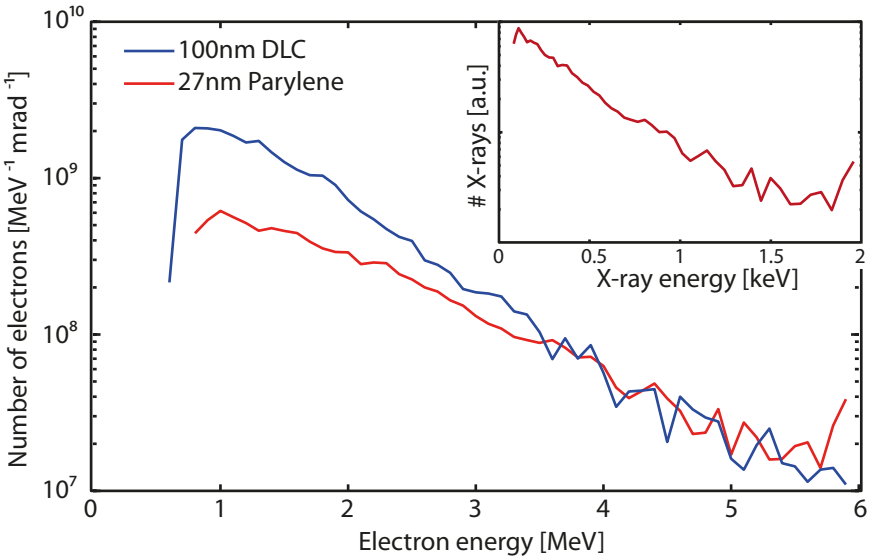

Figure 4.16: Electron spectra from the interaction with a 100 nm DLC foil and a 27 nm parylene foil. The small window shows the calculated X-ray spectrum based on the scattering process of a 2ω laser pulse on the accelerated electrons from a 27 nm parylene foil.

The X-ray energy range for the scattered 2ω laser pulse on the relativistic electron bunch can be predicted with the formula for the relativistic Doppler shift, which was introduced in section 2.5. Essential for this prediction is the electron energy spectrum, which was measured for the interaction with a 100 nm DLC foil and a 27 nm parylene foil. Both spectra are plotted in figure 4.16 and show a typical exponential decay between $1-6$ MeV with a maximum number of electrons around $10^9\,\mathrm{MeV}^{-1}\mathrm{mrad}^{-1}$. The small plot in figure 4.16 depicts the calculated X-ray spectrum based on the measured electron distribution of the 27 nm parylene target. Note that the simulation results in section 4.2.2 indicate, that electrons which are accelerated mainly in forward direction have energies $E > 3$ MeV. Thus, the X-ray energy range between $0.6-1$ keV has to be carefully investigated.

Figure 4.17 exhibits a typical recorded raw X-ray spectrum. In this representation, the zero order and the high energetic part ($E > 2000$ keV) are saturated in order to enhance the visual dynamic range of the relevant part of the spectrum. The freckled background originates from charged particles, such as protons, ions or electrons,

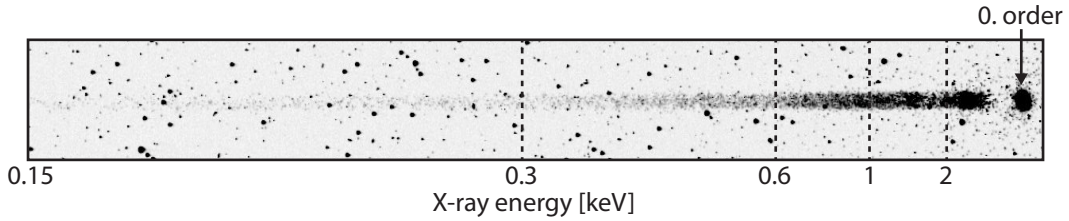

Figure 4.17: Image of the raw X-ray data obtained from a 27 nm target shot, using driver and scatter beam simultaneously.

which are not deflected sufficiently. A detailed analysis of the raw data reveals, that the average counts per pixel in the freckles is significantly higher than the zero order signal. Therefore, it is possible to distinguish between real X-ray signal and the signal of other radiation sources.

The detected signal is normalised to the zero order signal of each individual shot, in order to be comparable to each other. The zero order contains the whole spectrum, thus an enhancement of the normalised signal implies that the X-ray signal of the specific energy band is increased. In figure 4.18, this normalised signal is plotted for three different energy bands, 1190±30 eV, 910±30 eV and 690±30 eV. Experimentally challenging, but crucial for the scattering process, is the relative timing between the driver pulse and the scattering pulse, which covers a range from −2 to 1 ps, where negative sign means that the driver beam comes first. The expected optimal time range for a successful scattering process is a few hundreds of fs after the interaction of the driver pulse with the foil. Most shots, with negative delay (driver beam before scattering beam), which is an inevitable condition for Thomson scattering, have a similar signal level compared to shots with positive timing or shots with the driver beam only. However, there are a few shots in the relevant delay regime, between 0 to −300 fs, which show a stronger X-ray yield. The low rate of shots with an enhanced signal is not surprising, as the ideal conditions for Thomson scattering to occur undergo experimentally strong fluctuations. The error bars result from a statistic which shows, that the number of counts for each energy interval can be measured with a certainty of ±2 counts. Consequently the error bars become larger, when the absolute signal level is low, which is the case for the shots with enhanced signal. Considering the lower limit of the error bars, the yield in two shots is still above average for the energy bands 1190 ± 30 eV and 690 ± 30 eV. These results are a clear indication for a Doppler frequency upshift of the scatter beam from the

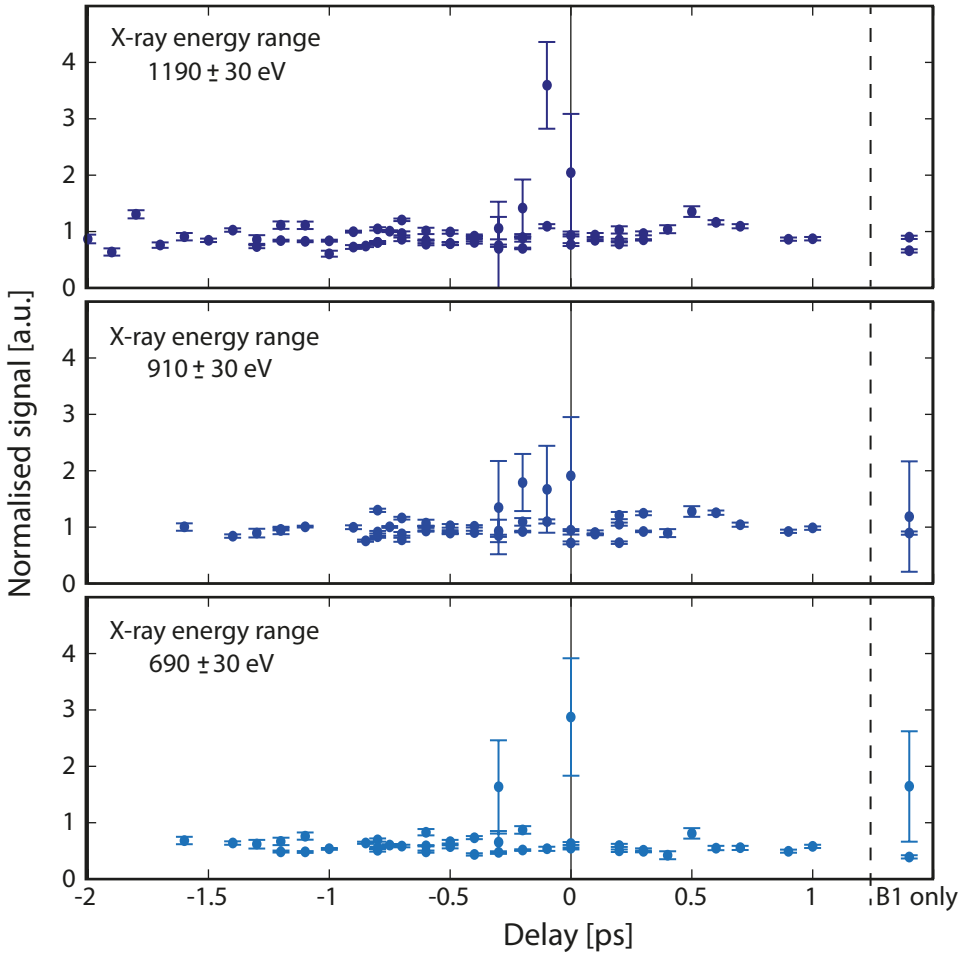

Figure 4.18: Normalised signal at three different X-ray energies from shots on 27 nm targets. The relative delay between scatter and driver pulse spans from −2 to 1 ps. The enhanced signal between −0.3 ps and 0 ps is an indication for a frequency upshift of the blue scatter beam on the previously accelerated electron sheath.

laser-driven electron bunch.

4.3 Discussion

In the following, the experimental results of both, Thomson scattering of a recycled laser pulse on laser accelerated electrons from a gas jet (setup I) and Doppler upshift in counterpropagating double beam configuration using solid targets (setup II), are discussed in the context of other experimental and theoretical investigations in this field. Difficulties in the experimental execution and suggestion for optimisation, as well as further prospects are reviewed.

Table 4.1 gives examples of experimental work carried out on the topic of Thomson scattering on electron bunches, similar to setup I. The characteristic parameters of the interaction partners, in particular the electron distribution and the scattering beam intensity are listed. The resulting X-ray beam properties, such as the divergence, the total number of photons, the peak number of photons at a specific energy and the source size are selected for a comparison of the experimental results presented in section 4.1 to three different publications. All quantities are in the same range of magnitude, showing that the results obtained in connection with this thesis fit well into the current status of all optical X-ray sources. However, some differences can be pointed out.
One mayor challenge is the reproducible generation of a stable electron beam, which is a highly investigated research topic on its own. Khrennikov et al. [73] report on a tunable, quasi-monochromatic X-ray source, which is an inherent result when using a stable electron source producing monoenergetic bunches. In their case, a shock front injector scheme was used, which was developed in a separate experimental investigation [74]. To implement this scheme, a razor blade is placed in the supersonic flow of the gas nozzle. The obstacle causes a sharp downwards density jump, which is used for the injection and trapping of electrons. The development and fine tuning of such an electron source is intense and time consuming and thus, beyond the time limit of the experimental campaign, which is presented in this thesis. A topic for future investigations can be the study of various nozzle configurations (with and without blade), the acceleration from gas cells and the impact of different laser pulse param-

	Phuoc et al. [37]	Tsai et al. [66]	Khrennikov et al. [73]	Results Chapter 4.1
Electron distribution	$\approx 100\,\mathrm{MeV}$, broad	$50-90\,\mathrm{MeV}$, peak	$17-50\,\mathrm{MeV}$, peak	$50-100\,\mathrm{MeV}$, peak/ broad
X-ray beam divergence [mrad]	18	20	-	20-50
Total number of photons	10^8	2×10^7	-	4×10^6
Number of photons at specific energy [keV^{-1} 0.1% BW]	3×10^4 at 100 keV	1.1×10^4 at 90 keV	$5-10\times10^3$ at 15 keV	1.6×10^4 at 100 keV
Source size [μm]	<3	6	$13-30$	-

Table 4.1: The interaction parameters and X-ray beam properties are listed for a comparison between the results presented in section 4.1 and the published results of three other research groups.

eters on the electron beam stability and quality. The number of photons emitted by the X-ray source is in the middle range compared to other experimental investigations. An outstanding result, excelling the other by nearly two order of magnitude is reported by Phuoc et al. [37]. The latter additionally measured the source size with the knife edge technique and obtained a value of less than $3\,\mu$m. Another approach is to assume the X-ray source size to be equal to the electron beam diameter at the collision point, which is at best an upper limit [73]. In order to calculate the brilliance of the X-ray source, the source size should be measured precisely in future campaigns.

Tsai et al. studied comprehensively the laser intensity and profile after the interaction with the gas jet and the reflection on the recycling mirror. Values of a_0 between $0.6-1.2$ are reported, shooting onto a gas jet with electron densities in the range of $1.7-2.2\times10^{19}\,\mathrm{cm}^{-3}$, confirming the estimation in section 4.1.2. For future investigations, the Arcturus laser facility offers the opportunity to implement a second, counterpropagating beam, which make recycling of the first laser pulse obsolete. The second pulse can be focused on the electron bunch, in order to reach intensities in

the nonlinear regime to trigger high harmonic Thomson scattering.

Frequency upshift of laser light on fast moving electron mirrors generated from solid targets was theoretically studied over the past decades. Despite the high experimental demands, evidence supporting this theory was recently found. Kiefer et al. [36] report on relativistic electron mirrors from nm scale DLC foils. When shooting synchronously on the rear target side with a second infrared pulse, a coherent frequency upshift to the range of 20 eV is observed. The radiation spectrum is enhanced at harmonic orders of the laser frequency, which is the result of dense, monochromatic electron mirrors. The acceleration from ultra thin targets requires a very high laser contrast, which can be achieved by implementing a double plasma mirror. In case of the experiment described in section 4.2, a single plasma mirror is used and a 27 nm target. PIC simulations of this setup predict dense electron layers with a rather broad energy distribution. Thus, the X-ray diagnostics is designed in such a way that a rather broad and higher energetic frequency upshift can be detected. Paz et al. [75] accelerated fast moving electron layers from μm thick aluminium foils. The backscattered radiation from the counterpropagating infrared laser pulse was in the range of $50-70$ eV. The enhanced yield in this energy range occurs when the timing between drive and scatter pulse is in the range of 100 fs. In the experiment presented in this thesis it was possible to more than double the backscattered X-ray energy. One factor is the choice of target and laser intensity. The electron acceleration from tens of nm scale targets in combination with a laser pulse in the range of 10^{20} produces $2-3$ MeV electron layers. Irradiating these layers with an intense 2ω scatter pulse leads to an X-ray signal of up to 1 keV. The disadvantage of using a 2ω pulse is that the electron layers become underdense in a shorter amount of time, as the critical density for blue is

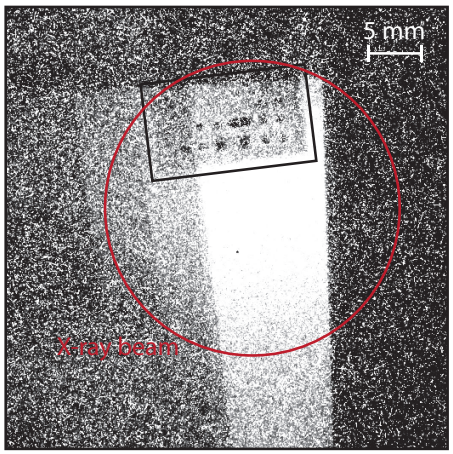

Figure 4.19: Single exposure radiograph of a USB-stick. The X-ray beam is marked with a red circle. The inner structure of the USB-stick is clearly identifiable.

higher than for infrared. Thus, the rate of enhanced shots is rather low, as it is more difficult to meet the conditions for efficient Thomson scattering.
In summary, the recycling mirror geometry is currently much more advanced than the scattering of a laser pulse on a relativistically moving electron mirror from thin foils. The latter is experimentally extremely challenging to implement and has a low repetition rate due to the fragile targets. On the other hand, it bears striking advantages and is thus highly beneficial to investigate further. Both techniques for an all optical X-ray source are in the stage of fundamental research and a promising alternative to synchrotron radiation. The radiograph of a USB-stick, recorded during the experiment, is shown in figure 4.19 and demonstrates just one example for future applications. By implementing a pinhole into the setup the image quality can be enhanced, as diffuse background radiation from other sources can be eliminated.

X-ray line emission from hot dense plasma

This Chapter is dedicated to present the investigation of the radiative properties of hot dense plasmas in the X-ray and XUV regime. Ultra short X-ray flashes, produced in hot dense plasmas, can be applied in the field of radiography or crystallography, e.g. the observation of fast processes in biological atomic structures [31]. As the emitted radiation also contains information about plasma parameters and dynamics, its detection and analysis comprises to an important plasma diagnostic. Hot dense plasmas can be found in the interior of stars, making the interaction of laser pulses with matter ideal for laboratory experiments to investigate the field of astrophysics [6] [76].
In this chapter, the radiation emitted during the transition of an excited ion into its ground state, called line emission, is studied. Various plasma conditions, created during the interaction with a heater beam, are probed at different times by a ultra short, laser pulse. The resultant emission yield is analysed. Its trend is verified by simulation results from a hydrodynamic code in combination with an atomic physics code. Finally, the line emission in dependency of the target thickness is investigated in order to determine the plasma electron temperature.

5.1 Setup

The investigation of line emission from various plasma conditions with ultrashort laser pulses were carried out during the experimental campaign of Thomson scattering (section 4.2) using setup II. As the two studies involve the application of a second beam, and the detection of X-ray radiation, the setup suits both. A detailed

drawing of setup II is shown in figure 4.13 and the description can be found in section 4.2.1. Here, some adaption and the main parameters, including their function in the context of the investigation presented in this chapter are given.

Table 5.1 gives an overview of the beam parameters and figure 5.1 shows a schematic

	ω Main	2ω Heater
Wavelength λ [nm]	800	400
Focal spot FWHM [μm]	3	50
Pulse duration τ [fs]	30	100
Intensity I [W/cm^2]	10^{20}	10^{16}

Table 5.1: Parameter of the two beams involved in the interaction.

of the different irradiation conditions applied during the experiment. Most interesting is irradiation condition a); the delay between both beam is positive, which means that the 2ω heater pulse interacts with the target first. The ultra short main beam arrives later and deposits its energy in an already expanded target. A negative delay between the pulses is illustrated in b). The tightly focused ω main beam reaches the target before the heater beam. The situation described in c) is used as a reference, where just the main beam is fired.

The target composition and thickness, given in section 4.2.1, are important param-

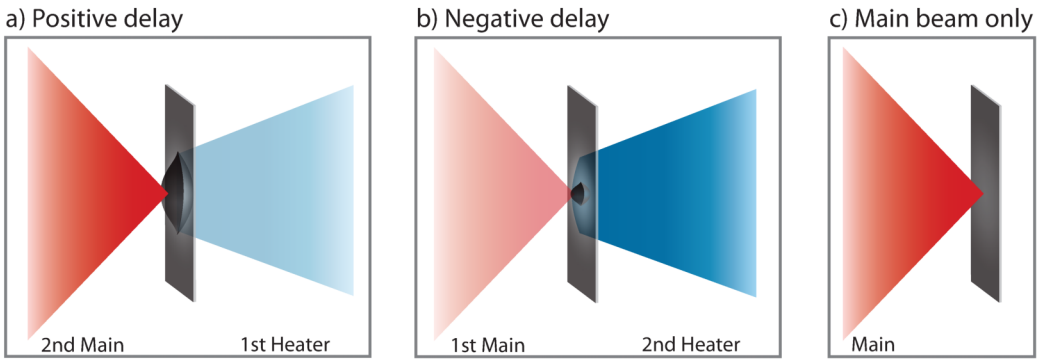

Figure 5.1: Temporal arrangement of the pulses; a) 2ω heater pulse arrives before ω main pulse, b) ω main pulse arrives before 2ω heater pulse. In c) only the main pulse is applied.

eters regarding possible radiative transitions. The X-ray diagnostic, a transmission grating, is designed to resolve photons between 0.5-2 keV. This range matches the emission associated with a highly ionised low-Z plasma, which is created when irra-

diating DLC and parylene foils. The transmission grating setup is equipped with a slit (instead of a pinhole), in order to simplify the identification of isolated lines in the spectrum. The spatial and temporal overlap of the two beams is guaranteed by applying the methods described in section 4.2.1. A spatial jitter of maximum 20 μm and a timing precision of 300 fs are found. Other diagnostics, which are visualised in figure 4.13, namely the electron spectrometer and the low intensity optical probe, are not in use for the investigation on line emission.

5.2 Time integrated emission spectra of low-Z targets

A typical spectrum using a DLC foil target is shown in figure 5.2 a), where the resonance lines of oxygen He-like ions and lines of the Lyman series of carbon H-like ions are identified. During the target preparation process, the DLC foils are in permanent contact with water or air, causing the oxidation of the material. Thus, it is not surprising to find O VII $1s^2$-$1s2p$ (O He$_\alpha$, 21.60 Å) and O VII $1s^2$-$1s3p$ (O He$_\beta$, 18.63 Å) lines among the emitted radiation. Despite the high content of carbon in the target material, the emission of carbon He-like ions is not visible and C VI $1s$-$2p$ (C Ly$_\alpha$, 33.73 Å) and C VI $1s$-$3p$ (C Ly$_\beta$, 28.47 Å) lines are rather weak. The X-ray diagnostic, a 5000 lines/mm Au transmission grating, is deposited onto a 1 μm plastic foil, which reabsorbs most of the lines emitted by carbon ions.

Figure 5.2 b) pictures typical raw data recorded when irradiating thin parylene F targets ($H_8C_6F_2$). Fluorinated parylene is a polymer, consisting predominately of hydrogen and carbon. But due to its low mass density, the amount of carbon is more than one magnitude lower compared to the amount of carbon in equally thick DLC foils. The re-absorption effect of the grating material leads in this case to a total absence of carbon ion line emission. The first order of the transmission grating can resolve three lines of the parylene F plasma spectrum: F IX $1s$-$2p$ (F Ly$_\alpha$, 14.98 Å), F IX $1s$-$3p$ (F Ly$_\beta$, 12.64 Å) and F VIII $1s^2$-$1s2p$ (F He$_\alpha$, 16.81 Å). The F VIII $1s^2$-$1s3p$ (F He$_\beta$, 14.46 Å) line is to close to Ly_α, thus it only becomes visible in the second order of the transmission grating.

Both spectra do not contain higher line series, such as the transition $1s$-$4p$ (H_γ line). This observation is an effect of a high density plasma, where the binding energy of electrons on upper atomic levels is compensated by the electrostatic potential of

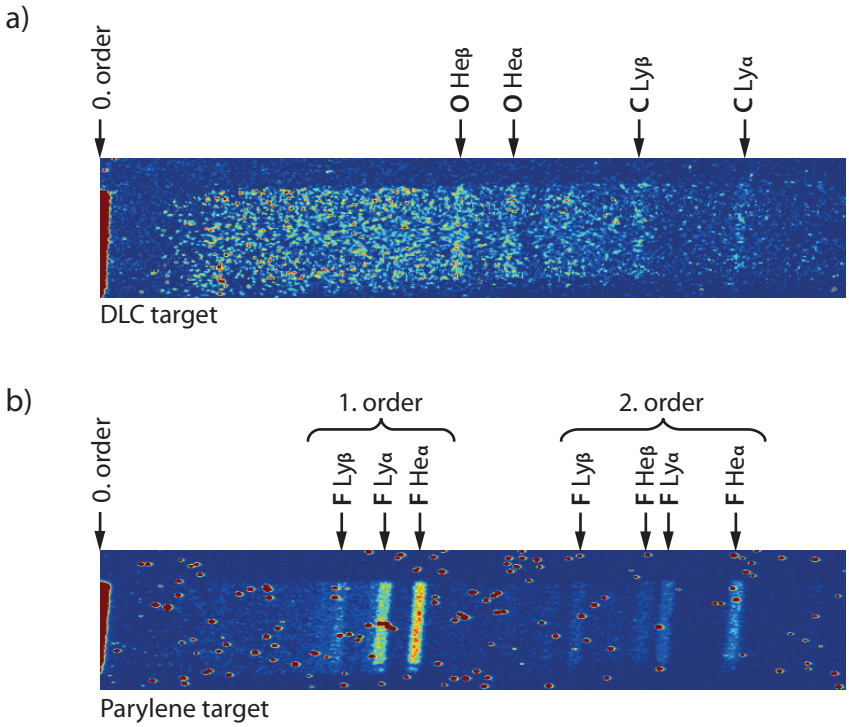

Figure 5.2: Time integrated emission spectra, emitted by a DLC target a) and a parylene F target b), when irradiated by the main high intense laser pulse.

neighbour ions. The bound states are shifted into the continuum, an effect called pressure ionisation, where upper level line emission does not appear [77] [78]. The lack of higher resonance lines is a signature of a high density plasma in spectroscopic measurements, particularly with ultrashort laser pulses, as demonstrated by Osterholz et al. [79].

5.3 Line emission as a function of the relative timing between two beams

The emission yield at various plasma conditions is investigated by scanning systematically the relative delay between the heater beam (B2) and the main beam (B1), by irradiating 27 nm parylene targets. The interaction process can be divided, according to the sign of the delay, into two cases. Applying a delay between −30 ps and 0 ps, means that the strongly focused main beam arrives at the target first. The second,

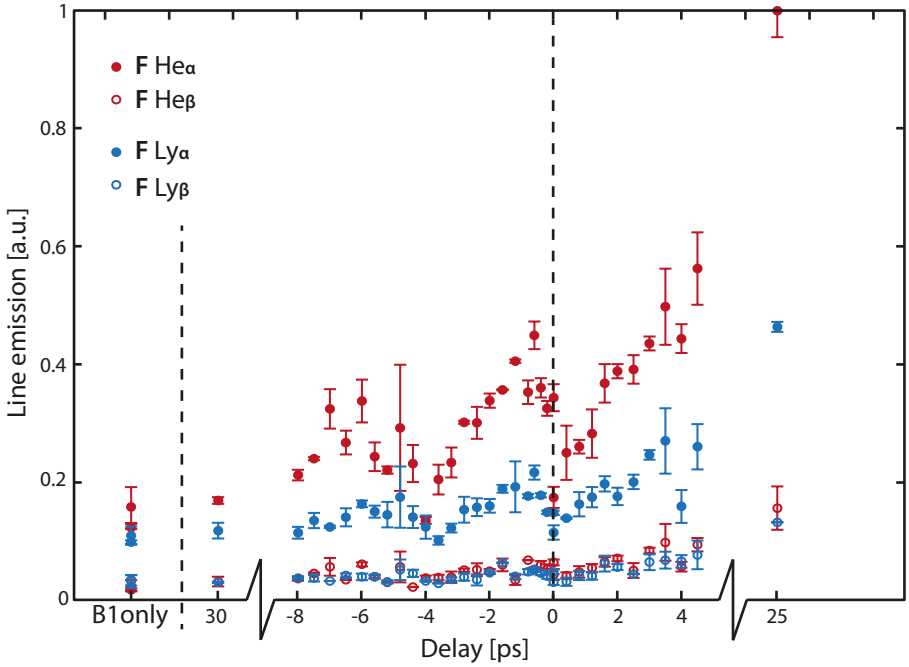

Figure 5.3: Line emission originating from flourine ions in the plasma as a function of the relative delay between the two beams, which are interacting with the target. The X-ray yield is enhanced, when the heater modifies the target before the main beam arrives (positive delay).

and more interesting scenario happens when the delay is positive (0 ps to 25 ps) and the less intense heater beam changes the target conditions before the main beam arrives.

Figure 5.3 presents the results of the study. The yield of the flourine ion lines F He_α, F He_β, F Ly_α and F Ly_β, normalised to the maximum measured value is plotted against the delay between both beams. Note, the x-axis breaks between -30 ps and -8 ps and on the positive side between 4 ps and 25 ps, in order to improve the data visualisation. The first noticeable observation is the strong emission from He-like flourine ions, suggesting that the dominant ionisation degree of flourine atoms is $Z = 7$. The second striking feature is the rising yield from the left side of the plot to the right side, which can be discussed in more detail. The line intensity plotted on the outer left side originates from shots, where only the main beam is applied (B1 only). The yield level of shots, where the main beam arrives tens of ps before the heater, is comparable to main beam only shots. This is an indication, that the ultra thin foil is already completely diluted when the second beam arrives and only the

interaction with the first beam determines the emission features. For the condition that the main beam comes just several ps prior to the heater, the yield increases slowly, while showing a periodic structure. When the heater beam interacts with the target first, the emission behaviour changes in such way, that with increasing delay, the yield rises steadily and stronger than in the case of negative delays. The heater beam is modifying the target characteristics for the interaction with the main beam. The X-ray signal does not change significantly up to a delay of 3 ps. However, for longer delays, for example 25 ps, the line emission is increased by a factor of 5 compared to a main beam only shot.

5.4 Dependency on the target thickness

The experimental study of inner shell line emission from dense plasma involves a scan with two different target thicknesses. Figure 5.4 depicts the results of this scan, showing the normalized line emission yield of C Ly_α, C Ly_β, O He_α and O He_β, detected from the interaction with a 50 nm DLC foil (blue) and a 100 nm DLC foil (red). Additionally, the normalised X-ray yield at different energy values, distributed over the whole spectrum is plotted for both target types. The emitted radiation from oxygen ions is on the same level for thick and thin foils. The oxidised contamination layer on the target is a surface effect only and consequently does not depend on the target thickness. There is clear evidence of a 10% enhancement of carbon Lyman line emission originating from the thin 50 nm DLC target. This enhancement can be quantified by building the integrated line intensity ratios of C Ly_α (C Ly_β) from the interaction with the thin foil to the same lines, originating from the interaction with the thick foil, namely $R_{Ly_\alpha} = 1.1$ and $R_{Ly_\beta} = 1.35$. For the interpretation of these time integrated result, the plasma dynamics have to be considered as a whole, including not only its emissivity but particularly its opacity in dependency of the target thickness. The method of choice to comprise these parameters and dynamics is a hybrid simulation with the hydrodynamic code MULTI-fs and the atomic physic code FLYCHK. By comparing the experimental results to the simulations, the measurement becomes an important plasma diagnostic for the determination of the plasma electron temperature. A detailed description is presented in section 5.5.4, later on in this chapter.

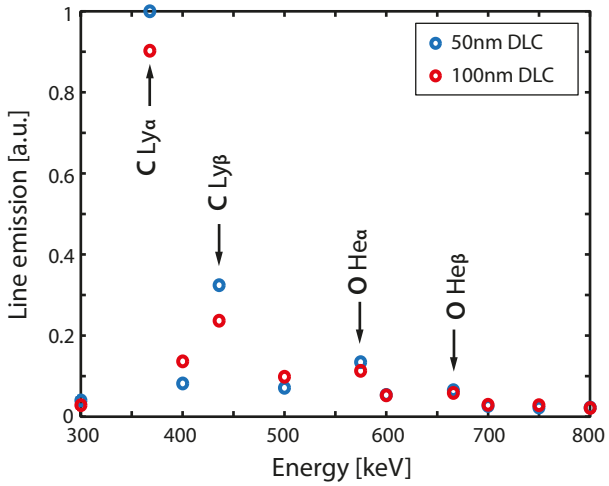

Figure 5.4: Emission spectrum from 50 nm DLC foil (blue) and 100 nm DLC foil (red). The spectra are recorded while applying both beams with a delay between −5 to 0 ps. For the thin target case, the C $Ly_{\alpha/\beta}$ lines are enhanced.

5.5 Simulations and interpretation

5.5.1 Hydrodynamic modeling of varying target conditions

The interaction with a high intense, ultrashort laser pulse initiates a rapid heating process, a plasma is created and starts to expand into vacuum. During this process, the plasma parameters are highly transient, changing from hot and dense to cold and diluted in a time scale of tens of ps. The plasma electron density, the plasma temperature, the ionisation degree and the plasma size are evolving as a function of time and space and are also responsible for the emissivity and opacity of the medium.

Figure 5.5 shows the results of the 1D Lagrangian hydrocode MULTI-fs. The simulation setup follows closely the experimental configuration of the plasma expansion initiated by the heater beam. In the simulation, the interaction of a 100 fs laser pulse with an intensity of $10^{15}\,\mathrm{W/cm^2}$ at normal incident to a thin target is modeled. The target is designed as a 30 nm carbon layer, with a density of $1.65\,\mathrm{g/cm^3}$, a typical value for parylene foils. The fraction of flourine atoms in the parylene foil is not considered. However, both species are low-Z materials. Thus, the temporal evolution of the density and the ionisation degree is assumed to be similar. The simulation grid consists of $N = 100$ Lagrangian cells, which are monitored in time intervals

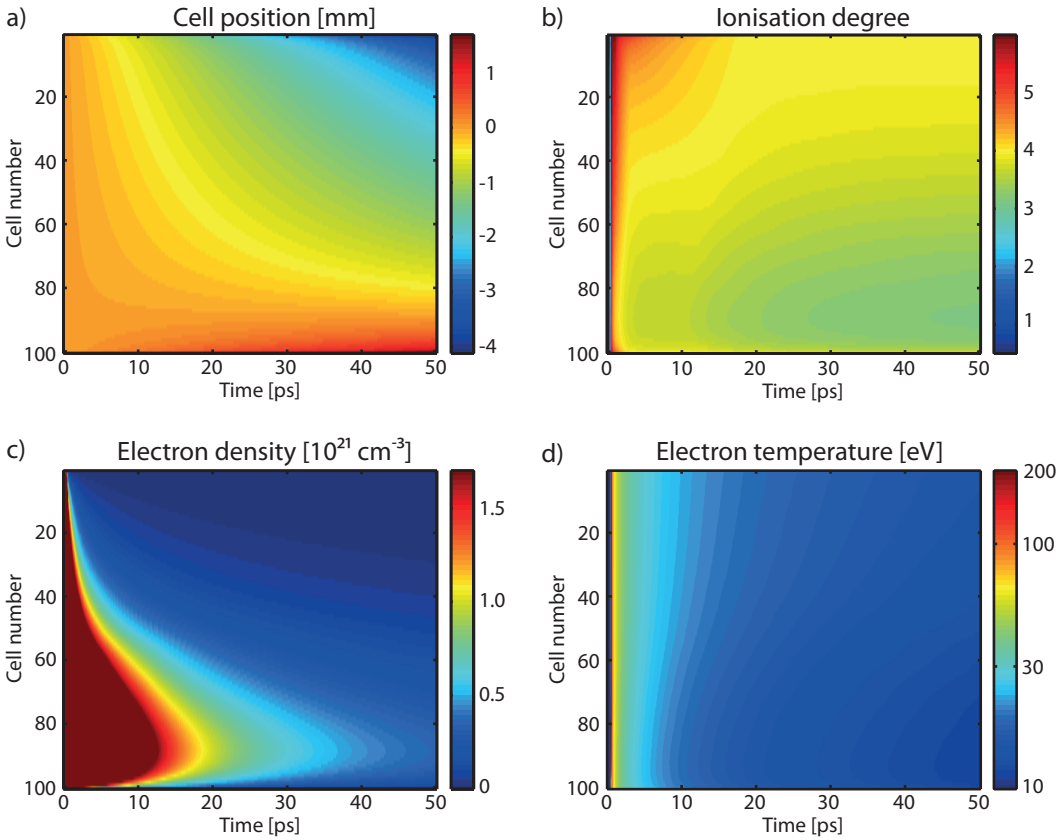

Figure 5.5: Temporal evolution of physical plasma parameters simulated using the 1D hydrodynamic code MULTI-fs. The results show the a) cell position, b) ionisation degree, c) electron density, d) temperature of a 30 nm target interacting with the 10^{16} W/cm^2 heater laser pulse.

of $\Delta t = 0.1$ ps up to 50 ps. Different flux limiter values are tested. Compared to other theoretical work on hydrodynamic simulations [79] [80], the best agreement is obtained using a flux limiter of $f = 0.01$.

The plots in figure 5.5 illustrate the temporal evolution of the most important plasma parameters, namely the cell position a), the ionisation degree b), the electron density c) and the plasma electron temperature d). As soon as the laser pulse peak hits the target, it becomes instantly fully ionised. This condition lasts for less than 2 ps as the plasma temperature drops dramatically and recombination takes place. The dominant species between $2 - 12$ ps are two-electron atoms. The temporal evolution of the ionisation degree fits well to the experimental data, which show a strong emission of He$_\alpha$- and He$_\beta$-like lines originating from two-electron flourine atoms.

The cell position at the front and rear side of the target (a), in combination with the electron density (c), provide information about the density gradient at the target boundaries. The target profile changes from a rectangular shape to a curve with slow decay. A parameter, which describes the density gradient at the target front side, is the plasma scale length which is defined as $L = |\frac{d}{dx} log n_e| x = x_c r$. With increasing time after the interaction with the heater beam, the plasma scale length increases. After 12 ps the plasma becomes completely underdense $n_e < 1.7 \times 10^{21}\,\mathrm{cm}^{-3}$ and extents to 5 μm FWHM.

Target profile effect on the laser absorption

The entire interaction process of the main pulse with the pre-heated plasma, starting from the coupling of laser energy into the plasma, the ionisation and recombination time scales, to the creation of strong electromagnetic fields and the subsequent acceleration of particles, strongly depends on the heated plasma profile. In the case of the results presented in this section these properties, namely the plasma scale length and the electron density change dramatically over the time scale of the experimental delay scan. Thus, the line emission properties of the different species in the plasma can change significantly, when varying the relative timing between the heater and the main beam.

Figure 5.6 a) displays a plot of the reduced plasma scale length L/λ_L as a function of the time after the interaction with the heater beam, based on the simulations presented in figure 5.5. The plot can be divided into three regimes: up to approximately 5 ps, the scale length can be treated in the limit $L \ll 1$, between $5 - 8$ ps the scale length is comparable to the laser wavelength, and for longer delays, the plasma scale length becomes a multiple of the laser wavelength. These classifications play an important role, when talking about the absorption process and the energy gain of a target interacting with a high intense laser pulse. Several mechanisms contribute to the coupling of laser energy into overdense targets, which are described in detail in chapter 2.5. The dominant mechanism for an extremely high intense ($I > 10^{19}$ W/cm^2) laser pulse, which is normal incident onto a steep gradient plasma is $\mathbf{J} \times \mathbf{B}$ heating [26]. However, small density gradient modifications, introduced by a prepulse or by the heater beam, influence the interaction immensely. Cai et al [82] found analytical solutions for the contribution of the plasma scale length on the absorption via

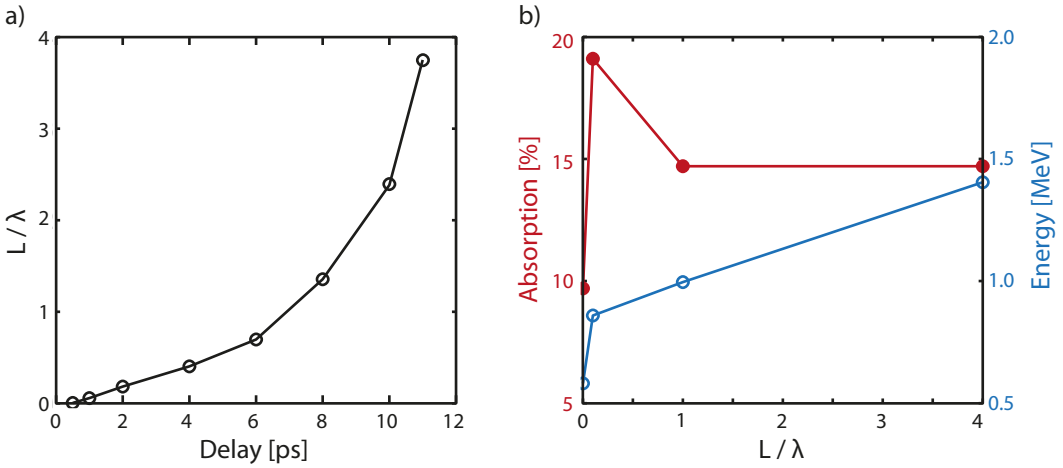

Figure 5.6: a) Reduced plasma scale length as a function of the relative delay between heater and main laser pulse. The curve is obtained from the electron density evolution and cell position of hydrodynamic simulation results. b) Absorption and average hot kinetic energy as a function of the plasma scale length. The data points are taken from the PIC simulation results of Lefebvre and Bonnaud et al. [81].

$\mathbf{J}\times\mathbf{B}$ for $L \ll 1$. For a wide range of the normalised laser amplitude a_0, an increasing power absorption rate is calculated, when the scale length grows. Lefebvre and Bonnaud [81] investigated nonlinear electron heating over a wide range of parameters, including the density gradient length L in the range of $0-15$. Figure 5.6 b) shows the results of their 1.5D PIC simulation, where a maximum electron density of $n_e = 17n_{cr}$ with $L = 0, 0.1$, and 1, and a smaller maximum electron density of $n_e = 9n_{cr}$ for the case of $L = 4$ is used. The normalised laser amplitude for the values presented in the graph is $a_0 = 5.5$. For a small scale length, the absorption is increased by a factor of 2 compared to the case of an infinitely steep plasma gradient. For a scale length in the order of the laser wavelength, the absorption fraction drops again and slowly rises for multiple of the laser wavelength. More interesting is the behaviour of the average hot kinetic energy, which increases for a scale length of $L = 0.1$ to 4 linearly and is a measure for the X-ray line emission intensity. The point of the critical density is inside the plasma, which leads to an interaction of the underdense fraction of the plasma with a standing wave (incoming, and reflected fraction of the laser pulse) [82]. The stochastic oscillation, triggered by this interaction leads to a stronger energy gain [83].

The parameter regime, regarding laser amplitude, plasma density and plasma scale

length of the experiment discussed in this chapter is by all means comparable to the regime investigated by Lefebvre and Bonnaud [81]. Thus, the experimental result in section 5.3, which shows an X-ray line emission enhancement with increasing delay between heater and driver beam, can be qualitatively explained by the advanced energy gain of the plasma with rising plasma scale length.

5.5.2 Hydrocode and atomic code hybrid to calculate enhancement in line emission

In order to confirm the experimental trend and the theoretical considerations, a simulation hybrid of the hydrocode MULTI-fs and the atomic physics code FLYCHK is performed. The plasma expansion of three different target conditions, corresponding a delay of t= 0, 10 ps and 15 ps is modeled with MULTI-fs in a similar manner to the simulation of the interaction with the heater beam. Only the laser intensity and wavelength is adapted in such way, to fit the interaction with the driver beam. In

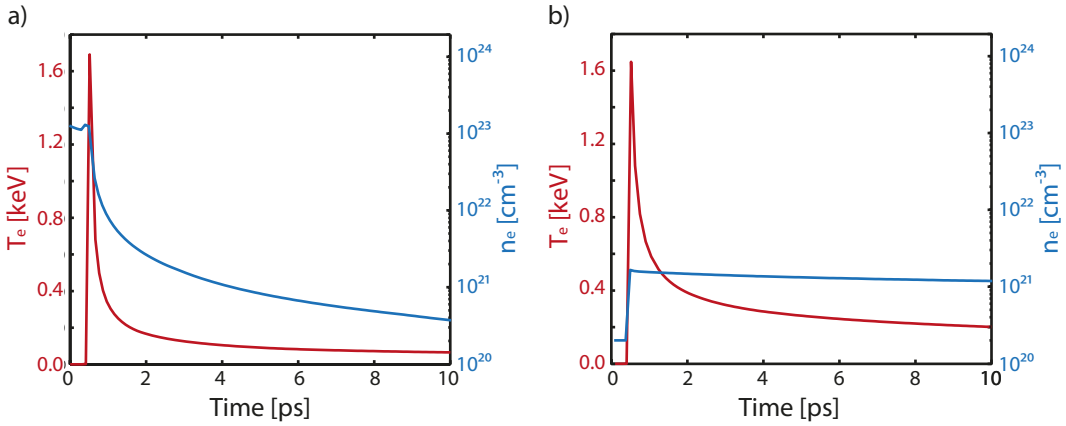

Figure 5.7: Time history of the plasma electron temperature and the electron density for the interaction with a steep gradient target, corresponding to a delay t= 0 ps a) and a diluted target corresponding to a delay t= 15 ps b). The graphs are results of hydrodynamic simulations.

figure 5.7 the electron temperature and electron density evolution of the simulation with a steep gradient target (t= 0 ps) and an expanded target (t= 15 ps) are plotted, respectively in a) and b). The plasma temperature of the steep gradient target drops much quicker than the one of the expanded target, while the maximum temperature of both is rather similar. The electron density at the time, when the plasma reaches

its highest temperature, is two orders of magnitude lower for the diluted target. The density decline is therefore stronger for the steep gradient target, while the electron density of the diluted target stays rather constant.
The plasma temperature, the electron density and the plasma size in dependence of the time are fed into FLYCHK code in order to calculate the line emission intensity of F He_α. The parylene target ($H_8C_6F_2$), used during the experiment, contains only 14% flourine, which is considered in the FLYCHK input file.
On the basis of these parameters, the code is able to calculated the spectroscopic intensities of given plasma conditions at different moments of time. The calculated intensity of a line emitted at the frequency ν is defined as

$$I_\nu = S_\nu(1 - e^{\tau_\nu}), \tag{5.1}$$

with the source function S_ν and the optical depth τ_ν, which are given by

$$S_\nu = \frac{\epsilon_\nu}{\kappa_\nu} \text{ and } \tau_\nu = \kappa_\nu L. \tag{5.2}$$

The emissivity ϵ_ν and the opacity κ_ν depend on the level populations, the density and the geometric length L of the plasma layer [84]. For the highly transient conditions of a laser pulse heating a thin target, the system is considered in a non-LTE mode and time dependent.

The line intensity evolution of F He_α for the interaction with the different target conditions is shown in figure 5.8. The red data points correspond to the simulation, when the target is not preheated, which leads to the lowest line intensity. The blue and black curve are results of the simulation for a delay of 10 ps and 15 ps respectively. The line emission becomes stronger with increasing delay between the two beams, which matches the experimental data presented in figure 5.3. The peak intensity in the temporal evolution of each case moves with increasing delay to later times.
Taking into account the input density and temperature evolution, this shift and the increasing line intensity can be explained as follows: The electron density is an important parameter for the line intensity, while the plasma temperature is responsible for life time of specific ion population levels. At early times, when the plasma is fully ionised, the line emission of hydrogenlike flourine (F Ly_α) is most prominent. Thus, the high initial electron density for t= 0 (figure 5.7 a)) has no effect on the line

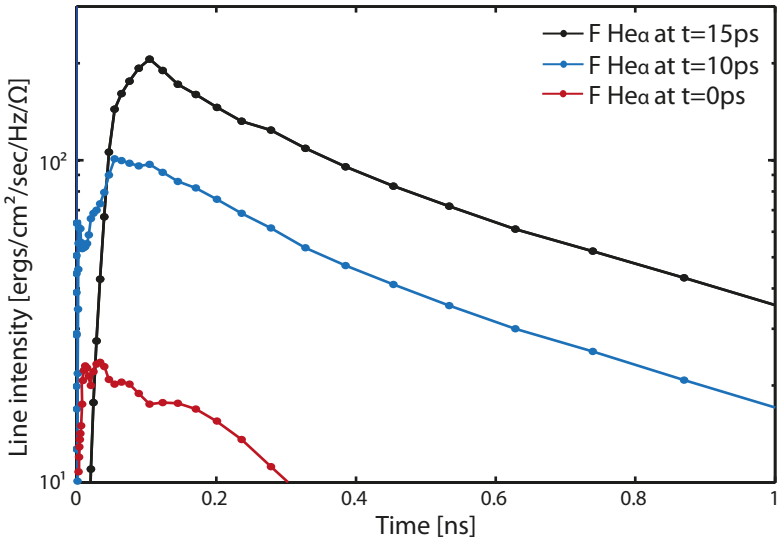

Figure 5.8: Line intensity of F He_α calculated by the atomic physics code FLYCHK for different target conditions.

intensity of F He_α. The ionisation distribution calculated by FLYCHK reveals, that heliumlike flourine becomes dominant in the time $20 - 400$ ps after the interaction. In this time interval, the density (and consequently the line intensity) of an initially stronger expanded target (figure 5.7 b)) is higher than the density of the case t= 0. The temporal shift of the peak intensity correlates to the evolution of the plasma temperature for the different cases. For an increasing delay between the two beams, the plasma stays longer hot, which affects the life time of the heliumlike flourine atoms.

5.5.3 Discussion

In this chapter, the X-ray radiation originating from plasma interacting with two laser pulses is studied. The double pulse approach is a recently highly investigated topic in laser plasma physics, including improvements regarding the acceleration of ions [8] or the double stage electron acceleration [12]. In the research of materials and in the low laser intensity regime, the double beam geometry is establish in laser induced breakdown spectroscopy [7]. Similar to the results in this chapter, the first laser pulse is used to heat the target material, in order to enhance the X-ray signal emitted after the interaction with a second beam. For ultrahigh laser intensities, different groups

investigated various parameter regimes. Eidmann et al. [85] measured the Al K-shell emission and resonance lines after focusing a single high intense, ultra short laser pulse and a double pulse (one delay: 25 ps) onto an aluminium block. The resonance line emission (Al Ly_α and Al He_α) are stronger in the double beam case, while the continuum part of the spectrum is weaker compared to the spectrum generated by a single laser pulse. Bastiani et al. [86] studied the K-shell emission from solid SiO_2 as a function of the initial plasma scale length by introducing a prepulse. An increasing signal of K_α emission for a prepulse delay up to 10 ps was found. The results are in strong relation to the absorption measurements preformed during the same campaign. Investigation on K-shell emission are interesting, particularly for rather thick targets, as it provides information about deeper plasma layers.
In the experiment, described in this section, targets in the range of tens of nm are used. Ultrathin targets have the advantage that they are heated more uniformly, and effects of spatial temperature gradients are reduced [87]. The temporal profile of the ultrashort main pulse can be described almost as a delta function, causing a laser energy deposition into the plasma within a negligible amount of time compared to the time scale of the plasma emission. Thus, the radiation originating from this hot dense plasma state depends predominantly on the initial target conditions. The presented data show both, the function of the setup as a diagnostic of various hot dense plasma conditions and the application as a energetically narrow X-ray source. Nonetheless, the topic on line emission from a plasma in a double beam geometry deserves further computational and experimental investigations. The simulation can be improved by employing a PIC code, particularly for the modeling of the interaction with the high intensity main beam. Different atomic species in form of various target materials can be studied, while scanning a larger delay interval. The optimisation of these two parameters, in the view of an enhanced X-ray signal can be a step towards a strong and ultrashort X-ray source.

5.5.4 Plasma temperature diagnostic

The line emission from hot dense plasma, particularly the intensity ratios of lines originating from highly ionised atoms are of great interest when diagnosing the plasma temperature. The simple observation of those lines, provides a method in order to estimate the lower limit of the plasma temperature. Considering the ionisation energy,

required to create hydrogenlike species, the corresponding temperature can be calculated. In the experimental study presented in section 5.4, C Ly$_\alpha$ and C Ly$_\beta$ emission is measured, which occurs exclusively in plasma with a temperature of more than 300 eV. A more accurate estimate is achieved by looking at the line intensity ratios of C Ly$_\alpha$ (C Ly$_\beta$) from the interaction with a 50 nm DLC foil to C Ly$_\alpha$ (C Ly$_\beta$) from a 100 nm DLC foil.

In the following, these values are compared to line intensity ratios calculated in a combined simulation of the hydrocode MULTI-fs and the atomic physics code FLYCHK. The heating process of the experimental conditions are modeled by covering a certain input parameter regime, including a scan of the laser intensity and the flux limiter. These values have an affect on the peak plasma electron temperature which, in return, can be determined when the simulation results fit the experimentally measured ratios.

In a first step, the temporal evolution of the plasma expansion of a 50 nm carbon layer is calculated with MULTI-fs. The simulation setup is similar to the one described in the last section 5.5.1, except that the plasma expansion is modeled for a longer time interval, up to 1.5 ns. The target dimension is adjusted to 50 nm and the peak laser intensity is increased in order to model the interaction with the high intensity main beam. A second run is performed, changing only the target thickness to 100 nm. Figure 5.9 a) and b) shows the results of the plasma expansion simulation. While for both cases the same laser intensity is applied, the thin target becomes hotter than the thick target. In experimental studies on mass-limited targets, this effect has been observed before [88] [89]. In thin targets, the absorbed laser energy is concentrated near the focal spot, while in thicker targets, the heat is transported and distributed over a larger amount of target material. The different temporal evolution of the electron temperature, the electron density and the opacity size are considered in the following simulation of the line emission yield. The MULTI-fs output data of both runs are organised in the shape of a history input file for the code FLYCHK. Figure 5.9 presents the line intensity evolution for C Ly$_\alpha$ resulting from the calculation with the 50 nm (blue) and 100 nm (red) carbon layer. The results are based on the MULTI-fs simulation a) and b), in which the thin target reaches a maximum electron temperature of 1150 eV. Although the intensity maximum in the thick target case is higher, the contribution over the whole time interval has to be considered. The strongest line intensity is emitted a few ps after the interaction and reduces by

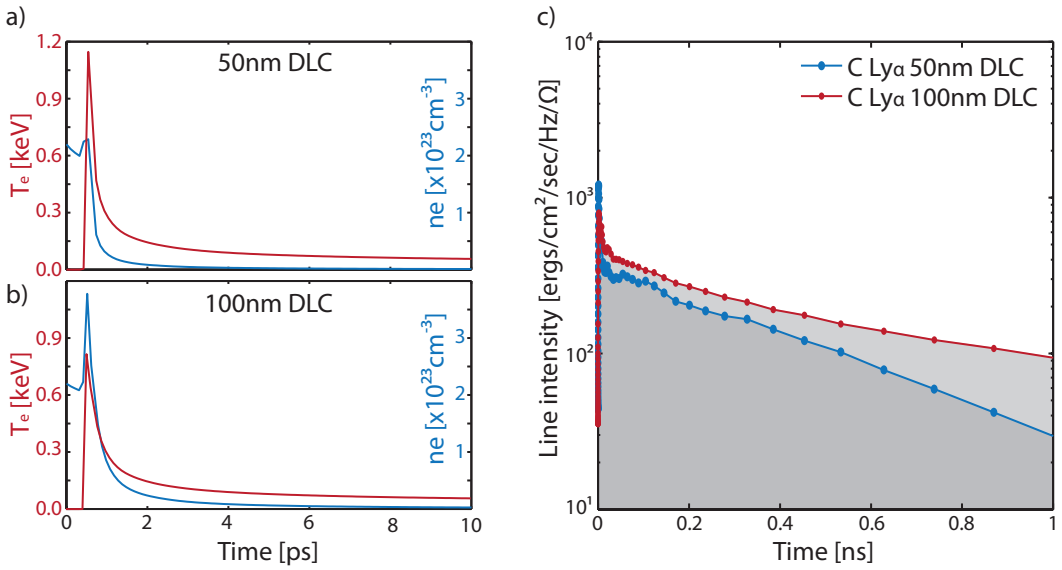

Figure 5.9: Time history of the plasma electron temperature and the electron density for the interaction with 50 nm DLC target a) and a 100 nm DLC target b) obtained from hydrodynamic simulations with MULTI-fs. c) Atomic code FLYCHK results, showing the temporal evolution of the C Ly$_\alpha$ line intensity based on the plasma expansion displayed in a) and b).

half within 2 ps for the thick target case, and within a much longer time period of 30 ps for the thin target case. This large intensity drop, on a ps time scale shows, that the detected integrated signal originates from the period, where the plasma is hot and dense, and gives important information about the fast plasma dynamics.
After $5-10$ ns the line intensity for both cases decreases more than two orders of magnitude. Thus, is it sufficient to integrate the line intensity over a time interval of 10 ns in order to compare the simulation results to the experimentally measured data. FLYCHK generates the output intensities at discrete time steps i, leading to a time integrated signal $\Gamma(\nu) = \sum_i I_\nu(t_i)\Delta t_i$.
To draw conclusions about the plasma electron temperature, present during the interaction, the values of the integrated emission signal of the thin and thick target case are compared to each other by looking at their ratios $R_{Ly_\alpha}(T_e) = \Gamma_{50nm}(Ly_\alpha)/\Gamma_{100nm}(Ly_\alpha)$ and $R_{Ly_\beta}(T_e) = \Gamma_{50nm}(Ly_\beta)/\Gamma_{100nm}(Ly_\beta)$. The amount of radiation emitted during a specific transition, strongly depends on the plasma temperature and density. By scanning a certain laser intensity range, the plasma expansion (electron temperature and electron density evolution) of both target types is simulated several times

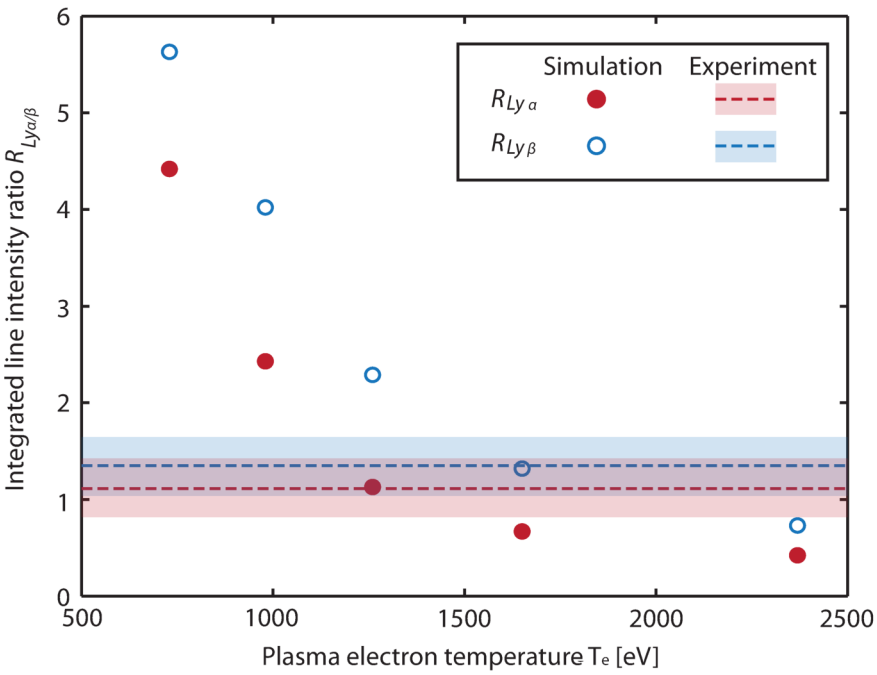

Figure 5.10: Intensity ratio of C Ly lines originating from the interaction with a 50 nm carbon layer and a 100 nm carbon layer. The dashed lines represent the experimentally measured ratio.

using MULTI-fs. The results are processed in FLYCHK in order to calculated the ratios $R_{Ly_\alpha}(T_e)$ and $R_{Ly_\beta}(T_e)$ for different initial plasma temperatures. In figure 5.10 the temperature scan and the corresponding ratios are plotted and compared to the experimental values (dashed lines) obtained in section 2.5. The intersection of simulation results and measured data is at an temperature interval between 1500 eV and 1900 eV.

Discussion

Plasma spectroscopy comprehends many important diagnostic methods of hot plasmas. By measuring the intensity ratio of two lines within the same charge state, for example Lyman$-\alpha$ and Lyman$-\beta$, the ratio of the partial densities of the initial excited states can be calculated. This ratio is related to the plasma temperature and density, which makes the method suitable for a hot plasma diagnostic [32]. The line ratio emitted from two differently ionised atoms is often easier to measure, because

the emission of α lines is stronger than the emission of β lines. Jiang et al. [90] obtained the plasma temperature by detecting He_α and Ly_α lines produced by focusing a 10^{18} W/cm^2 laser pulse onto a 130 μm Al target. Osterholz et al. [91] considered the same ratio, but used different atomic species in the spectroscopic calculations with FLYCHK and compared the results to experimental data. For short living plasmas, the hydrogenlike lines originate from a part of the plasma which is hotter than the part, where heliumlike line emission is dominant. Thus, dealing with two different species introduces a certain complexity in the analysis, which may lead to incorrect results [32]. Highly resolved spectroscopic measurements give the opportunity to analyse the spectral line shape, which provides valuable information about the local plasma conditions, particularly the plasma density [92] [93]. The line ratio of satellite to parent line intensities is used in a large number of experiments to diagnose the plasma temperature [94] [95]. For both techniques, an X-ray spectrometer with a resolution in the sub-angstrom range is necessary. Crystal spectrometer, which are based on Bragg's law offer such a high resolution for an X-ray range up to 100 Å.
The spectra, analysed in the context of this thesis are recorded with a grating spectrometer. Its resolution is not sufficient to distinguish between satellite and parent lines or to identify modifications in the line shape. However, the method developed in this chapter has the unique advantage, that the plasma electron temperature can be determined by measuring the integrated line intensity of only one line emitted from two different plasma conditions. The required simulations rely on the assumption that the spatial density and temperature distributions after the interaction with the laser pulse are rather uniform, which is a reasonable approximation in the case of ultrathin targets [95].

Conclusions and Outlook

In this chapter, the experimental investigations and computational results presented in the thesis are reviewed and discussed in the prospect of future experimental campaigns.

The generation and diagnosis of X-ray radiation related to laser-matter interaction, involving two ultrashort, high intense laser pulses was studied. X-ray radiation originating directly from hot dense plasmas and the production in secondary processes, namely the scattering of photons on laser accelerated electrons are addressed. The results obtained, advance the understanding of hot dense plasmas and contribute considerably to the development of novel X-ray beam sources.

In the first part of this work the generation of X-rays via Thomson scattering of light on laser accelerated electrons was investigated using two different setups. For one setup, the electron acceleration in the SM-LWFA regime from a gas target was studied by varying the gas valve backing pressure. The most stable electron beams, with quasi monoenergetic electron spectra around 100 MeV, were detected at an electron density of $2.3 \times 10^{19}\,\mathrm{cm}^{-3}$. After the interaction with the gas jet, the remainder of the laser pulse was reflected back by a thin glass plate, acting like a plasma mirror. An energy measurement of the recycled laser pulse in combination with the detection of the beam profile on a plastic screen revealed a maximum amplitude of $a_0 = 0.9$ at the scattering position. Thus, intense X-ray radiation was generated resulting from Thomson scattering of the recycled pulse on the electron bunch. X-ray beams, with a symmetric Gaussian beam profile and a divergence of $20 - 50$ mrad were detected along the propagation direction of the electron beam. A Matlab code was developed, which considered the experimentally measured electron spectrum of each shot and the transmission of X-rays through a set of copper filter, in order to reconstruct the X-ray energy spectrum. The typical X-ray beam energy was in the range of hundreds

of keV and strongly depending on the electron beam parameter. The signal observed in the experiment was translated into a total number of photons per shot. Finally, the developed X-ray source was characterised with a photon number of 1.6×10^4 ph/keV per 0.1% BW at 100 keV.

For the second setup, the plasma expansion at the rear side of thin foils and the electron dynamics after the interaction with a high intense laser pulse were investigated. An energetically broad, exponentially decaying electron distribution up to several MeV was observed. To demonstrate a temporally resolved density and energy distribution, 2D PIC simulations were carried out. The results revealed the periodic formation of dense electron layers due to $v \times B$ heating, with energies $E > 3$ MeV, traveling in forward direction micrometer scale distances before dispersing. To investigate the backscattering of light on these electron layer, a dual beam geometry was implemented. The second 2ω was focused onto the rear side of the target. As the production and sustainability of the electron sheath is highly time sensitive, the relative delay between the two beams was a crucial parameter. The temporal overlap of both beams was controlled by a setup, which brought both beams to constructive interference on a detection camera, when synchronisation was achieved. By irradiating a 27 nm parylene foils with the intense driver pulse and the counter-propagating 2ω scattering pulse synchronously or with a maximum delay of -300 fs (driver before scattering beam), an enhanced X-ray signal in the range of $0.6 - 1.2$ keV was observed. The behaviour of the X-ray signal for increasing negative delay and for positive delay, namely the absence of shots with an enhanced signal, indicated that the high energy photons originate from Thomson scattering.

The second part of the thesis focused on the study of line emission originating from a hot dense low-Z plasma created by a high intense, ultrashort laser pulse. A limited series of $\mathrm{Ly}_{\alpha/\beta}$ and $\mathrm{He}_{\alpha/\beta}$ lines was detected for two different target materials. Various plasma conditions were created by heating a 27 nm parylene foil with a low intensity 2ω laser pulse and letting it expand up to tens of ps before the interaction with the high intense main pulse. The results showed a line intensity enhancement with increasing delay between the heater and the main laser pulse. The radiation yield for the transition configuration $1s^2 - 1s2p$ of helium-like flourine ions increased by a factor of 5, when the heater pulse arrived up to 25 ps earlier. Simulations of the plasma expansion with the hydrodynamic code MULTI-fs revealed that the plasma scale length becomes longer with increasing delay, thus the absorption of the second

beam is more efficient. Calculations with the atomic physic code FLYCHK for the line intensity, including opacity effects, confirmed the experimentally measured trend. Important in this context is the time interval in which the population of helium-like ions is at its maximum, which is tens of ps after the interaction. Hydrodynamic simulations showed, that at this point the electron density of a pre-expanded target is higher than the electron density of an initially steep gradient target.
Futhermore, an increased line intensity from a 50 nm DLC foil in comparison to a thicker 100 nm DLC foil was found. A simulation hybrid of the hydrodynamic code MULTI-fs and the atomic physic code FLYCHK was applied in order to model the plasma expansion and related line emission. The simulation results and the experimentally measured line intensity ratios from both target types matched for a plasma electron temperature in the range of 1500 eV and 1900 eV.

Both setup were build up and used in this form for the first time at the Arcturus laser facility and the results constitute a successful proof that both, dual beam experiments in counter-propagating geometry and the development of an all laser based X-ray source can be implemented.
The results obtained in the experiment on line emission from various target conditions showed that spectroscopy is a powerful tool for the diagnostic of hot dense plasmas. Additionally an optimisation regarding the intensity of a narrow band (resonant line) X-ray source was achieved by manipulating the target properties. In the next step, the source can be further enhanced by scanning a larger time interval of the delay between the two beam. Different target compositions and thicknesses can be investigated and the X-ray energy can be adapted according to the application by choosing the most suited foil material.
Inspired by the results of the X-ray generation via Thomson scattering, a prospect for further investigations on this topic is an improvement of the electron acceleration in terms of energy, flux and stability. An experimental campaign can be dedicated exclusively on this topic, testing different schemes including the acceleration from gas jets, gas cells, capillaries and from ultrathin solid targets. Furthermore, the intensity of the scattering laser pulse can be enhanced in order to enter the regime of nonlinear Thomson scattering. One approach is to increase the efficiency of the KDP crystal, which is responsible for the conversion into 2ω laser light. Another way is to use a more powerful laser pulse. At present, a new 6 J pump laser is added into the ampli-

fication chain of each of the two arms at the Arcturus laser facility. With the extra pump energy, the aim is to increase the output energy to 7 J before compression. In the course of this upgrade and by using fast focusing optics, intensities of up to $10^{21}\,\mathrm{W/cm^2}$ can be reached. This will enable the study of new regimes and improve the concepts discussed in this thesis.

Bibliography

[1] J. Faure, Y. Glinec, A. Pukhov, S. Kiselev, S. Gordienko, E. Lefebvre, J. P. Rousseau, F. Burgy, and V. Malka. *A laser-plasma accelerator producing monoenergetic electron beams.* Nature, 431(7008):541–544, 2004.

[2] H. Schwoerer, S. Pfotenhauer, O. Jackel, K. U. Amthor, B. Liesfeld, W. Ziegler, R. Sauerbrey, K. W. D. Ledingham, and T. Esirkepov. *Laser-plasma acceleration of quasi-monoenergetic protons from microstructured targets.* Nature, 439(7075):445–448, 2006.

[3] R. Kodama, P. A. Norreys, K. Mima, A. E. Dangor, R. G. Evans, H. Fujita, Y. Kitagawa, K. Krushelnick, T. Miyakoshi, N. Miyanaga, T. Norimatsu, S. J. Rose, T. Shozaki, K. Shigemori, A. Sunahara, M. Tampo, K. A. Tanaka, Y. Toyama, Y. Yamanaka, and M. Zepf. *Fast heating of ultrahigh-density plasma as a step towards laser fusion ignition.* Nature, 412(6849):798–802, 2001.

[4] M. Roth, T. E. Cowan, M. H. Key, S. P. Hatchett, C. Brown, W. Fountain, J. Johnson, D. M. Pennington, R. A. Snavely, S. C. Wilks, K. Yasuike, H. Ruhl, F. Pegoraro, S. V. Bulanov, E. M. Campbell, M. D. Perry, and H. Powell. *Fast ignition by intense laser-accelerated proton beams.* Physical Review Letters, 86(3):436–439, 2001.

[5] K. W. D. Ledingham, I. Spencer, T. McCanny, R. P. Singhal, M. I. K. Santala, E. Clark, I. Watts, F. N. Beg, M. Zepf, K. Krushelnick, M. Tatarakis, A. E. Dangor, P. A. Norreys, R. Allott, D. Neely, R. J. Clark, A. C. Machacek, J. S. Wark, A. J. Cresswell, D. C. W. Sanderson, and J. Magill. *Photonuclear physics when a multiterawatt laser pulse interacts with solid targets.* Physical Review Letters, 84(5):899–902, 2000.

[6] S. V. Bulanov, T. Z. Esirkepov, D. Habs, F. Pegoraro, and T. Tajima. *Relativistic laser-matter interaction and relativistic laboratory astrophysics.* European Physical Journal D, 55(2):483–507, 2009.

[7] V. I. Babushok, F. C. DeLucia, J. L. Gottfried, C. A. Munson, and A. W. Miziolek. *Double pulse laser ablation and plasma: Laser induced breakdown spectroscopy signal enhancement.* Spectrochimica Acta Part B-Atomic Spectroscopy, 61(9):999–1014, 2006.

[8] J. Böker. *Laser-Driven Proton Acceleration with Two Ultrashort Laser Pulses.* Ph.D. Dissertation, Heinrich-Heine-Universität Düsseldorf, 2015.

[9] L. Romagnani, M. Borghesi, C. A. Cecchetti, S. Kar, P. Antici, P. Audebert, S. Bandhoupadjay, F. Ceccherini, T. Cowan, J. Fuchs, M. Galimberti, L. A. Gizzi, T. Grismayer, R. Heathcote, R. Jung, T. V. Liseykina, A. Macchi, P. Mora, D. Neely, M. Notley, J. Osterholtz, C. A. Pipahl, G. Pretzler, A. Schiavi, G. Schurtz, T. Toncian, P. A. Wilson, and O. Willi. *Proton probing measurement of electric and magnetic fields generated by ns and ps laser-matter interactions.* Laser and Particle Beams, 26(2):241–248, 2008.

[10] O. Willi, T. Toncian, M. Borghesi, J. Fuchs, E. D'Humieres, P. Antici, P. Audebert, E. Brambrink, C. Cecchetti, A. Pipahl, and L. Romagnani. *Laser triggered micro-lens for focusing and energy selection of MeV protons.* Laser and Particle Beams, 25(1):71–77, 2007.

[11] S. Kar, H. Ahmed, R. Prasad, M. Cerchez, S. Brauckmann, B. Aurand, G. Cantono, P. Hadjisolomou, C. L. S. Lewis, A. Macchi, G. Nersisyan, A. P. L. Robinson, A. M. Schroer, M. Swantusch, M. Zepf, O. Willi, and M. Borghesi. *Guided post-acceleration of laser-driven ions by a miniature modular structure.* Nature Communications, 7, 2016.

[12] J. Faure, C. Rechatin, A. Norlin, A. Lifschitz, Y. Glinec, and V. Malka. *Controlled injection and acceleration of electrons in plasma wakefields by colliding laser pulses.* Nature, 444(7120):737–739, 2006.

[13] G. Sarri, D. J. Corvan, W. Schumaker, J. M. Cole, A. Di Piazza, H. Ahmed, C. Harvey, C. H. Keitel, K. Krushelnick, S. P. D. Mangles, Z. Najmudin,

D. Symes, A. G. R. Thomas, M. Yeung, Z. Zhao, and M. Zepf. *Ultrahigh Brilliance Multi-MeV gamma-Ray Beams from Nonlinear Relativistic Thomson Scattering*. Physical Review Letters, 113(22), 2014.

[14] P. Emma, R. Akre, J. Arthur, R. Bionta, C. Bostedt, J. Bozek, A. Brachmann, P. Bucksbaum, R. Coffee, F. J. Decker, Y. Ding, D. Dowell, S. Edstrom, A. Fisher, J. Frisch, S. Gilevich, J. Hastings, G. Hays, P. Hering, Z. Huang, R. Iverson, H. Loos, M. Messerschmidt, A. Miahnahri, S. Moeller, H. D. Nuhn, G. Pile, D. Ratner, J. Rzepiela, D. Schultz, T. Smith, P. Stefan, H. Tompkins, J. Turner, J. Welch, W. White, J. Wu, G. Yocky, and J. Galayda. *First lasing and operation of an angstrom-wavelength free-electron laser*. Nature Photonics, 4(9):641–647, 2010.

[15] S. Brauckmann. *Diagnosis of thin foils irradiated by ultra high intensity laser pulses*. Master Thesis, Heinrich Heine Universität Düsseldorf, 2013.

[16] M. Kosel. *Computational Calculation of Spectral Filtering for a Thomson-Scattering Source*. Bachelor Thesis, Heinrich Heine Universität Düsseldorf, 2015.

[17] E. Aktan. *Laser plasma interactions using ultra-thin foils*. Master Thesis, Heinrich Heine Universität Düsseldorf, 2016.

[18] P. Gibbon. *Short pulse laser interactions with matter*. Imperial College Press, London, 2005.

[19] K. Burnett, V. C. Reed, and P. L. Knight. *Atoms in ultra-intense laser fields*. Journal of Physics B-Atomic Molecular and Optical Physics, 26(4):561–598, 1993.

[20] M. Protopapas, C. H. Keitel, and P. L. Knight. *Atomic physics with super-high intensity lasers*. Reports on Progress in Physics, 60(4):389, 1997.

[21] W.L. Kruer. *The Physics of Laser Plasma Interactions*. Westview Press, Oxford, 2003.

[22] T. Tajima and J. M. Dawson. *Laser Electron-Accelerator*. Physical Review Letters, 43(4):267–270, 1979.

[23] E. Esarey, C. B. Schroeder, and W. P. Leemans. *Physics of laser-driven plasma-based electron accelerators.* Reviews of Modern Physics, 81(3):1229–1285, 2009.

[24] A. Pukhov and J. Meyer-ter Vehn. *Laser wake field acceleration: the highly non-linear broken-wave regime.* Applied Physics B-Lasers and Optics, 74(4-5):355–361, 2002.

[25] J. R. Davies. *Laser absorption by overdense plasmas in the relativistic regime.* Plasma Physics and Controlled Fusion, 51(1), 2009.

[26] Y. Ping, R. Shepherd, B. F. Lasinski, M. Tabak, H. Chen, H. K. Chung, K. B. Fournier, S. B. Hansen, A. Kemp, D. A. Liedahl, K. Widmann, S. C. Wilks, W. Rozmus, and M. Sherlock. *Absorption of short laser pulses on solid targets in the ultrarelativistic regime.* Physical Review Letters, 100(8), 2008.

[27] S. C. Wilks, W. L. Kruer, M. Tabak, and A. B. Langdon. *Absorption of ultra-intense laser-pulses.* Physical Review Letters, 69(9):1383–1386, 1992.

[28] Y. W. Tian, W. Yu, P. X. Lu, H. Xu, V. Senecha, A. L. Lei, B. F. Shen, and X. Wang. *Generation of periodic ultrashort electron bunches and strongly asymmetric ion Coulomb explosion in nanometer foils interacting with ultra-intense laser pulse.* Physics of Plasmas, 15(5), 2008.

[29] S. D. Baton, J. J. Santos, F. Amiranoff, H. Popescu, L. Gremillet, M. Koenig, E. Martinolli, O. Guilbaud, C. Rousseaux, M. R. Le Gloahec, T. Hall, D. Batani, E. Perelli, F. Scianitti, and T. E. Cowan. *Evidence of ultrashort electron bunches in laser-plasma interactions at relativistic intensities.* Physical Review Letters, 91(10), 2003.

[30] V. V. Kulagin, V. A. Cherepenin, M. S. Hur, and H. Suk. *Theoretical investigation of controlled generation of a dense attosecond relativistic electron bunch from the interaction of an ultrashort laser pulse with a nanofilm.* Physical Review Letters, 99(12), 2007.

[31] A. Rousse, C. Rischel, and J. C. Gauthier. *Colloquium: Femtosecond x-ray crystallography.* Reviews of Modern Physics, 73(1):17–31, 2001.

[32] D. Salzmann. *Atomic Physics in Hot Plasmas*. Oxford University Press, New York, 1998.

[33] National Institute of Standards and Technology (NIST). *http*: *//nlte.nist.gov/FLY/*. 2017.

[34] J.D. Jackson. *Classical Electrodynamics*. Wiley, New York, 3rd edition, 1998.

[35] S. Y. Chen, A. Maksimchuk, and D. Umstadter. *Experimental observation of relativistic nonlinear Thomson scattering*. Nature, 396(6712):653–655, 1998.

[36] D. Kiefer, M. Yeung, T. Dzelzainis, P. S. Foster, S. G. Rykovanov, C. L. S. Lewis, R. S. Marjoribanks, H. Ruhl, D. Habs, J. Schreiber, M. Zepf, and B. Dromey. *Relativistic electron mirrors from nanoscale foils for coherent frequency upshift to the extreme ultraviolet*. Nature Communications, 4, 2013.

[37] K. T. Phuoc, S. Corde, C. Thaury, V. Malka, A. Tafzi, J. P. Goddet, R. C. Shah, S. Sebban, and A. Rousse. *All-optical Compton gamma-ray source*. Nature Photonics, 6(5):308–311, 2012.

[38] A. Einstein. *Zur Elektrodynamik bewegter Körper*. Annalen der Physik, 14(S1):194–224, 1905.

[39] S. V. Bulanov, T. Z. Esirkepov, M. Kando, and J. Koga. *Relativistic mirrors in laser plasmas (analytical methods)*. Plasma Sources Science and Technology, 25(5), 2016.

[40] E. Esarey, S. K. Ride, and P. Sprangle. *Nonlinear Thomson scattering of intense laser-pulses from beams and plasmas*. Physical Review E, 48(4):3003–3021, 1993.

[41] S. K. Ride, E. Esarey, and M. Baine. *Thomson scattering of intense lasers from electron-beams at arbitrary interaction angles*. Physical Review E, 52(5):5425–5442, 1995.

[42] D. Strickland and G. Mourou. *Compression of amplified chirped optical pulses*. Optics communications, 56(3):219–221, 1985.

[43] A. Jullien, O. Albert, F. Burgy, G. Hamoniaux, J. P. Rousseau, J. P. Chambaret, F. Augé-Rochereau, G. Chériaux, J. Etchepare, N. Minkovski, and S. M. Saltiel.

10^{10} *temporal contrast for femtosecond ultraintense lasers by cross-polarized wave generation.* Optics Letters, 30(8):920–922, 2005.

[44] M. Kaluza, J. Schreiber, M. I. K. Santala, G. D. Tsakiris, K. Eidmann, J. Meyer-ter Vehn, and K. J. Witte. *Influence of the laser prepulse on proton acceleration in thin-foil experiments.* Physical Review Letters, 93(4), 2004.

[45] S. P. D. Mangles, A. G. R. Thomas, M. C. Kaluza, O. Lundh, F. Lindau, A. Persson, Z. Najmudin, C. G. Wahlstrom, C. D. Murphy, C. Kamperidis, K. L. Lancaster, E. Divall, and K. Krushelnick. *Effect of laser contrast ratio on electron beam stability in laser wakefield acceleration experiments.* Plasma Physics and Controlled Fusion, 48(12B):B83–B90, 2006.

[46] I.H. Hutchinson. *Principles of Plasma Diagnostics, second edition.* Cambridge University Press, Cambridge, 2001.

[47] S. S. Harilal and M. S. Tillack. *Laser plasma density measurements using interferometry.* Fusion Division Center Energy Research, UCSD-ENG-114, 2004.

[48] V. Malka, C. Coulaud, J. P. Geindre, V. Lopez, Z. Najmudin, D. Neely, and F. Amiranoff. *Characterization of neutral density profile in a wide range of pressure of cylindrical pulsed gas jets.* Review of Scientific Instruments, 71(6):2329–2333, 2000.

[49] E.W. Schpolski. *Atomphysik 1.* Deutscher Verlag der Wissenschaften, Berlin, 1967.

[50] A. Buck, K. Zeil, A. Popp, K. Schmid, A. Jochmann, S. D. Kraft, B. Hidding, T. Kudyakov, C. M. S. Sears, L. Veisz, S. Karsch, J. Pawelke, R. Sauerbrey, T. Cowan, F. Krausz, and U. Schramm. *Absolute charge calibration of scintillating screens for relativistic electron detection.* Review of Scientific Instruments, 81(3), 2010.

[51] Image Plate. *http: //www.sb.fsu.edu/~ xray/Manuals/ip.pdf.* 2017.

[52] H. Chen, N. L. Back, T. Bartal, F. N. Beg, D. C. Eder, A. J. Link, A. G. MacPhee, Y. Ping, P. M. Song, A. Throop, and L. Van Woerkom. *Absolute*

calibration of image plates for electrons at energy between 100 keV and 4 MeV. Review of Scientific Instruments, 79(3), 2008.

[53] B. Hidding, G. Pretzler, M. Clever, F. Brandl, F. Zamponi, A. Lubcke, T. Kampfer, I. Uschmann, E. Forster, U. Schramm, R. Sauerbrey, E. Kroupp, L. Veisz, K. Schmid, S. Benavides, and S. Karsch. *Novel method for characterizing relativistic electron beams in a harsh laser-plasma environment.* Review of Scientific Instruments, 78(8), 2007.

[54] X. Xhu. *Electron Acceleration in Ultraintense Laser Pulse Interaction with Solid Targets.* Ph.D. Dissertation, Heinrich-Heine-Universität Düsseldorf, 2017.

[55] K. A. Tanaka, T. Yabuuchi, T. Sato, R. Kodama, Y. Kitagawa, T. Takahashi, T. Ikeda, Y. Honda, and S. Okuda. *Calibration of imaging plate for high energy electron spectrometer.* Review of Scientific Instruments, 76(1), 2005.

[56] National Institute of Standards and Technology (NIST). *http*: *//physics.nist.gov/PhysRefData/Xcom/html/xcom*1*.html.* 2017.

[57] Transmission grating efficie ncy curve. *http*: *//henke.lbl.gov/optical_constants/tgrat*2*.html.* 2017.

[58] S. Ter-Avetisyan, B. Ramakrishna, D. Doria, G. Sarri, M. Zepf, M. Borghesi, L. Ehrentraut, H. Stiel, S. Steinke, G. Priebe, M. Schnurer, P. V. Nickles, and W. Sandner. *Complementary ion and extreme ultra-violet spectrometer for laser-plasma diagnosis.* Review of Scientific Instruments, 80(10), 2009.

[59] K. Landecker. *Possibility of frequency multiplication and wave amplification by means of some relativistic effects.* Physical Review, 86(6):852–855, 1952.

[60] R. H. Milburn. *Electron scattering by an intense polarized photon field.* Physical Review Letters, 10(3):75, 1963.

[61] R. W. Schoenlein, W. P. Leemans, A. H. Chin, P. Volfbeyn, T. E. Glover, P. Balling, M. Zolotorev, K. J. Kim, S. Chattopadhyay, and C. V. Shank. *Femtosecond x-ray pulses at 0.4 angstrom generated by 90 degrees Thomson scattering: A tool for probing the structural dynamics of materials.* Science, 274(5285):236–238, 1996.

[62] J. Osterhoff, A. Popp, Z. Major, B. Marx, T. P. Rowlands-Rees, M. Fuchs, M. Geissler, R. Hoerlein, B. Hidding, S. Becker, E. A. Peralta, U. Schramm, F. Gruener, D. Habs, F. Krausz, S. M. Hooker, and S. Karsch. *Generation of stable, low-divergence electron beams by laser-wakefield acceleration in a steady-state-flow gas cell.* Physical Review Letters, 101(8), 2008.

[63] S. Semushin and V. Malka. *High density gas jet nozzle design for laser target production.* Review of Scientific Instruments, 72(7):2961–2965, 2001.

[64] A. Maksimchuk, S. Reed, S. S. Bulanov, V. Chvykov, G. Kalintchenko, T. Matsuoka, C. McGuffey, G. Mourou, N. Naumova, J. Nees, P. Rousseau, V. Yanovsky, K. Krushelnick, N. H. Matlis, S. Kalmykov, G. Shvets, M. C. Downer, C. R. Vane, J. R. Beene, D. Stracener, and D. R. Schultz. *Studies of laser wakefield structures and electron acceleration in underdense plasmas.* Physics of Plasmas, 15(5), 2008.

[65] C. Peth. *Personal Communication.* Heinrich Heine Universität Düsseldorf, 2017.

[66] H. E. Tsai, X. M. Wang, J. M. Shaw, Z. Y. Li, A. V. Arefiev, X. Zhang, R. Zgadzaj, W. Henderson, V. Khudik, G. Shvets, and M. C. Downer. *Compact tunable Compton x-ray source from laser-plasma accelerator and plasma mirror.* Physics of Plasmas, 22(2), 2015.

[67] B. Qiao, M. Zepf, M. Borghesi, B. Dromey, and M. Geissler. *Coherent x-ray production via pulse reflection from laser-driven dense electron sheets.* New Journal of Physics, 11, 2009.

[68] A. Macchi, S. Veghini, T. V. Liseykina, and F. Pegoraro. *Radiation pressure acceleration of ultrathin foils.* New Journal of Physics, 12, 2010.

[69] J. Robertson. *Diamond-like amorphous carbon.* Materials Science and Engineering R-Reports, 37(4-6):129–281, 2002.

[70] B. Aurand, B. Elkin, L. O. Heim, B. Lommel, B. Kindler, M. Tomut, C. Rodel, S. Kuschel, O. Jackel, and T. Kuehl. *Ultra-thin polymer foils for laser-ion acceleration.* Journal of Radioanalytical and Nuclear Chemistry, 299(2):965–968, 2014.

[71] S. Steinke, A. Henig, M. Schnurer, T. Sokollik, P. V. Nickles, D. Jung, D. Kiefer, R. Horlein, J. Schreiber, T. Tajima, X. Q. Yan, M. Hegelich, J. Meyer-Ter-Vehn, W. Sandner, and D. Habs. *Efficient ion acceleration by collective laser-driven electron dynamics with ultra-thin foil targets.* Laser and Particle Beams, 28(1):215–221, 2010.

[72] A. J. Mackinnon, Y. Sentoku, P. K. Patel, D. W. Price, S. Hatchett, M. H. Key, C. Andersen, R. Snavely, and R. R. Freeman. *Enhancement of proton acceleration by hot-electron recirculation in thin foils irradiated by ultraintense laser pulses.* Physical Review Letters, 88(21), 2002.

[73] K. Khrennikov, J. Wenz, A. Buck, J. Xu, M. Heigoldt, L. Veisz, and S. Karsch. *Tunable All-Optical Quasimonochromatic Thomson X-Ray Source in the Nonlinear Regime.* Physical Review Letters, 114(19), 2015.

[74] A. Buck, J. Wenz, J. Xu, K. Khrennikov, K. Schmid, M. Heigoldt, J. M. Mikhailova, M. Geissler, B. Shen, F. Krausz, S. Karsch, and L. Veisz. *Shock-Front Injector for High-Quality Laser-Plasma Acceleration.* Physical Review Letters, 110(18), 2013.

[75] A. Paz, S. Kuschel, C. Rodel, M. Schnell, O. Jackel, M. C. Kaluza, and G. G. Paulus. *Thomson backscattering from laser-generated, relativistically moving high-density electron layers.* New Journal of Physics, 14, 2012.

[76] M. F. Gu, P. Beiersdorfer, G. V. Brown, A. Graf, R. L. Kelley, C. A. Kilbourne, F. S. Porter, and S. M. Kahn. *Laboratory measurements of the dielectronic recombination satellite transitions of He-like Fe XXV and H-like Fe XXVI.* Canadian Journal of Physics, 90(4):351–357, 2012.

[77] M. Nantel, G. Ma, S. Gu, C. Y. Cote, J. Itatani, and D. Umstadter. *Pressure ionization and line merging in strongly coupled plasmas produced by 100-fs laser pulses.* Physical Review Letters, 80(20):4442–4445, 1998.

[78] A. Maksimchuk, M. Nantel, G. Ma, S. Gu, C. Y. Cote, D. Umstadter, S. A. Pikuz, I. Y. Skobelev, and A. Y. Faenov. *X-ray radiation from matter in extreme conditions.* Journal of Quantitative Spectroscopy and Radiative Transfer, 65(1-3):367–385, 2000.

[79] J. Osterholz, F. Brandl, M. Cerchez, T. Fischer, D. Hemmers, B. Hidding, A. Pipahl, G. Pretzler, S. J. Rose, and O. Willi. *Extreme ultraviolet emission from dense plasmas generated with sub-10-fs laser pulses.* Physics of Plasmas, 15(10), 2008.

[80] K. Eidmann, J. Meyer-ter Vehn, T. Schlegel, and S. Huller. *Hydrodynamic simulation of subpicosecond laser interaction with solid-density matter.* Physical Review E, 62(1):1202–1214, 2000.

[81] E. Lefebvre and G. Bonnaud. *Nonlinear electron heating in ultrahigh-intensity-laser-plasma interaction.* Physical Review E, 55(1):1011–1014, 1997.

[82] H. B. Cai, W. Yu, S. P. Zhu, and C. Y. Zheng. *Short-pulse laser absorption via J x B heating in ultrahigh intensity laser plasma interaction.* Physics of Plasmas, 13(11), 2006.

[83] D. Bauer, P. Mulser, and W. H. Steeb. *Relativistic ponderomotive force, uphill acceleration, and transition to chaos.* Physical Review Letters, 75(25):4622–4625, 1995.

[84] R. W. Lee. *The How To For FLY.* Manual for the code FLY and FLYCHK, 1995.

[85] K. Eidmann, A. Saemann, U. Andiel, I. E. Golovkin, R. C. Mancini, E. Andersson, and E. Forster. *Generation of hot plasma at solid density by high-contrast ultra-short laser pulses.* Journal of Quantitative Spectroscopy and Radiative Transfer, 65(1-3):173–184, 2000.

[86] S. Bastiani, A. Rousse, J. P. Geindre, P. Audebert, C. Quoix, G. Hamoniaux, A. Antonetti, and J. C. Gauthier. *Experimental study of the interaction of subpicosecond laser pulses with solid targets of varying initial scale lengths.* Physical Review E, 56(6):7179–7185, 1997.

[87] P. Audebert, V. Nagels, J. P. Geindre, F. Dorchies, O. Peyrusse, S. Gary, F. Girard, R. Shepherd, J. C. Gauthier, and C. Chenais-Popovics. *X-ray spectroscopy of a thin foil plasma produced by a short-pulse high-intensity laser.* Journal of Quantitative Spectroscopy and Radiative Transfer, 81(1-4):19–30, 2003.

[88] J. Limpouch, J. Psikal, A. A. Andreev, K. Y. Platonov, and S. Kawata. *Enhanced laser ion acceleration from mass-limited targets.* Laser and Particle Beams, 26(2):225–234, 2008.

[89] T. Kluge, W. Enghardt, S. D. Kraft, U. Schramm, K. Zeil, T. E. Cowan, and M. Bussmann. *Enhanced laser ion acceleration from mass-limited foils.* Physics of Plasmas, 17(12), 2010.

[90] Z. Jiang, J. C. Kieffer, J. P. Matte, M. Chaker, O. Peyrusse, D. Gilles, G. Korn, A. Maksimchuk, S. Coe, and G. Mourou. *X-ray spectroscopy of hot solid density plasmas produced by subpicosecond high-contrast laser-pulses at* 10^{18}-10^{19} W/cm^2. Physics of Plasmas, 2(5):1702–1711, 1995.

[91] J. Osterholz, F. Brandl, T. Fischer, D. Hemmers, M. Cerchez, G. Pretzler, O. Willi, and S. J. Rose. *Production of dense plasmas with sub-10-fs laser pulses.* Physical Review Letters, 96(8), 2006.

[92] M. Cirisan, M. Cvejic, M. R. Gavrilovic, S. Jovicevic, N. Konjevic, and J. Hermann. *Stark broadening measurement of Al II lines in a laser-induced plasma.* Journal of Quantitative Spectroscopy and Radiative Transfer, 133:652–662, 2014.

[93] C. Aragon, J. A. Aguilera, and J. Manrique. *Measurement of Stark broadening parameters of Fe II and Ni II spectral lines by laser induced breakdown spectroscopy using fused glass samples.* Journal of Quantitative Spectroscopy and Radiative Transfer, 134:39–45, 2014.

[94] C. Biedermann, R. Radtke, and K. B. Fournier. *Spectroscopy of heliumlike argon resonance and satellite lines for plasma temperature diagnostics.* Physical Review E, 66(6), 2002.

[95] P. Audebert, J. P. Geindre, J. C. Gauthier, and C. Popovics. *High-resolution K-shell dielectronic satellite lines from laser-irradiated spot targets at* 1.06*,* 0.53*, and* 0.27 μm *wavelength.* Physical Review A, 30(2):768–772, 1984.

Publications

- D.P. Higginson, L. Vassura, M.M. Gugiu, P. Antici, M. Borghesi, S. Brauckmann, C. Diouf, A. Green, L. Palumbo, H. Petrascu, S. Sofia, M. Stardubtsev, O. Willi, S. Kar, F. Negoita, J. Fuchs. *Temporal Narrowing of Neutrons Produced by High-Intensity Short-Pulse Lasers.* Physical Review Letters, **115(5)**, 2015

- S. Kar, H. Ahmed, R. Prasad, M. Cerchez, S. Brauckmann, B. Aurand, G. Cantono, P. Hadjisolomou, C.L.S. Lewis, A. Macchi, G. Nersisyan, A.P.L. Robinson, A-M. Schroer, M. Swantusch, M. Zepf, O. Willi, M. Borghesi. *Guided post-acceleration of laser-driven ions by a miniature modular structure.* Nature Communications, **7**, 10792, 2016.

- S. Kar, H. Ahmed, G. Nersisyan, S. Brauckmann, F. Hanton, A-L. Giesecke, K. Naughton, O. Willi, C.L.S. Lewis, M. Borghesi. *Dynamic control of laser driven proton beams by exploiting self-generated, ultrashort electromagnetic pulses.* Physics of Plasmas, **23(5)**, 055711, 2016.

- H. Ahmed, S. Kar, G. Cantono, G. Nersisyan, S. Brauckmann, D. Doria, D. Gwynne, A. Macchi, K. Naughton, O. Willi, C.L.S. Lewis, M. Borghesi. *Investigations of ultrafast charge dynamics in laser-irradiated targets by a self probing technique employing laser driven protons.* Nuclear Instruments and Methods in Physics Research Section A: Accelerators, Spectrometers, Detectors and Associated Equipment, **829**, 172 – 175

Die hier vorgelegte Dissertation habe ich eigenständig und ohne unerlaubte Hilfe angefertigt. Die Dissertation wurde in der vorgelegten oder in ähnlicher Form noch bei keiner anderen Institution eingereicht. Ich habe bisher keine erfolglosen Promotionsversuche unternommen.

Düsseldorf, 06. Dezember 2017 Stephanie Brauckmann